AD-A104 278   ROP INC   WALTHAM MASS   F/G 12/1
MATHEMATICAL AND NUMERICAL ANALYSIS IN SUPPORT OF SCIENTIFIC RE--ETC(U)
JUN 80   C J MCCANN, R M RAO, A MAZZELLA   F19628-76-C-0212
UNCLASSIFIED   AFGL-TR-80-0205   NL

1 OF 2
AD A
104278

RE ①

R+AT
~~Attn: CC/ [illegible]~~
Library Data

AFGL-TR-80-0205

MATHEMATICAL AND NUMERICAL ANALYSIS IN SUPPORT OF SCIENTIFIC RESEARCH

Edited by C. John McCann

RDP, Incorporated
391 Totten Pond Road
Waltham, Massachusetts 02154

FINAL REPORT
17 May 1976 - 31 May 1980

30 June 1980

Approved for public release, distribution unlimited.

AIR FORCE GEOPHYSICS LABORATORY
AIR FORCE SYSTEMS COMMAND
UNITED STATES AIR FORCE
HANSCOM AFB, MASSACHUSETTS 01731

SECURITY CLASSIFICATION OF THIS PAGE *(When Data Entered)*

REPORT DOCUMENTATION PAGE		READ INSTRUCTIONS BEFORE COMPLETING FORM
1. REPORT NUMBER AFGL-TR-80-0205 ✓	2. GOVT ACCESSION NO. AD-A104	3. RECIPIENT'S CATALOG NUMBER 278
4. TITLE *(and Subtitle)* MATHEMATICAL AND NUMERICAL ANALYSIS IN SUPPORT OF SCIENTIFIC RESEARCH		5. TYPE ~~OF REPORT & PERIOD~~ COVERED Final Report 17 May 76 – 31 May 80
		6. PERFORMING ORG. REPORT NUMBER
7. AUTHOR(s) Edited by C. John McCann		8. CONTRACT OR GRANT NUMBER(s) F19628-76-C-0212 ✓
~~9. PERFORMING ORGANIZATION NAME AND ADDRESS~~ RDP, Incorporated 391 Totten Pond Road Waltham, Mass 02154		10. PROGRAM ELEMENT, PROJECT, TASK AREA & WORK UNIT NUMBERS 9993XXXX
11. CONTROLLING OFFICE NAME AND ADDRESS Air Force Geophysics Laboratory Hanscom AFB, Massachusetts 01731 Monitor/Paul Tsipouras/SUWA		12. REPORT DATE 30 June 1980 13. NUMBER OF PAGES 112
14. MONITORING AGENCY NAME & ADDRESS *(if different from Controlling Office)*		15. SECURITY CLASS. *(of this report)* Unclassified 15a. DECLASSIFICATION DOWNGRADING SCHEDULE

16. DISTRIBUTION STATEMENT *(of this Report)*

Approved for public release; distribution unlimited.

17. DISTRIBUTION STATEMENT *(of the abstract entered in Block 20, if different from Report)*

18. SUPPLEMENTARY NOTES

19. KEY WORDS *(Continue on reverse side if necessary and identify by block number)*

Mathematical Analysis, Numerical Analysis, Data Analysis, Scientific Application Programs.

20. ABSTRACT *(Continue on reverse side if necessary and identify by block number)*

This report is presented to give a description of the mathematical and numerical analysis effort in support of the Air Force scientists engaged in basic research in the environmental sciences.

The scope of problems reported both in the particular discipline supported and the type of support is quite broad. Typically, the analysis involved: mathematical modelling, digital filtering, integral evaluations, data fitting, and Fourier analysis.

DD FORM 1 JAN 73 1473 EDITION OF 1 NOV 65 IS OBSOLETE

Unclassified

SECURITY CLASSIFICATION OF THIS PAGE *(When Data Entered)*

Application computer programs were also developed to not only check the analysis but also to produce data required by the scientists.

The duration of support is just as varied and lasted anywhere from a few days to many months. Therefore, some of the problems reported are completely analyzed, while others reached various degrees of evolution toward a final resolution.

LIST OF AUTHORS

C. John McCann
Rahul M. Rao
Andrew Mazzella
Brendan J. Welch
John Palys

The list of authors on page iii are authors of the fifteen articles in this report. The initiators are persons who requested that the work be done per Mr. C. John McCann, RDP Inc.

FOREWORD

This support analysis and scientific programming was performed under contract to the Analysis and Simulation Branch (SUWA) of the Air Force Geophysics Laboratory (AFGL), Hanscom Air Force Base, Massachusetts. Programs described herein and documentation of such can be obtained from the computer library of SUWA.

TABLE OF CONTENTS

SYNCHRONOUS DEMODULATION OF CHOPPER MODULATED RADIANCE SIGNALS

Initiator:	Mr. T. Murdock
Problem No.:	3003
Project No.:	7670

This problem entailed the development of a sequence of programs to process telemetered radiance signals. The main processing was performed in a program called IRDSP. The following contains a description of the processing algorithms developed by RDP for this task.

Program IRDSP (Infra-Red-Data Signal Processing) was written to demodulate the chopper-modulated radiance signals contained in the telemetered data received from the IRBS or ZIP flights. The multi-tape telemetry data base is processed by IRDSP *one tape at a time*. The output of the program consists of plots and printed tables of the radiance estimates and a plot-data file. When the entire input data base has been processed, the plot-data files are sorted by key and a plot-data base is created. Using this, flight-plots of the radiance signals are produced using a separate program. The flight plots can be over the entire flight time, or over a time interval falling on two input tapes.

In this write-up the description of program IRDSP is presented in four sections:

1. The Signal Demodulation task.
2. Input Data Base.
3. Processing Methodology and Program Flow Chart.
4. Demodulation Algorithm.

1. The Signal Demodulation Task

The high speed data link in both the IRBS and ZIP instrumentation transmit the radiance measurements made by the multi-sensor Infra-Red (IR) detectors in a chopper modulated form. 27 of the 38 channels in IRBS and 32 of the 44 channels in ZIP are chopper-modulated outputs of Infra Red (IR) detectors. Each is sensitive to a unique range of wavelengths. RDP's task is to demodulate the radiance message in each channel and deliver plots of time versus radiance tables to the client.

A typical chopper-modulated radiance waveform in the input data base has the form as shown in Figure 1. The radiance message is embedded in the relatively slowly varying envelope of the chopping waveform.

Over the 20-minute flight time, the detectors are exposed to both calibrated and unknown target sources of radiance. Each channel output will contain the numbered features shown in Figure 1. These are briefly described below.

1. Just prior to take-off the detectors are calibrated by making the hardware execute an auto-calibration (Autocal) sequence in which known levels of black body radiation are shone on the detectors.
2. Approximately 60 seconds after take-off, the autocal sequence is repeated for an inflight calibration.
3. After 100 seconds into the flight, the detectors scan the earth limb in 1/2° increments. This data is taken for the next 200 secs.
4. During the remainder of the flight, the detectors measure Zodiacal light.

To design a suitable demodulation algorithm, we must have an adequate mathematical representation of the received chopped waveforms.

The chopping of the radiance message is done by mechanically opening and closing the detector aperture in step with a high-Q tuning fork of frequency f_c Hz.

The chopping waveform is not rectangular. Nevertheless it is periodic and can be represented by a Fourier series as:

$$\varphi(t) = \sum_{n=-\infty}^{\infty} a_n \cdot e^{jnw_c t} \quad . \qquad (1)$$

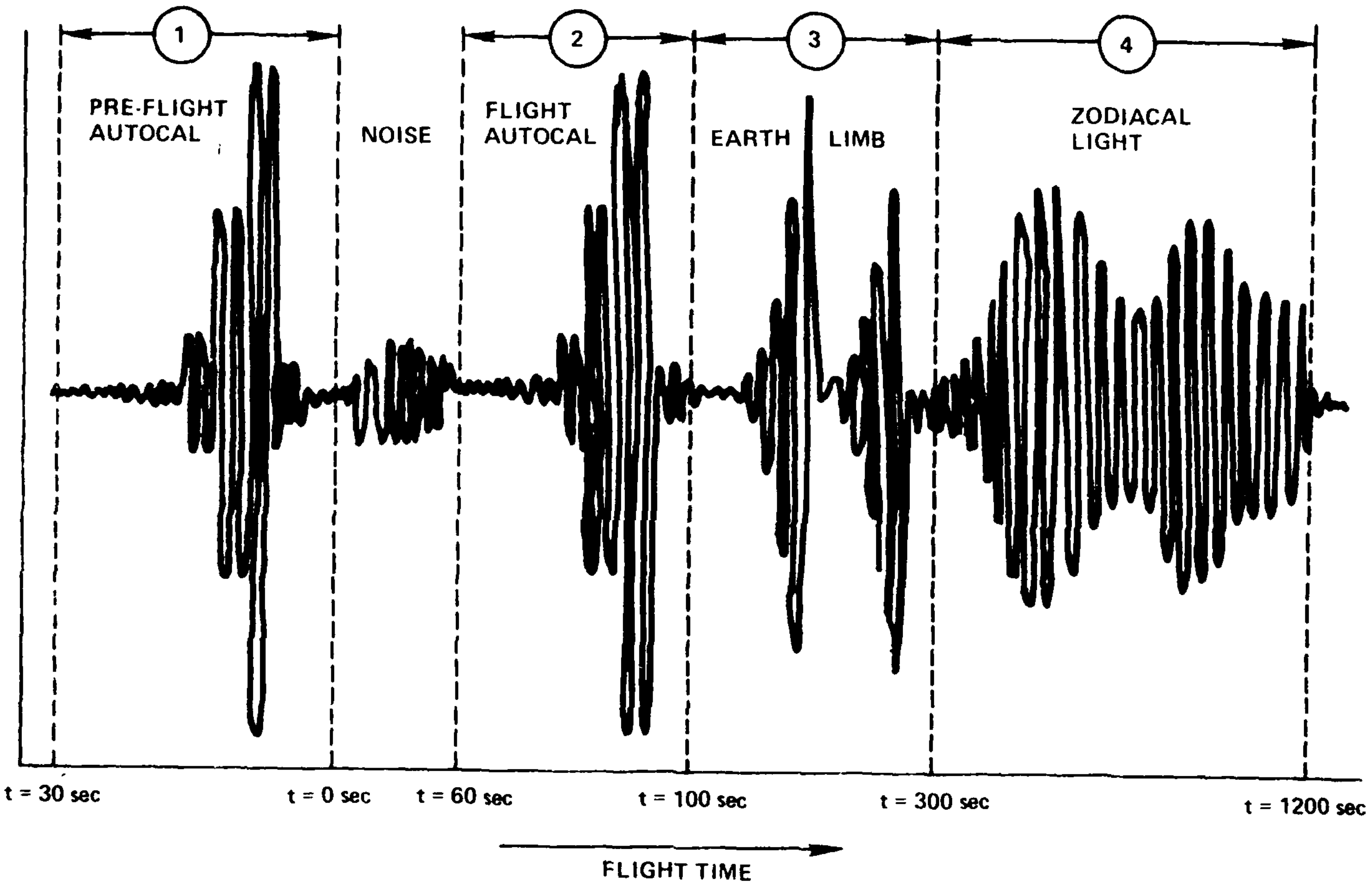

Fig. 1 Features in a typical IRBS or ZIP chopper modulated radiance signal.

Its Fourier Transform is a train of impulses,

$$\Phi(w) = 2\pi \sum_{n=-\infty}^{\infty} a_n \cdot \delta(w - nw_c) \quad . \tag{2}$$

When the radiance message, r(t) is chopped by $\varphi(t)$, the convolution theorem states that $r(t) \cdot \varphi(t)$ has the spectrum

$$F(r(t) \cdot \varphi(t)) = \frac{1}{2\pi} R(w) * \Phi(w)$$

(where F( ) is the Fourier Transform operator and * is the convolution operator)

$$= R(w) * \sum^{\infty} a_n \, \delta(w - nw_c)$$

$$= \sum_{n=-\infty}^{\infty} a_n \cdot R(w - nw_c) \quad , \tag{3}$$

i.e., the chopped message spectrum is the weighted sum of the translates of the message spectrum, each translate being located at a chopper harmonic.

Before sampling and PCM encoding, however, the message spectrum at D.C. is removed by a band-pass filter which also acts as a de-aliasing filter. Now, if the message spectrum R(w) has a bandwidth $B \ll w_c$, then,

$$s(t) = r(t) \cdot \varphi(t) \Big|_{\text{Band Pass Filtered}} \tag{4}$$

has the approximate spectra

$$S(w) = \sum_{n=-\infty}^{\infty} a_n \cdot G_n \cdot R(w - nw_c) \quad , \tag{5}$$

where G_n are the values of the filter's frequency response at the n^{th} harmonic location and is assumed to be constant in a local neighborhood, $nf_c \pm B$ Hz.

Letting $A_n = a_n \cdot G_n$, the received chopped radiance signals then have spectra of the torm,

$$S(w) = \sum_{n=-\infty}^{\infty} A_n \cdot R(w - nw_c) \quad . \tag{6}$$

Note that $A_n = 0$ for $n=0$ and $n > f_s/2f_c$ due to the band-pass filter.

The signal processing task is to reconstruct the radiance message r(t) from a noisy observation of s(t). In practice, this can be done only to within a scale factor since the Fourier coefficients, a_n, of the chopping waveform as manifested in s(t) are not known. The proper scale factor is then determined from the autocalibration level outputs.

2. Input Data Base

The ZIP and IRBS data bases have different amounts and types of data, but as far as radiance data demodulation is concerned, both data bases have the same structure and are thus processed in the same manner. The IRBS rocket is expected to transmit information for about 20 minutes. The onboard electronic hardware samples 38 desired output quantities, quantizes each sample to 14 bits, multiplexes and block-encodes the binary data to facilitate receiver synchronization and transmits the output bit stream at 300 kilo-bits per sec (kbps) as a PCM Biphase (L) signal. At the receiver, the received bit sequence is recorded on an analog tape. In the ZIP design 44 output quantities are sampled, multiplexed, and telemetered at 616 kbps. In either case, the analog data tape is, however, not directly accessible by a computer. In fact, to make the data compatible with program IRDSP several steps are involved. These steps are block diagrammed in Figure 2.

A brief description of the steps in Figure 2 is as follows:

1. The analog tape is decoded in pieces on to "n" digital tapes by the Honeywell 316 FM decoder. Each tape (designated I.1-I.n) can contain approximately 3 minutes of IRBS data or about 90 secs of ZIP data.
2. Duplication on to work tapes. The tapes in Step 1, i.e., I.1-I.n are simply duplicated on to work tapes, II.1-II.n. All further steps are

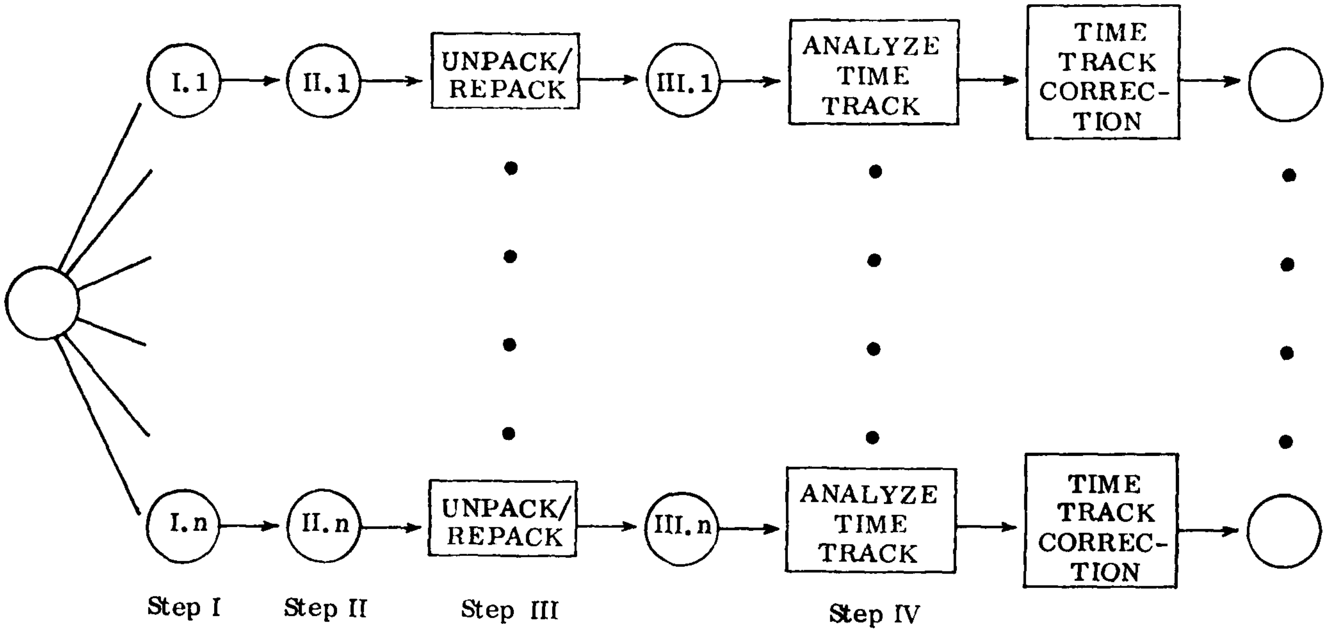

Figure 2. Steps in the Decoding and Restructuring of the IRBS/ZIP Analog Data Tape.

performed on these work tapes. The reason is that in case of loss of information in any tape, recovery via duplication in Step 2 has much faster turnaround time than recovery via decoding in Step 1.

3. Unpacking/Repacking. The data in tapes II.1-II.n (the outputs from Step 2) exists in blocks of packed bits. A modified version of HON316 is used to unpack and repack specific bits into integer values. These numbers are, in fact, the output of the A/D converter in the rocket hardware which originally sampled the data channels. HON316 then writes these integer sample values in blocks to the output tape.

   Each output tape (III.1-III.n) contains one file comprised of binary records of the form shown in Figure 3.

t_1	t_2		t_{13}: IRBS t_{11}: ZIP
$d_1(t_1)$			
⋮		⋮	
$d_{38}(t_1)$: IRBS $d_{44}(t_1)$: ZIP			$d_{38}(t_{13})$: IRBS $d_{44}(t_{11})$: ZIP

Figure 3. Structure of a Record in the Input Tapes for Program IRDSP.

Each record contains the two-integer dimensions of a data array followed by the array itself. Array dimensions are 38 x 13 for IRBS and 44 x 11 for ZIP. The first location of each column contains sampling time values and the remaining locations contain channel outputs at this time instant.

In the ideal situation of no time errors (row #1 of each record), the tapes III.1-III.n are compatible with program IRDSP. Practically, however, errors are invariably present and the following step deals with this problem.

4. Identification and classification of time errors. Program ANALYZE is used to read the tapes III.1-III.n (one tape per run) and scan through the first row of each record identifying and classifying time-data errors. It also produces a plot of time versus sample index in which errors can be visually observed.

Each run's printout is next inspected and a judgment is made on whether the corresponding tape is acceptable. Tapes that are deemed unacceptable are returned to be re-digitized.

The above four-step procedure for preparing the raw, rocket data for analysis by program IRDSP, appears deceptively straight forward. In fact, it is a time-consuming process due to the turnaround requirements for tape-jobs on the AFGL computer system. Experience with the test data tape has shown that 4-5 weeks are needed to complete Steps 1-4 above, if the data exhibits a large number of time errors. Further, the probability exists that the time errors will lead to misinterpretation of the data.

3. Processing Methodology and Program Flowchart

Earlier, in Section 2, the final structure of the received rocket data was described. The data exists on 9-track tapes. Consider the IRBS data for a moment. Each tape has approximately 3 minutes of data. Since the system sampling rate is 563.91 Hz, one tape contains over 100,000 samples of data for each of the 38 channels. For processing on the AFGL computer which has a 300k word memory, one is forced to process the data in smaller convenient segments. Currently, a segment size of 4000 is being used. This is approximately 7 seconds of data. This segmentation does not, however, interfere with the signal processing. Successive input segments are precisely overlapped to compensate for data loss due to end-effects of the digital filters and consequently the output blocks are contiguously spaced in time. Of course, if a data gap is detected, the segmenting process continues from beyond the gap. The process continues till the data corresponding to the specified time interval has been analysed or until an end-of-file mark has been reached.

The implementation of the above processing methodology is in the form of two routines – FNDBLKS and GETBLK. FNDBLKS is called once before any signal processing begins. It scans through the input data tape and identifies segments to be processed. This identification involves tagging the location in the file of the beginning time and end time for each segment in terms of (1) the record # in the file and (2) the column # within this record.

The second routine, GETBLK, uses the information compiled by FNDBLKS to read a data block from tape, convert the integer A/D output values into voltage values and make the block available to the subroutine ENVELOP for signal processing. After a call in which a new channel is specified, successive calls to GETBLK can be used to sequentially access the data segments for that channel.

Having described how the data is blocked and accessed, the overall flow chart of IRDSP can now be outlined as in Figure 4.

4. The Demodulation Algorithm

The radiance estimation procedure used in program IRDSP is now described. With reference to the flow chart in Figure 4, the following description applies to the processing block, labelled "ENVELOP."

Quite simply, the radiance estimate is the envelope of the complex, narrow-band component of the received data, within the frequency band $f_c \pm B$ Hz. Here, f_c is the chopper frequency and B is the assumed radiance-signal bandwidth. The procedure for obtaining the envelope entails complex demodulation and is block diagrammed in Figure 5 for the ideal noise-free situation.

The rest of the section is devoted to the justification for and the limitations of complex demodulation as a viable procedure for estimating the radiance message from chopper-modulated received data. A noise-free analysis first establishes the validity of the procedure. Next, a suitable noise model is included in the analysis; it is shown that an undesirable aspect of the in-band noise is to non-linearly distort the estimate. This affect will be negligible over most of the rocket data due to a sufficiently high Signal-power to in-band Noise-power Ratio (SNR) and is significant only at very low message levels.

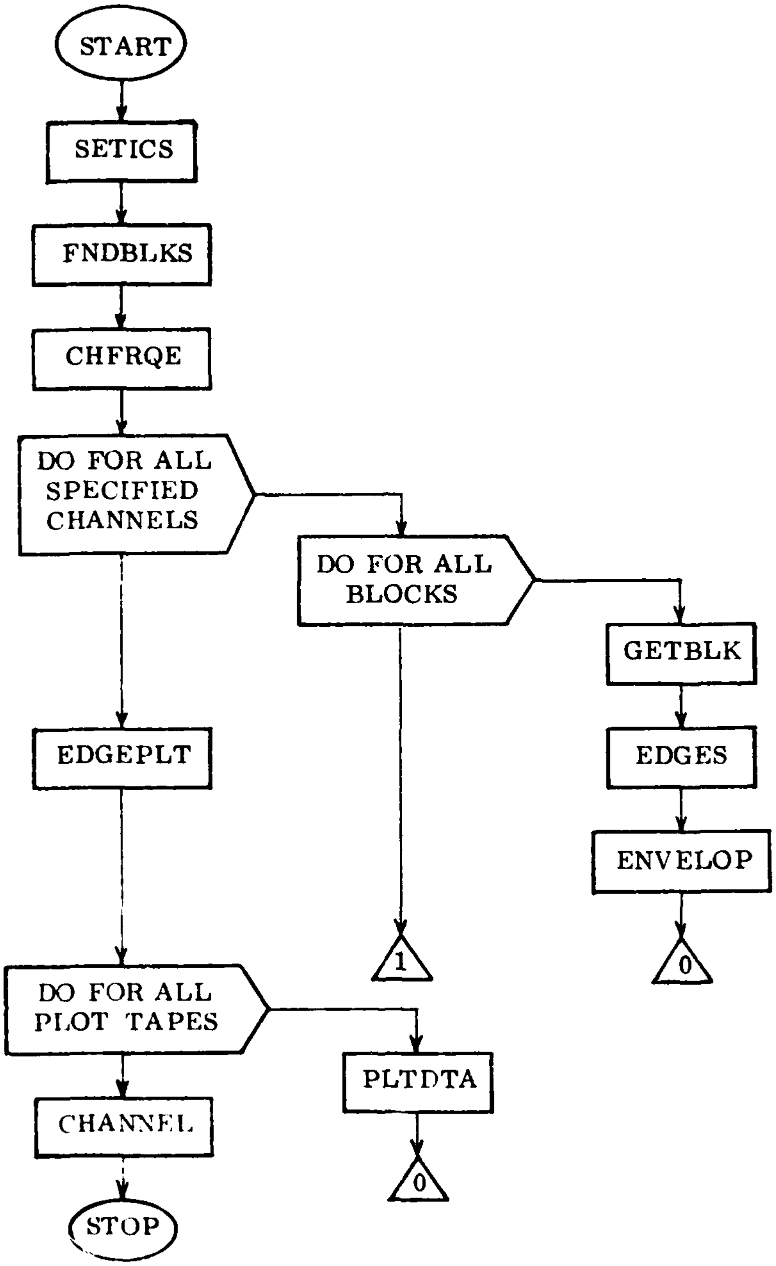

Figure 4. Structured Flowchart of Program IRDSP.

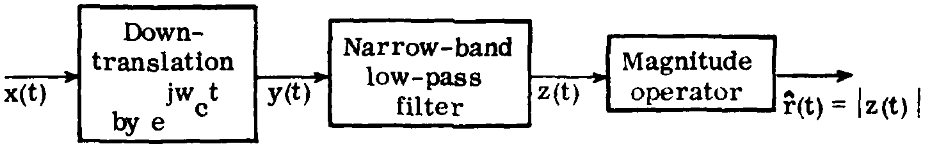

Figure 5. Block Diagram of Complex Demodulation Procedure for Noise-free Signal.

Finally, the specifications of the practical, complex demodulation algorithm are summarized.

Noise-Free Analysis

The chopper-modulated data channels are assumed to have the following form:

$$s(t) = r(t) \cdot \varphi(t) \quad , \tag{7}$$

where r(t) = the radiance measured by the detector – assumed to be low frequency in nature and bandlimited to B Hz

$\varphi(t)$ = the chopping waveform

$$= \sum_n A_n \cdot e^{jnw_c t} \tag{8}$$

$w_c = 2\pi f_c$ = the fundamental radian frequency of the chopper

$\{A_n\}$ are the complex coefficients of the Fourier series.

Let $A_1 = A_{ch} \cdot e^{j\theta_c}$. If the received data x(t) is noise-free,

$$x(t) = s(t) = r(t) \cdot \sum_n A_n e^{jnw_c t} \quad . \tag{9}$$

Then, from Figure 5, the radiance estimate is

$$\hat{r}(t) = |z(t)| = \left| \left\{ x(t) \cdot e^{-jw_c t} \right\} * h(t) \right| \quad . \tag{10}$$

Assuming for the moment that the low-pass filter is ideal and has bandwidth $\beta > B$, the message bandwidth, then one obtains

$$\hat{r}(t) = |A_1 \cdot r(t)| = \left| A_{ch} r(t) \cdot e^{j\theta_c} \right| = A_{ch} r(t) \quad , \qquad (11)$$

i.e., the estimate $\hat{r}(t)$ is a scaled replica of the radiance impinging on the detector. Note in Eq. (11) that the unknown phase of the chopper fundamental is eliminated by the magnitude operator, an advantage that accrues from the use of the complex sinusoid $e^{jw_c t}$ in the frequency down-translation (in contrast to the use of a real sinusoid $\sin w_c t$ or a co-sinusoid $\cos w_c t$).

The Noise Model and Its Effect on the Estimator

The earlier noise-free analysis establishes the viability of complex demodulation as a procedure for recovering a low frequency, bandlimited message from a noise-free chopper modulated version of it. A variety of noise sources, however, contaminate the actual modulated signals. For simplicity these are separated into two parts. One part is the broadband random noise caused by background radiance, the electronics and the telemetry transmission channel. The other, also assumed wideband, is the transient interference caused by cosmic ray showers. The received signal can then be expressed as:

$$x(t) = s(t) + \mu(t) + w(t) \quad , \qquad (12)$$

where $s(t)$ = modulated signal defined in Eq. (7),

$\mu(t)$ = broadband noise representing the sum of background atmospheric radiance, the detector noise and the system noise,

$w(t)$ = cosmic ray interference consisting of randomly occurring spiky transients.

Note that the two contaminants are very different in the time domain but are similar (broadband) in the frequency domain. For this noisy, received signal, the complex demodulation procedure gives

$$\hat{r}(t) = \left| \left\{ x(t) \cdot e^{-jw_c t} \right\} * h(t) \right|$$

$$= \left| A_{ch} \cdot e^{j\theta_c} \cdot r(t) + \mu_{n.b.}(t) + w_{n.b.}(t) \right| , \qquad (13)$$

where an ideal filter has again been assumed and $\mu_{n.b.}(t)$ and $w_{n.b.}(t)$ are complex narrow-band components of $\mu(t)$ and $w(t)$, respectively, defined by the spectra

$$\begin{aligned} U_{n.b.}(f) &= U(f) \qquad \text{for} \quad f_c - \beta \leq f \leq f_c + \beta \\ &= 0 \qquad \text{elsewhere} \end{aligned} \qquad (14)$$

and similarly,

$$\begin{aligned} W_{n.b.}(f) &= W(f) \qquad \text{for} \quad f_c - \beta \leq f \leq f_c + \beta \\ &= 0 \qquad \text{elsewhere} \ . \end{aligned} \qquad (15)$$

Note that both $U_{n.b.}(f)$ and $W_{n.b.}(f)$ are asymmetric spectra since the corresponding time signals $\mu_{n.b}(t)$ and $w_{n.b.}(t)$ are complex.

On comparing Eqs. (11) and (13), we see that when the received data is noisy, the estimate r(t) is not simply a scaled replica of the radiance message, but is corrupted by the in-band noise components. Of course, this in-band noise energy is bound to show up in the output, since spectrally, it is indistinguishable from the message energy. What is undesirable about the form of Eq. (13), however, is that the in-band noise distorts the message in a non-linear way. To see this more clearly we proceed as follows: Let

$$n(t) = \mu_{n.b.}(t) + w_{n.b.}(t) = \nu(t) \cdot e^{j\theta_n(t)} \ . \qquad (16)$$

In Eq. (16) the noise representation is in terms of the slowly varying envelope $\nu(t)$ and phase $\theta_n(t)$ of the narrow-band, untranslated, noise process. Then, Eq. (13) gives

$$\hat{r}(t) = \left| A_{ch} \cdot r(t) \cdot e^{j\theta_c} + n(t) \right|$$

$$= \left| \{A_{ch} r(t) \cos \theta_c + \nu(t) \cos \theta_n(t)\} + j \{A_{ch} r(t) \sin \theta_c + \nu(t) \sin \theta_n(t)\} \right| , \tag{17}$$

which simplifies to

$$\hat{r}(t) = \left[A_{ch}^2 \cdot r^2(t) + \nu^2(t) + 2A_{ch} \cdot r(t) \cdot \nu(t) \cos \{\theta_c - \theta_n(t)\} \right]^{1/2} . \tag{18}$$

Equation (18) gives the radiance estimator when the received data is noisy. By setting $\nu(t) = 0$ in Eq. (18), the noise-free estimate is $\hat{r}(t) = A_{ch} \cdot r(t)$, which is the same as in Eq. (11).

Of practical importance, however, is the condition of relatively low noise, i.e., when

$$SNR = \frac{\text{Power in } r(t)}{\text{Power in } n(t)} \gg 1 . \tag{19}$$

To see the nature of the estimator at high SNR, rewrite Eq. (18) as

$$\hat{r}(t) = A_{ch} r(t) \left[1 + 2 \cdot \frac{\nu(t)}{A_{ch} r(t)} \cos \{\theta_c - \theta_n(t)\} + \frac{\nu^2(t)}{A_{ch}^2 r^2(t)} \right]^{1/2} . \tag{20}$$

The last term in the expression is a random process being a function of the input noise. At time t, for the random variable,

$$x_t = \frac{\nu^2(t)}{A_{ch}^2 r^2(t)} \tag{21}$$

if the condition of (19) is true it follows that

$$\text{Prob}\,(x_t < \delta) \simeq 1 \quad \text{for} \quad 0 < \delta \ll 1 . \tag{22}$$

Hence, neglecting the last term in (20) and retaining the first two terms in the power expansion, (20) gives

$$\hat{r}(t) \simeq A_{ch} r(t) \left[1 + \frac{\nu(t)}{A_{ch} r(t)} \cos \{\theta_c - \theta_n(t)\} \right]$$

$$\simeq A_{ch} r(t) + \nu(t) \cos (\theta_c - \theta_n(t)) \quad . \tag{23}$$

Hence, at high SNR, the estimate $\hat{r}(t)$ contains a scaled replica of the message plus output noise.

The conclusion from the above noise analysis is that the complex-demodulated envelope $\hat{r}(t)$ will satisfactorily recover the radiance message from the IRBS data.

Practical Considerations

In the preceding discussions, an ideal low-pass filter had been assumed to simplify the discussions. A practical algorithm cannot, however, use an ideal filter since its non-casual, infinite impulse response only allows the computation of its output with infinite delay. To make a usable filter, one must, therefore, relax the frequency domain specifications up to the point where the performance is still acceptable. Thus, the discontinuous transition from passband to stopband is modified to provide an intermediate transition band and rather than insisting on infinite stopband suppression one specifies a large but finite attenuation. Of course, the only effect of using such a non-ideal filter is that the higher message-translates in the modulated data and the out-of-band noise will not be entirely eliminated but acceptably attenuated.

Once suitable specifications have been decided the designer must choose between the two generic filter types – Finite Impulse Response (FIR) or Infinite Impulse Response (IIR) – for his needs. The attendant trade-off is that IIR filters can meet magnitude-response specifications with much lower filter order than can FIR filters but they invariably have a non-linear phase response with delay while FIR filters are easily constrained to have linear phase and no delay. In the present application it was decided that waveform symmetry and delay-less processing were uncompromisable requirements. Hence, an FIR linear phase filter is used.

The specifications for the low-pass filter used in Figure 5 are as follows:

1. FIR, linear phase, real coefficients
2. Passband (± .0274 dB) = .45 Hz
3. Transition Band = 6.0 Hz
4. Minimum stopband attenuation = 50 dB.

The filter was designed by the windowing method using a Kaiser I_0 - sinh window. The resulting filter is close to optimal (in the sense that it is "nearly-equiripple"). Its 3 dB bandwidth is 2.82 Hz and filter order is 276.

When this filter is used in the demodulation scheme on actual data, a hitherto unconsidered interaction between the sharp cosmic ray transients and the filter's long processing memory (.49 secs) comes to light. When a sharply spiked cosmic ray "hit" is processed, the output exhibits the familiar and highly undesirable ringing effect. The narrower the spike is, the more this ringing is like the impulse response of the filter. Obviously, the larger the spike, the more pronounced is the ringing. Also, if a succession of hits occurs each within .49 secs of its neighbors, the radiance estimate will be obscured by a long and persistent (and meaningless) ringing. Note that the above implied rate is 2 hits/sec which is considered entirely probable.

Thus, we see that our earlier conclusion, that the radiance estimator of Figure 5 was satisfactory, was rather hasty. The earlier noise analysis was based on steady-state frequency domain characterization of the contaminants, and since both the stationary noise and the cosmic ray hits are broadband phenomena they were lumped together into one noise process in Eqs. (16) and (17). It is clear now that the spikes have to be removed and that this has to be done in the time domain where the two contaminants are differentiable.

The spike detection algorithm has to be some variation of the basic approach of thresholding the difference between the signal and a smooth version of it. To set a threshold, the local signal variance is needed. In the chopped data, direct application of such an algorithm will not work, however, since the variance values will be dominated by the chopper energy and not the spike energy. Thus, the chopper energy must be removed prior to cleaning. In other words, with reference to Figure 5, the cleaning must, therefore, be performed on z(t). By then, of course, the ringing would be present. Several cleaning algorithms were tested by RDP with reasonable success in detecting and removing spikes.

ANALYSIS OF THE DETECTOR SIGNAL PROCESSOR

Initiator: Mr. S. Price
Problem No.: 4060
Project No.: 7670

SUMMARY OF THE PROBLEM AND PRINCIPAL RESULTS

Each element in the Detector Array has an associated Detector Signal Processor circuit which performs a logarithmic compression of the dynamic range of the sensor measurement. Our task is to analyze the circuit and to obtain a closed form expression for the output-to-input transfer characteristic. This characteristic would enable one to "de-log" the channel outputs. Towards this end we have determined:

(i) The "snap-shot" transfer function of the logging circuit as a function of the output level,

(ii) the approximate pass-bandwidth and gain as a function of the output level,

(iii) a closed-form expression for the output-to-input transfer characteristic.

The transfer expression that we have obtained appears to have an adequate functional form. However, when it is written in the peak-to-peak input versus peak-to-peak output form to match the calibration data, it contains a dependence on the actual minimum and maximum output values rather than on just their difference. Because of this a simpler expression was heuristically determined. The parameters in this expression were optimized, via iterative regression, for each detector channel. The converged heuristic transfer expression appears to be quite satisfactory in explaining the calibration data.

PROBLEM DEFINITION

The Detector Signal Processor (DSP) can be represented by the block diagram in Figure 1, as a cascade of four amplifier stages.

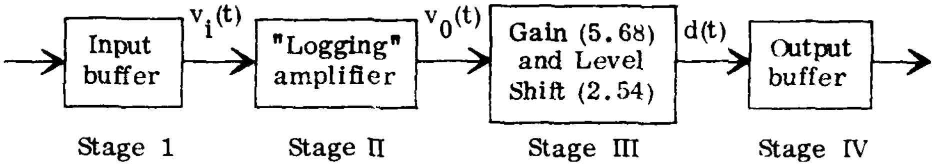

Figure 1. Functional Block Diagram of the Detector Signal Processor.

The end stages are unity gain, input and output buffer stages respectively, and are used for the usual obvious reasons. Stages II, III are the key elements of the signal processor. In Stage II, the buffered sensor output v_i is amplified with a constant gain when $|v_i| <$ 1mv and with a logarithmically decreasing gain, with increasing $|v_i|$, when $|v_i| \gg$ 1mv. The resulting bipolar output v_0 is then amplified with a constant gain of 5.68 by Stage III, and also level shifted by 2.5 volts to produce a unipolar positive output d(t).

Our intent is to obtain an output-to-input transfer expression of the form,

$$v_i = f(d) \quad , \tag{1}$$

since it will enable the "de-logging" of the channel outputs, to yield the original sensor output v_i. For this purpose it is sufficient to focus our attention on Stage II, and seek a transfer expression,

$$v_i = g(v_0) \tag{2}$$

because obtaining (1) from (2) involves only a trivial change of variables defined by

$$d(t) = 5.68v_0(t) + 2.5 \quad . \tag{3}$$

Equations (1) - (3) describe the analysis problem. In the next section we describe the particular analysis methodology that we employ.

ANALYSIS METHODOLOGY

Figure 2 below is the circuit diagram for Stage II.

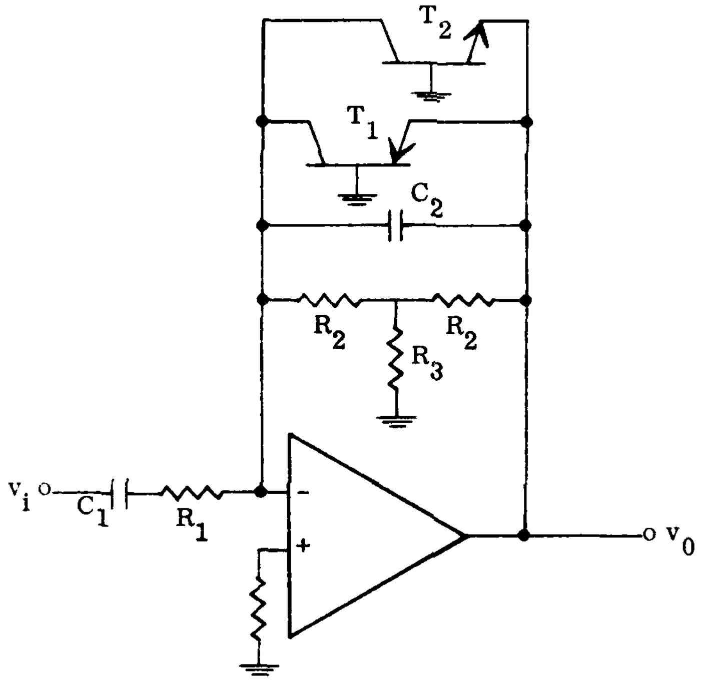

Fig. 2. The Circuit Diagram for the Logging Amplifier

To analyse the circuit of Fig. 2, we initially considered the usual approach of applying Kirchoff's current law (KCL) at the node at the '-ve' input of the operational amplifier. The resulting differential equation is non-linear due to the non-linear feedback from the logging transsistors T_1 and T_2. By linearizing around particular output values, one could possibly obtain a solution. However, at this point we chose to use an alternative approach because we believe it gives better insight into the circuit action. This alternative approach for obtaining a transfer expression is best explained in terms of its three constituent steps. These are:

Step 1: The Equivalent Circuit

Since the logging transistors are acting as variable resistors which change the gain of the stage in a non-linear fashion, the first step is to replace T_1 and T_2 by their incremental resistances $R_{v,pnp}$ and $R_{v,npn}$ which are exponentially decreasing functions of the output voltage.

Step 2: The Family of Frequency Response Functions

Conditioned on a particular value that the output assumes, a linear analysis is performed which yields a "snap-shot" frequency response. Moreover, the set of values that v_0 can assume, defines a family of frequency response curves. The time varying function, $v_0(t)$ can then be viewed as the output of a system whose frequency response is making transitions from one member of this family of responses to another with time.

Step 3: The Approximate Output Voltage Dependent Gain and the Transfer Expression

For input $v_i(t)$ band-limited to be within the minimum bandwidth that the varying system can ever assume, the system transfer function is approximatable by a frequency-independent but output-voltage dependent "gain" ($\triangleq G(v_0)$), i.e.,

$$\frac{v_0(t)}{v_i(t)} = G(v_0) \quad . \tag{4}$$

Hence,

$$v_i = G^{-1}(v_0) \cdot v_0 = g(v_0) \quad .$$

This is the desired output-to-input transfer characteristic, mentioned earlier as Eq. (2).

In the next section, the analysis outlined in Steps 1 - 3 above, shall be carried out.

CIRCUIT ANALYSIS

As outlined in the previous section, the analysis will be performed in three steps, as follows.

Step 1: The Equivalent Circuit

In Appendix A1, the incremental resistance, R_v, of a pnp transistor used in the "transdiode" logging configuration is derived. The result is,

$$R_v(v_E) = R_0 \cdot 10^{-v_E/E_0} , \tag{5}$$

where

$$R_0 = 113.93\ M\Omega \tag{6}$$

$$E_0 = 72.05\ mv\ . \tag{7}$$

We can define the incremental resistances of transistors T_1 and T_2 in Fig. 2 in terms of $R_v(v_E)$ of (5) as,

$$R_{v,pnp}(v_0) = \begin{cases} \infty & \text{for } v_0 \leq 0 \\ R_v(v_0) & \text{for } v_0 > 0 \end{cases} \tag{8}$$

and

$$R_{v,npn}(v_0) = \begin{cases} R_v(|v_0|) & \text{for } v_0 \leq 0 \\ \infty & \text{for } v_0 > 0\ . \end{cases} \tag{9}$$

Formulas (8), (9) reflect the fact that of the two transistors T_1 and T_2, only one is active depending upon the polarity of v_0.

Another simplification of the circuit in Fig. 2 is that the T-network in the feedback path can be replaced by an equivalent resistance,

$$R_T = 2R_2 + \frac{R_2^2}{R_3}\ . \tag{10}$$

For $R_2 = 10\ K\Omega$ and $R_3 = 57.47\Omega$, formula (10) gives,

$$R_T = 1.76\ M\Omega\ . \tag{11}$$

Using Eqs. (8), (9), and (11), the equivalent circuit for Stage II of Fig. 2 is as shown below in Fig. 3.

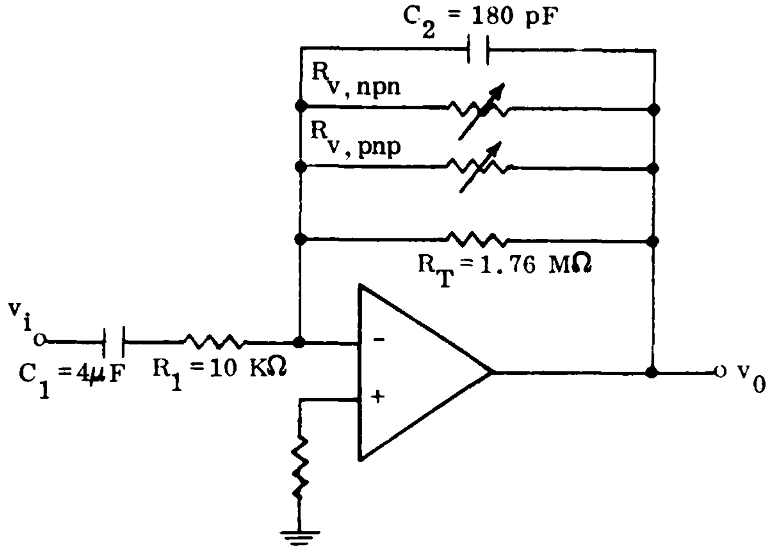

Fig. 3. The Equivalent Circuit for the "logging" Stage of Fig. 2

Step 2: The Family of Frequency Response Functions

The advantage of the equivalent representation in Fig. 3 of the logging circuit is that instead of analysing the non-linear feedback explicitly, we can now perform a linear analysis of the fixed-elements, linear circuit that results for each value that the output assumes. Thus, at $v_0 = g$ volts, a "snap-shot" of the varying frequency response is obtained. Moreover, the set of values that the output can assume defines a family of frequency responses for the circuit. Useful simplifications result from this approach. Let

$$R_b = R_T \| R_{v,pnp} \| R_{v,npn}$$

$$= \text{the equivalent feedback resistance.} \qquad (12)$$

Note: $\|$ is the parallel combination operator. As explained above, at $v_0 = g$ a fixed value, R_b in (12) has a constant value. For the circuit of Fig. 3, we can then define the two impedances,

$$Z_f = \frac{1}{jwC_1} + R_1 \qquad (13)$$

$$Z_b = \left(\frac{1}{jwC_2}\right) \| R_b \tag{14}$$

and the circuit can be redrawn as in Fig. 4. The notion of a "snap-shot" analysis can now be elaborated.

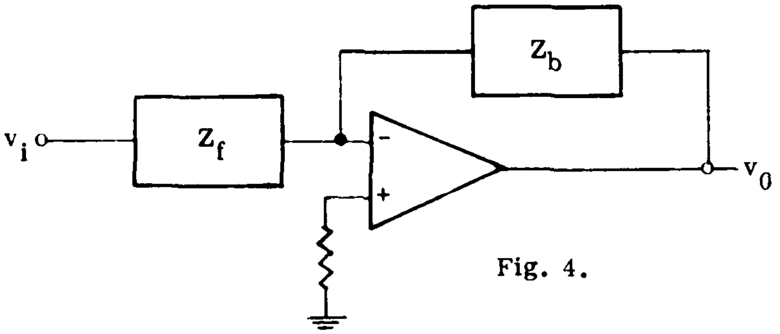

Fig. 4.

The impedance representation of Fig. 4 has been obtained at a particular value of $v_0 = g$. Still this does not stop us from obtaining its transfer function, since we can always consider small enough inputs such that the variation in Z_b can be arbitrarily bounded. It is in this sense that the transfer function obtained this way is a "snap-shot" of a varying frequency response.

For the inverting op-amp circuit in Fig. 4, the transfer function is,

$$H(s) = -\frac{Z_b}{Z_f} = \frac{\frac{1}{sC_2} \cdot R_b \Big/ \left(\frac{1}{sC_2} + R_b\right)}{\frac{1}{sC_1} + R_1}$$

$$= \frac{sR_bC_1}{(1+sC_2R_b)(1+sC_1R_1)} \ .$$

The magnitude of the frequency response can be obtained from H(s) as,

$$H_M(f) = g \cdot \left[\frac{f^2}{(f^2+a^2)(f^2+b^2)}\right]^{1/2} \ , \tag{15}$$

where

$$g = \frac{1}{2\pi C_2 R_1} = 8.84 \times 10^4 \tag{16}$$

and the two system poles are,

$$a = \frac{1}{2\pi C_1 R_1} = 3.9789 \text{ Hz} \tag{17}$$

and

$$b = \frac{1}{2\pi C_2 R_b} \quad . \tag{18}$$

Formulas (15) and (16) indicate that the cut-on pole at $f = a$ is fixed at 4 Hz, while the cut-off pole at $f = b$ varies with $R_v(g)$, i.e., its location is a function of the output level.

Returning to the frequency response in Eq. (15), it is easily shown that the maximum occurs at the frequency,

$$f_M = \sqrt{ab} \tag{19}$$

and the value of the maximum transfer is

$$H_M(f_M) = \frac{g}{a+b} \quad . \tag{20}$$

The important conclusion from (19) and (20) is that both f_M and $H_M(f_M)$ being functions of b, are themselves functions of the output voltage.

From the above "snap-shot" frequency response analysis of the circuit, we find that "b" is the critical parameter of the circuit. From (18), b, in turn, depends upon R_b, the equivalent feedback resistance, and it is this critical variable that we shall now analyse.

The equivalent feedback resistance,

$$R_b = R_T \| R_{v,pnp} \| R_{v,npn} = R_T \| R_v(|v_0|) \quad , \tag{21}$$

since only one transistor is active depending upon the polarity of the output v_0. From this expression one can immediately identify three distinctly different regions of operation for the circuit as follows:

Region I – Constant Gain Region. In this region, $R_v(v_0) \gg R_T$, i.e., the output level is small enough that

$$R_v(v_0) = R_0 \cdot e^{-|v_0|/E_0} \gg R_T \ .$$

Then, $R_b \simeq R_T$ and from Eqs. (14) through (16) it follows that,

$$b = \text{upper 3 dB cut-off} = 502.3 \text{ Hz}$$

$$f_M = \sqrt{ab} = 44.8 \text{ Hz}$$

and

$$H_M(f_M) = 174.58$$

i.e.,

$$H_M(w) \simeq H_M(f_M) \ , \qquad a < w < b \ . \tag{22}$$

But,

$$H_M(f_M) = \frac{g}{a+b} = \frac{C_1 R_b}{C_2 R_b + C_1 R_1}$$

and since $C_2 R_b \ll C_1 R_1$,

$$H_M(f_M) = \frac{C_1 R_b}{C_1 R_1} = \frac{R_b}{R_1} \ , \tag{23}$$

and Eq. (22) becomes

$$H_M(w) \simeq \frac{R_b}{R_1} \ . \tag{24}$$

This is a significant result. It states that for $v_i(t)$ bandlimited to $(a, b)_{min}$ the "gain" of the bandpass circuit is approximately independent of frequency. In other words, the capacitors, C_1 and C_2, have only a marginal effect on gain. They primarily perform waveshaping and high frequency noise suppression.

Equation (24) gives us the output voltage dependent "gain" that we were seeking in Eq. (4). Thus,

$$\frac{v_0}{v_i} = G(v_0) \simeq H(w) \simeq -\frac{R_b}{R_1} \tag{25}$$

the -ve sign being due to the inverting configuration of the operational amplifier. Therefore,

$$v_i = -\frac{R_1}{R_b} \cdot v_0 = -\left(\frac{R_1}{R_T} + \frac{R_1}{R_v}\right) v_0 \ ,$$

i.e.,

$$v_i = -\frac{v_0}{G_1} - \frac{1}{G_2} v_0 \cdot 10^{-v_0/E_0} \ , \tag{26}$$

where $G_1 = R_T/R_1$ and $G_2 = R_0/R_1$.

Region II – Logarithmic Gain Region. This region is characterized by $R_v(v_0) \ll R_T$, i.e., the output level is large enough that

$$R_v(v_0) = R_0 10^{-|v_0|/E_0} \ll R_T \ .$$

In this case, $R_b \simeq R_v(v_0)$. Again, b, f_M, and $H_M(f_M)$ can be computed from Eqs. (14) - (16) for a fixed v_0. The important observation, however, is that

$$R_b \Big|_{\text{REGION II}} \leq R_b \Big|_{\text{REGION I}}$$

and, therefore, b and f_M can only be larger than the small signal values of Region I. Similarly, $H_M(f_M)$ can only be smaller than in Region I.

Region III – Transition Region. This region, of course, corresponds to those values of the output for which $R_v(v_0) \sim R_T$. The amplifier has neither constant nor logarithmic gain and hence the term "transition region."

The plot of $R_v(v_0)$, R_T, and R_b versus v_0, below, shows the three regions.

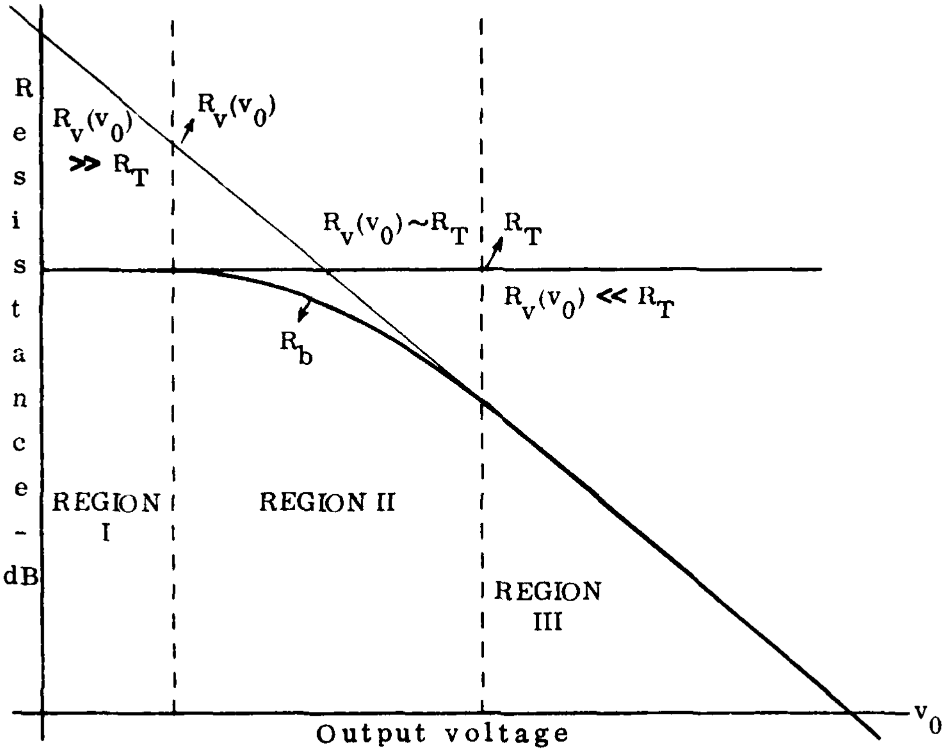

Fig. 5. Plot of the Feedback Resistance, R_b, versus the Output Voltage, v_0

We now have all the necessary information to complete our task of obtaining a closed-form expression for the transfer characteristic of the logging circuit. This is done next in Step 3.

Step 3. The Approximate Output-Voltage-Dependent Gain and the Output-to-Input Transfer Expression.

The family of frequency responses found in the previous section can be plotted for some typical values of R_b as in Figure 6.

In this plot, note that in the frequency band (4,502.3) Hz, the responses are flat to within 3 dB of their respective maximum values.

This frequency range, of course, is the pass-band for small output levels. It follows that if we consider input signals which are bandlimited to

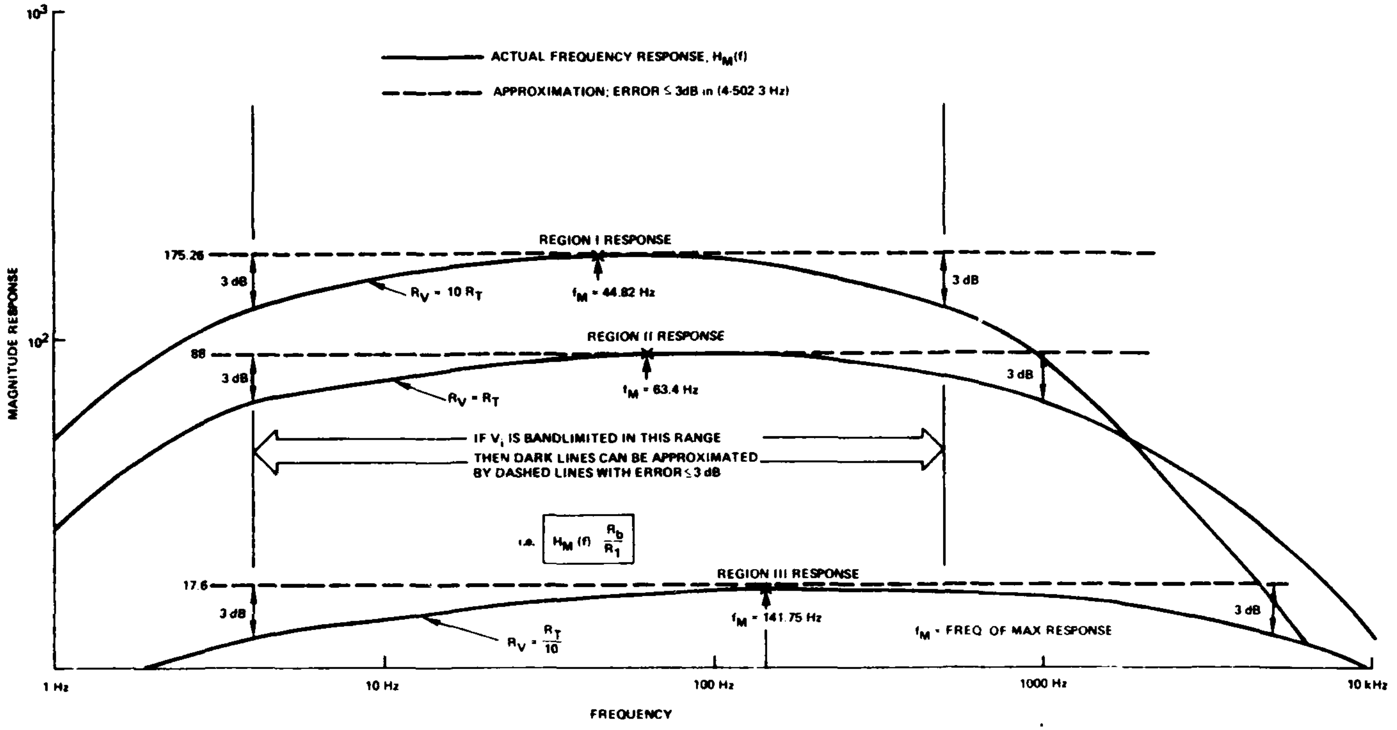

Fig. 6. Plot of three representative Frequency Response Curves in each region of circuit operation. The approximation $H_M(f)=R_b/R_1$ (i.e., frequency independent, v_0 dependent) produces error $\leq$ 3 dB in the minimum passband of the circuit (in Region I) of 4 Hz to 502.38 Hz.

within $(a, b)_{\min}$ then for such input the frequency response can be approximated by the maximum value, $H_M(f_M)$ with a known bounded error of ≤ 3 dB and the transformation $d(t) = 5.68\ v_0(t) + 2.5$ can be used to obtain v_i vs. d from Eq. (26). Thus,

$$v_i = -\frac{(d-2.5)}{5.68G_1} - \frac{(d-2.5)}{5.68G_2} \cdot 10^{-(d-2.5)/5.68E_0} ,$$

i.e.,

$$v_i = \frac{2.5}{5.68G_1} - \frac{1}{5.68G_1} d + \frac{2.5}{5.68G_2} \cdot 10^{2.5/5.68E_0} \cdot 10^{-d/5.68E_0}$$

$$- \frac{1}{5.68G_2} \cdot 10^{2.5/5.68E_0} \cdot d \cdot 10^{-d/5.68E_0}$$

or

$$v_i = a_0 + a_1 d + a_2 10^{-d/e_0} + a_3 \cdot d \cdot 10^{-d/e_0} , \tag{27}$$

where $e_0 = 5.68E_0$

$$a_1 = -\frac{1}{5.68G_1}$$

$$a_0 = \frac{2.5}{5.68G_1} \qquad a_2 = \frac{2.5}{5.68G_2} \cdot 10^{2.5/5.68E_0}$$

$$a_3 = -\frac{1}{5.68G_2} \cdot 10^{2.5/5.68E_0} .$$

Finally, the transfer expression in terms of peak-to-peak input and output values is,

$$v_{i,p-p} = a_1 d_{p-p} + a_2 \left[10^{-d_h/e_0} - 10^{-d_\ell/e_0} \right]$$

$$+ a_3 \left[d_n 10^{-d_h/e_0} - d_\ell \cdot 10^{-d_\ell/e_0} \right] , \tag{28}$$

i.e., due to the non-linear form of (27) the peak-to-peak transfer expression requires a knowledge not only of $d_{p-p} = d_h - d_\ell$, but also of the actual minimum and maximum output levels, d_h and d_ℓ, themselves. This information has not been recorded in the calibration data. Therefore, to fit an expression to the calibration data, we heuristically fit a function of the form of (26)

$$v_{i,p-p} = \frac{d_{p-p}}{x_3} + x_1 \cdot d_{p-p} \cdot 10^{d_{p-p}/x_2} \quad . \tag{29}$$

The constants x_1, x_2, and x_3 were determined via iterative regression for each channel. Results of the fit for the channels $S1^+$ through $S9^+$ are included as Figures 7-15.

REFERENCES

Sheingold, Daniel H., Ed., Non-linear Circuits Handbook, Analog Devices, Inc., Norwood, Mass., 1976

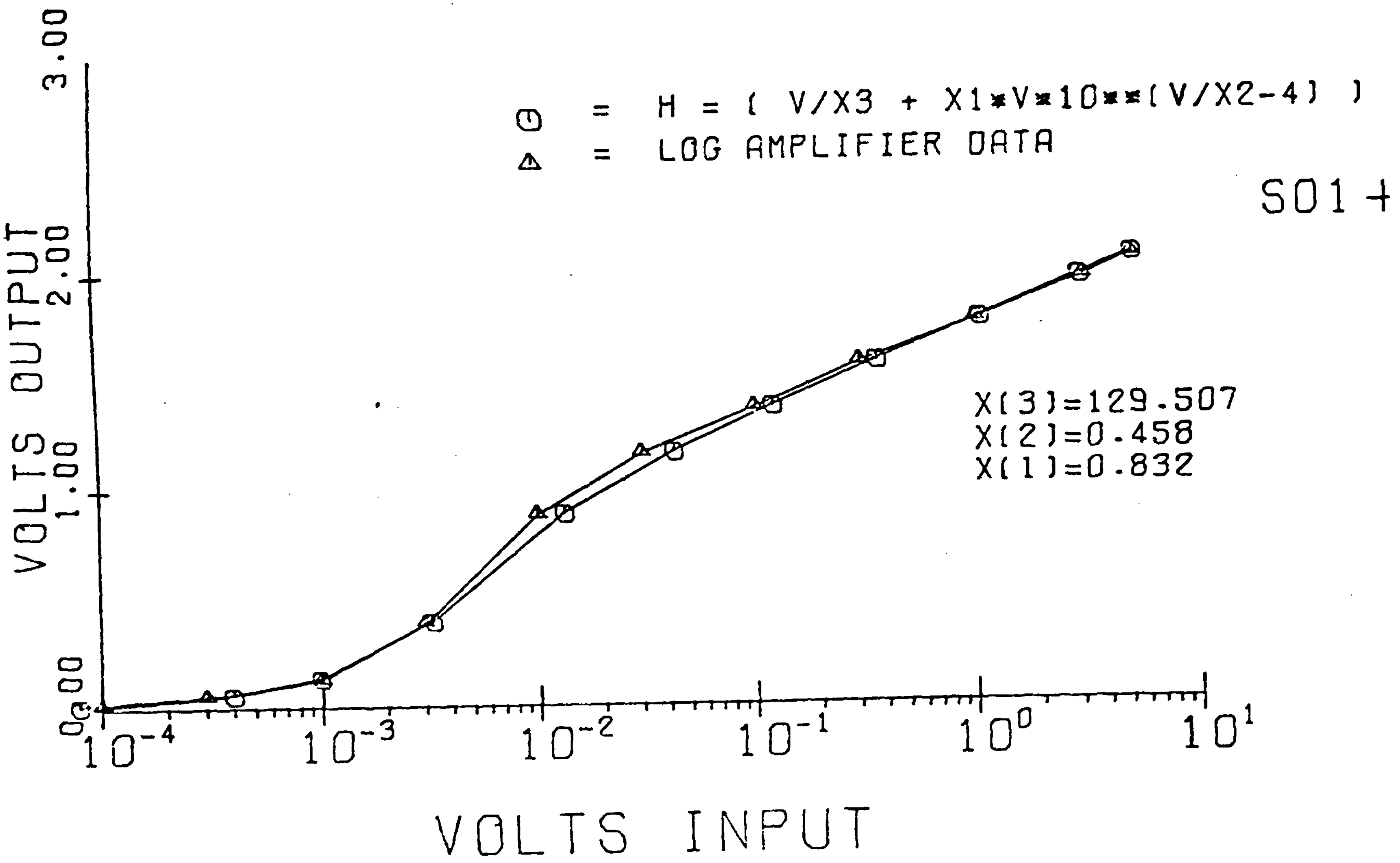
⊖ = H = (V/X3 + X1*V*10**(V/X2-4))
△ = LOG AMPLIFIER DATA
S01+
X(3)=129.507
X(2)=0.458
X(1)=0.832
VOLTS OUTPUT
3.00
2.00
1.00
0.00
VOLTS INPUT
10^-4
10^-3
10^-2
10^-1
10^0
10^1

Figure 7

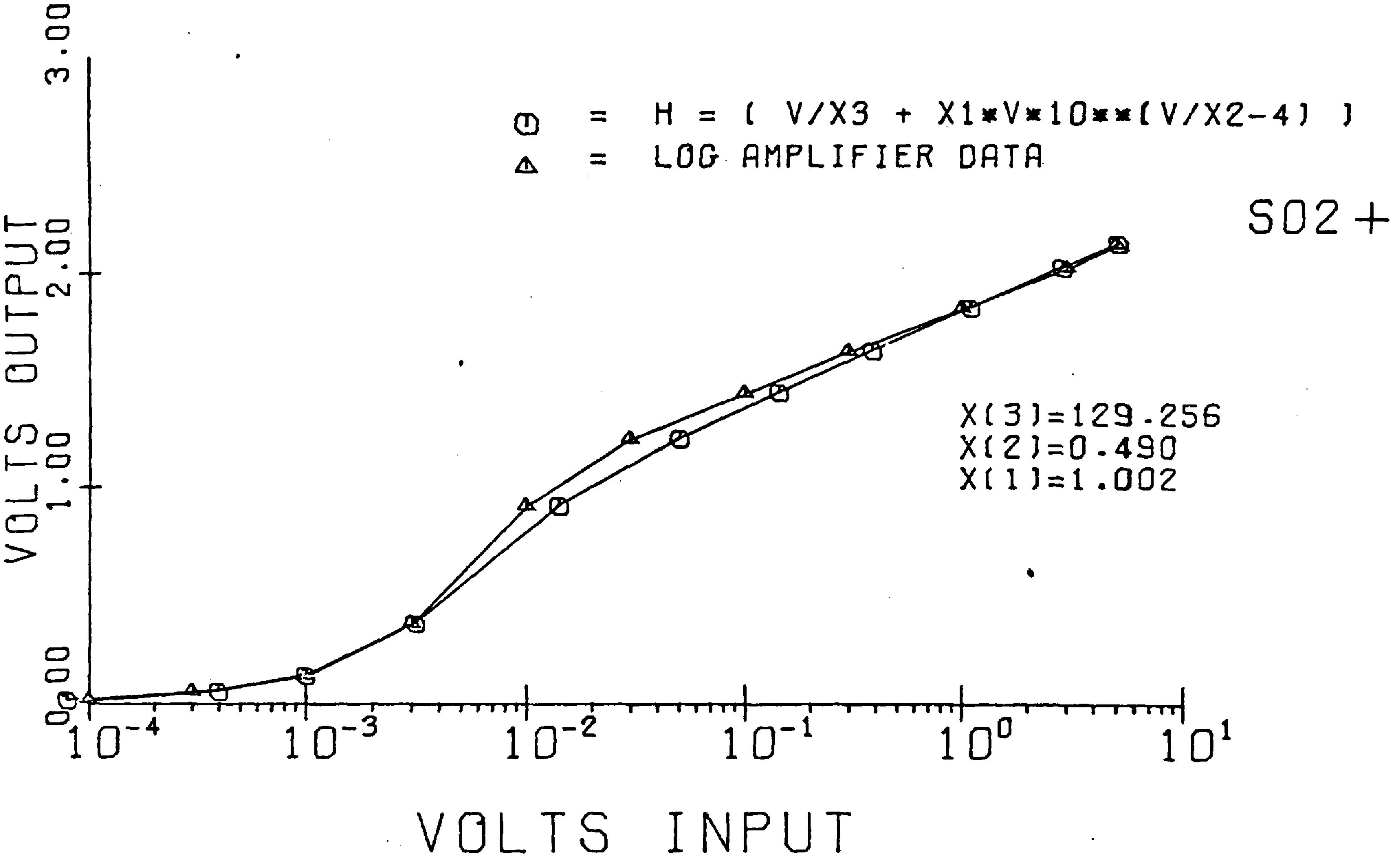

⊕ = H = (V/X3 + X1*V*10**(V/X2-4))
△ = LOG AMPLIFIER DATA
SO2+
X(3)=129.256
X(2)=0.490
X(1)=1.002
VOLTS OUTPUT
0.00
1.00
2.00
3.00
VOLTS INPUT
10^{-4}
10^{-3}
10^{-2}
10^{-1}
10^{0}
10^{1}

Figure 8

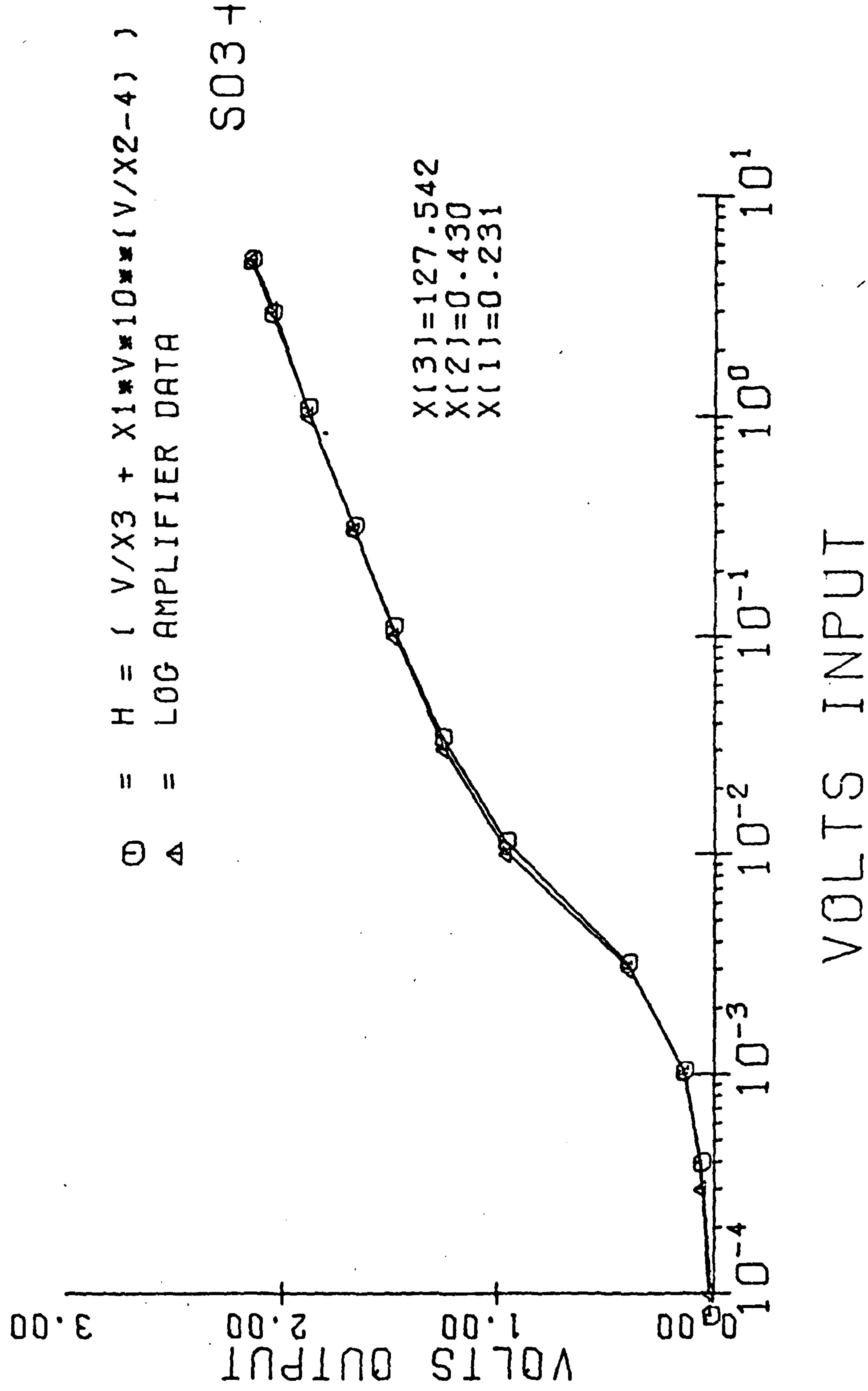
⊖ = H = (V/X3 + X1*V*10**(V/X2-4))
△ = LOG AMPLIFIER DATA
SO3+
X(3)=127.542
X(2)=0.430
X(1)=0.231
VOLTS OUTPUT
0.00
1.00
2.00
3.00
VOLTS INPUT
10^{-4}
10^{-3}
10^{-2}
10^{-1}
10^{0}
10^{1}

Figure 9

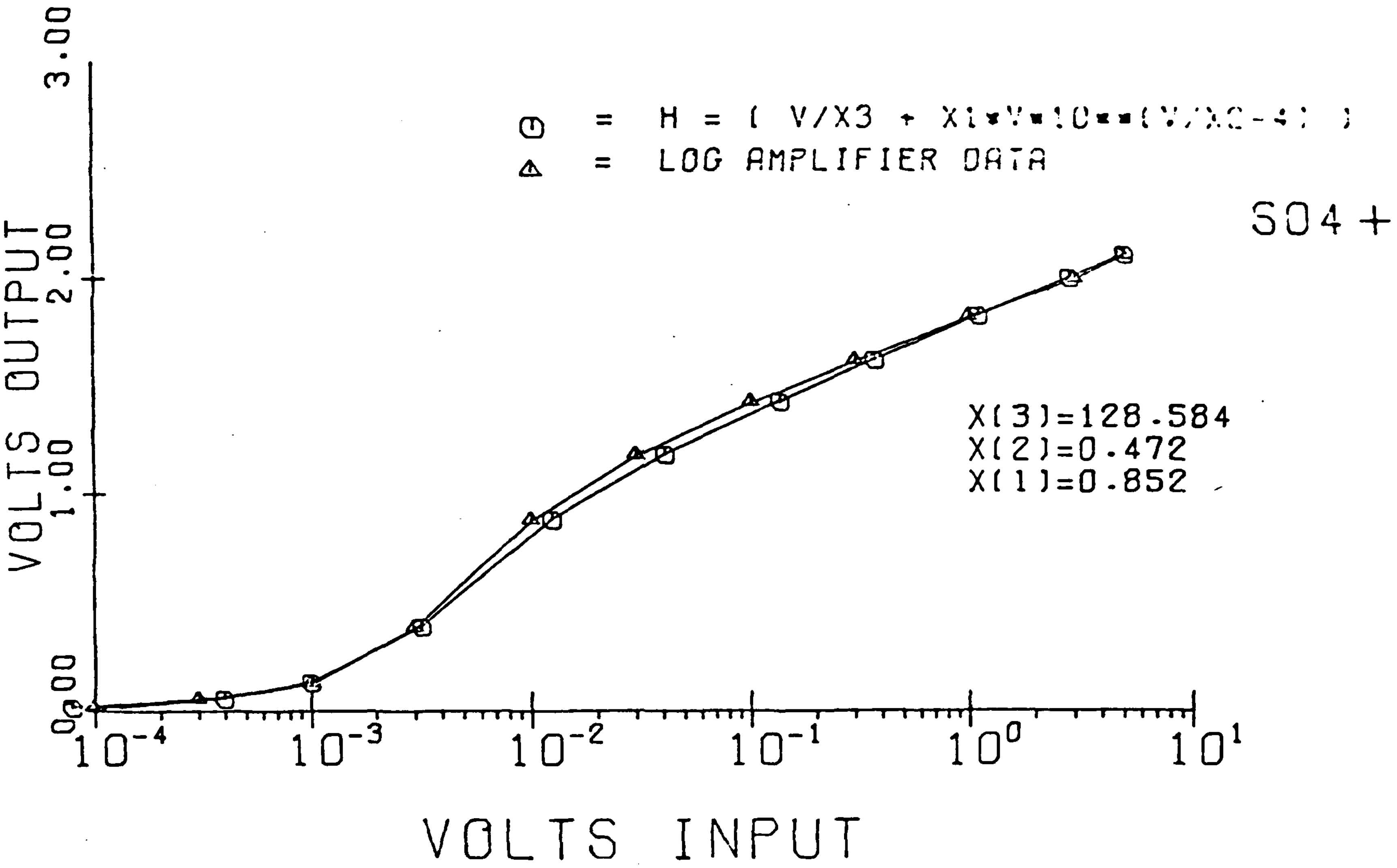
⊖ = H = (V/X3 + X1*V*10**(V/X2-4))
△ = LOG AMPLIFIER DATA
SO4+
X(3)=128.584
X(2)=0.472
X(1)=0.852
VOLTS OUTPUT
0.00
1.00
2.00
3.00
VOLTS INPUT
10^{-4}
10^{-3}
10^{-2}
10^{-1}
10^{0}
10^{1}

Figure 10

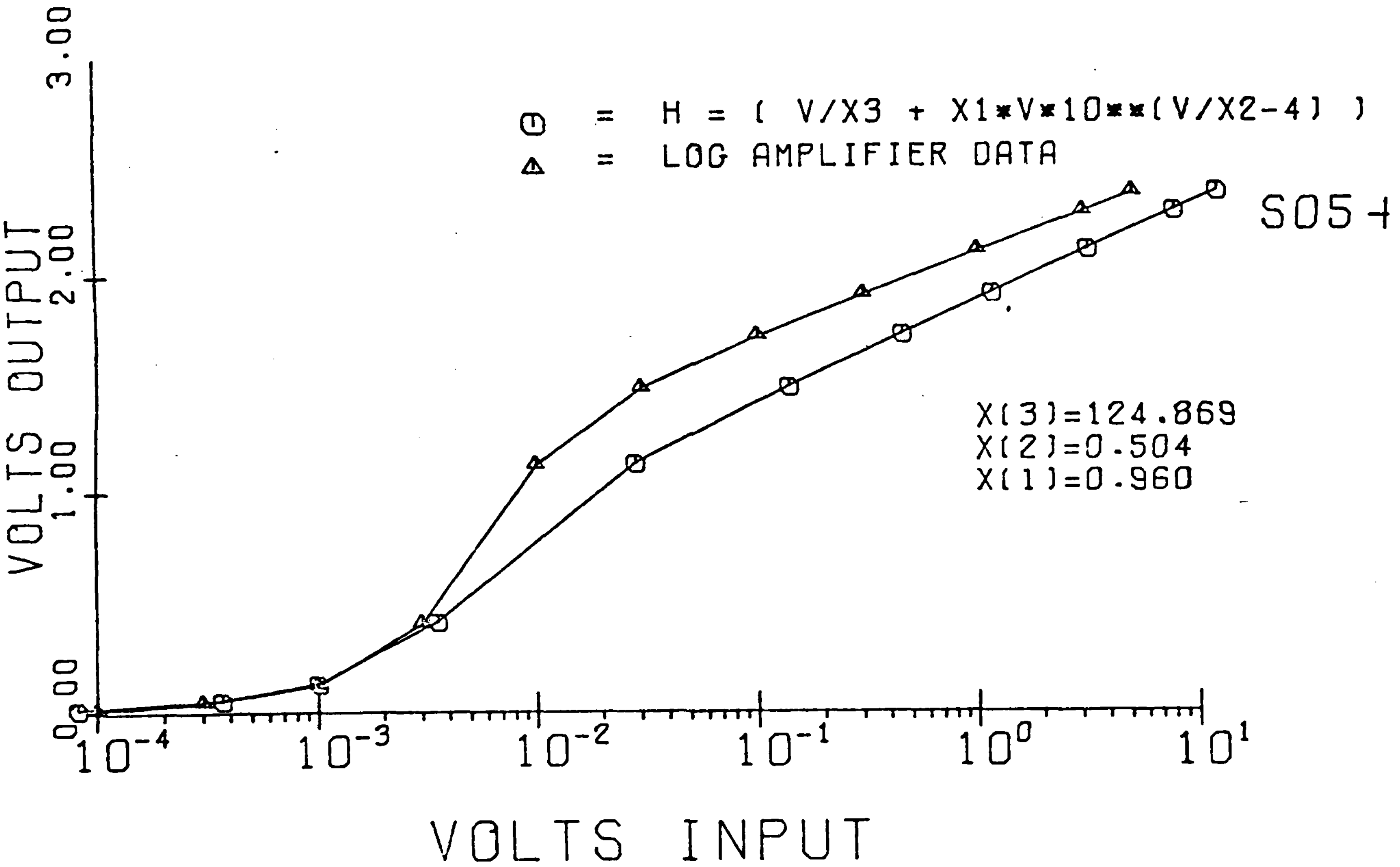
○ = H = (V/X3 + X1*V*10**(V/X2-4))
△ = LOG AMPLIFIER DATA
S05+
X(3)=124.869
X(2)=0.504
X(1)=0.960
VOLTS OUTPUT
3.00
2.00
1.00
0.00
10^{-4}
10^{-3}
10^{-2}
10^{-1}
10^{0}
10^{1}
VOLTS INPUT

Figure 11

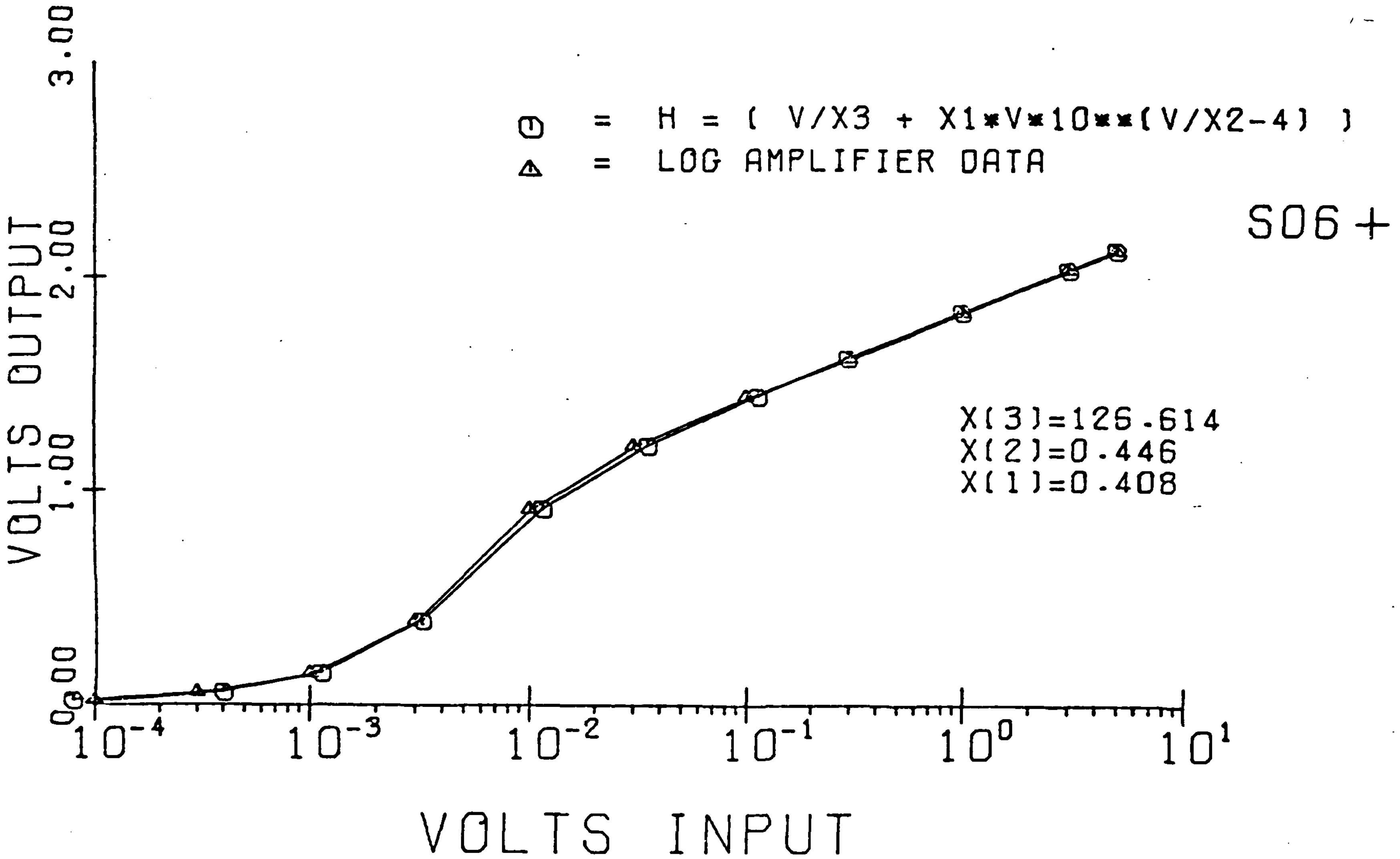

⊖ = H = (V/X3 + X1*V*10**(V/X2-4))
△ = LOG AMPLIFIER DATA
S06+
X(3)=126.614
X(2)=0.446
X(1)=0.408
VOLTS OUTPUT
0.00
1.00
2.00
3.00
VOLTS INPUT
10^-4
10^-3
10^-2
10^-1
10^0
10^1

Figure 12

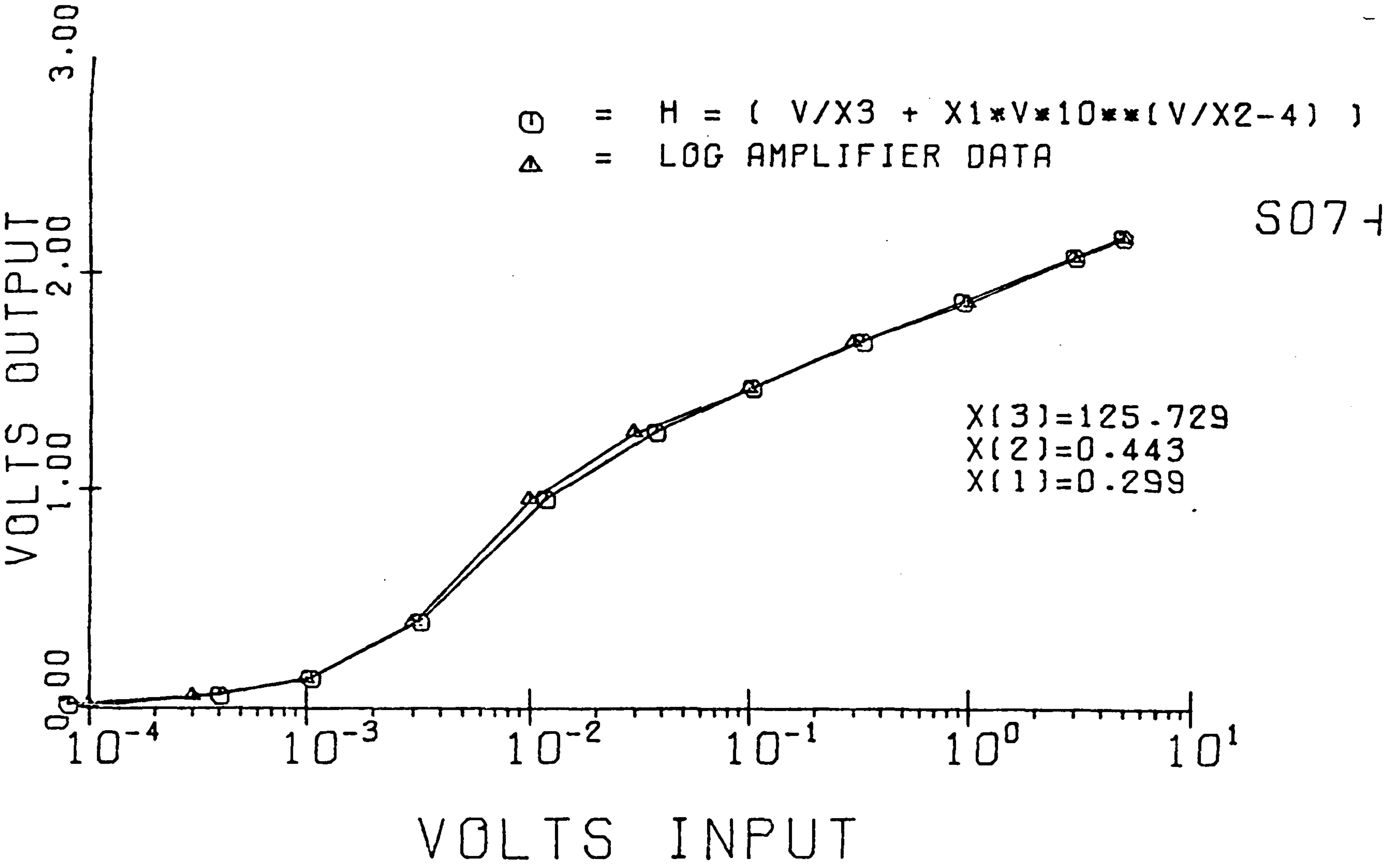
⊖ = H = (V/X3 + X1*V*10**(V/X2-4))
△ = LOG AMPLIFIER DATA
S07-I
X(3)=125.729
X(2)=0.443
X(1)=0.299
VOLTS OUTPUT
0.00
1.00
2.00
3.00
VOLTS INPUT
10^{-4}
10^{-3}
10^{-2}
10^{-1}
10^{0}
10^{1}

Figure 13

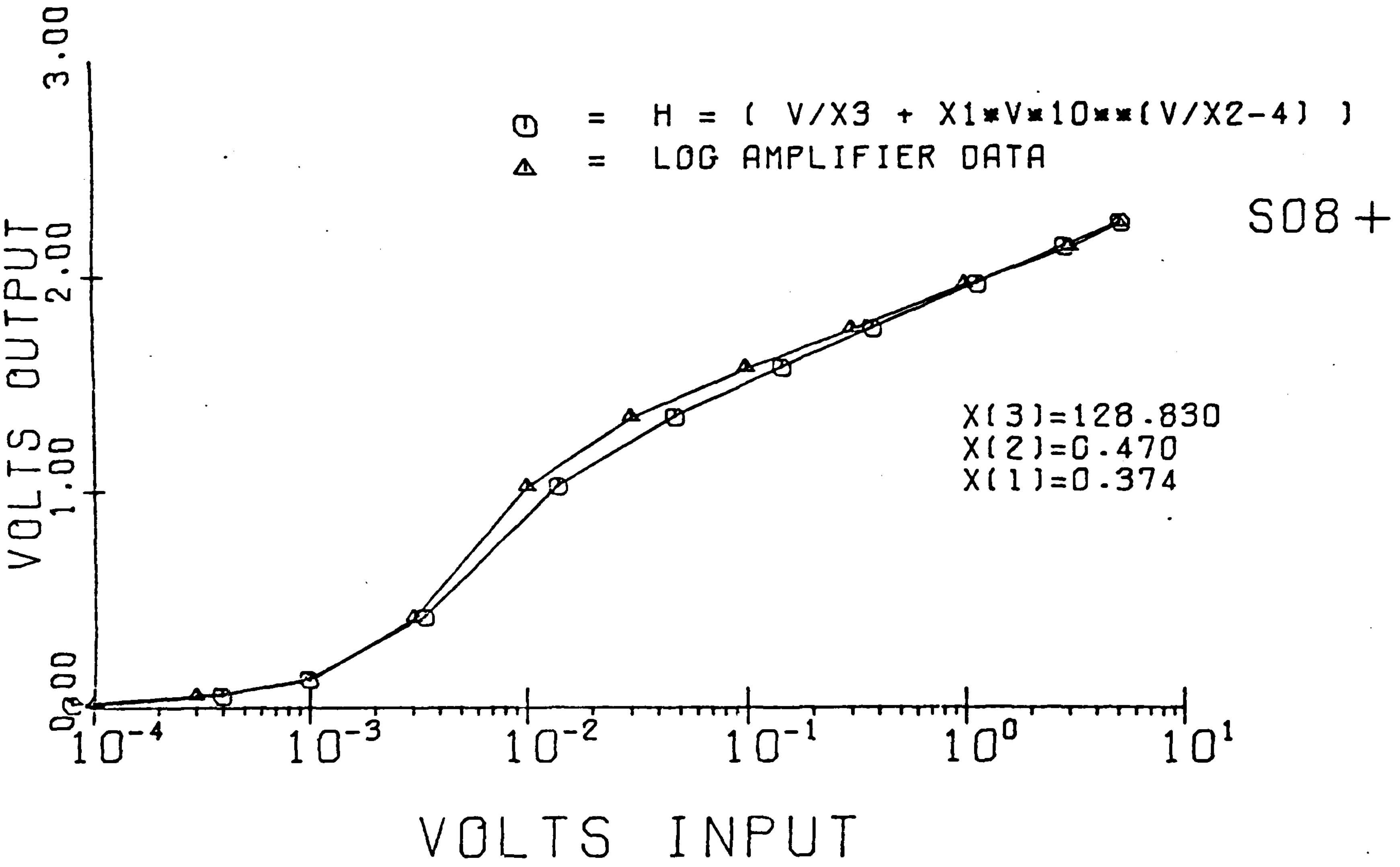

3.00
2.00
1.00
0.00
VOLTS OUTPUT
○ = H = (V/X3 + X1*V*10**(V/X2-4))
△ = LOG AMPLIFIER DATA
S08+
X(3)=128.830
X(2)=0.470
X(1)=0.374
10⁻⁴
10⁻³
10⁻²
10⁻¹
10⁰
10¹
VOLTS INPUT

Figure 14

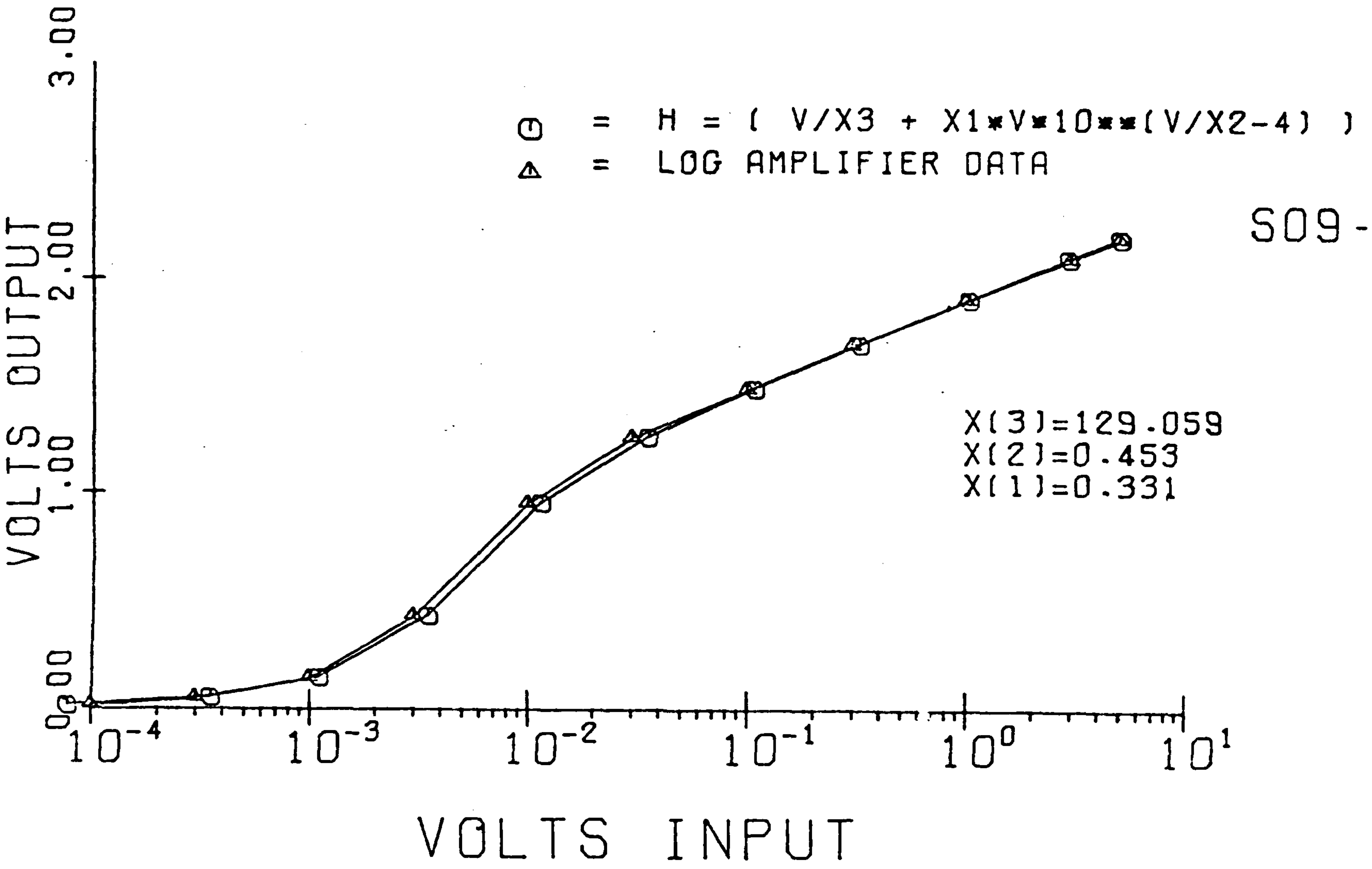

3.00
2.00
1.00
0.00
VOLTS OUTPUT
10^{-4}
10^{-3}
10^{-2}
10^{-1}
10^{0}
10^{1}
VOLTS INPUT
○ = H = (V/X3 + X1*V*10**(V/X2-4))
△ = LOG AMPLIFIER DATA
S09-
X(3)=129.059
X(2)=0.453
X(1)=0.331

Figure 15

APPENDIX A1

The expression for R_v, the incremental variable resistance of the logging transistors can be obtained as follows: For the grounded-base configuration (known as the "Transdiode" logging configuration) the modified Ebers and Moll equation for the collector current is

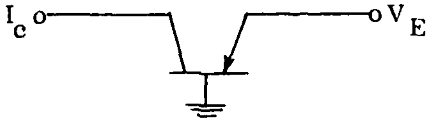

$$I_c = \alpha_N I_{ES}\left(e^{qv_E/KT} - 1\right) - I_{cS}\left(e^{qv_c/KT} - 1\right) - \sum I_{cs_j}\left(e^{qv_c/M_jKT} - 1\right)$$

where v_E = Emitter-base voltage

v_c = collector-base voltage

α_N = forward current transfer ratio

α_I = *reverse current transfer ratio*

$M_j > 1$ are the "uncollected" current components that flow through the base circuit

$q = 1.60219 \times 10^{-19}C$; $K = 1.38062 \times 10^{-23} J/°K$

$T = °K = °c + 273.15$

Since $v_c \simeq 0$ due to the virtual ground at the -ve terminal of the op-amp

$$I_c = \alpha_N I_{ES}\left(e^{qv_E/KT} - 1\right)$$

$$v_E = \frac{KT}{q} \ln\left[\frac{I_c}{I_{ES}}\right] - \frac{KT}{q}\ln \alpha_N \quad \text{for} \quad \frac{I_c}{\alpha_N I_{ES}} \gg 1 \; .$$

Now α_N is close to unity and fairly constant over the entire range of currents. Neglecting the last term (which for $\alpha_N = .99$ contributes (1/4) mv offset),

$$v_E = \frac{KT}{q} \times 2.303 \times \log \frac{I_c}{I_{ES}} = E_0 \log \frac{I_c}{I_{ES}} \; .$$

Then,

$$R_v = \frac{dv_E}{dI_c} = \text{incremental resistance at } V_E = \frac{E_0}{2.303 I_c} = \frac{KT}{qI_c} ,$$

i.e.,

$$R_v = \frac{KT}{q\alpha_N I_{ES}\left(e^{qv_E/KT} - 1\right)} = \frac{.031292928}{I_{ES}} \cdot \frac{1}{e^{v_E/.031293} - 1}$$

$$= R_0 \cdot \frac{1}{10^{v_E/E_0} - 1} ,$$

where

$$R_0 = \frac{.03129292737}{I_{ES}} \quad \text{and} \quad E_0 = 72.054627 \text{ millivolts.}$$

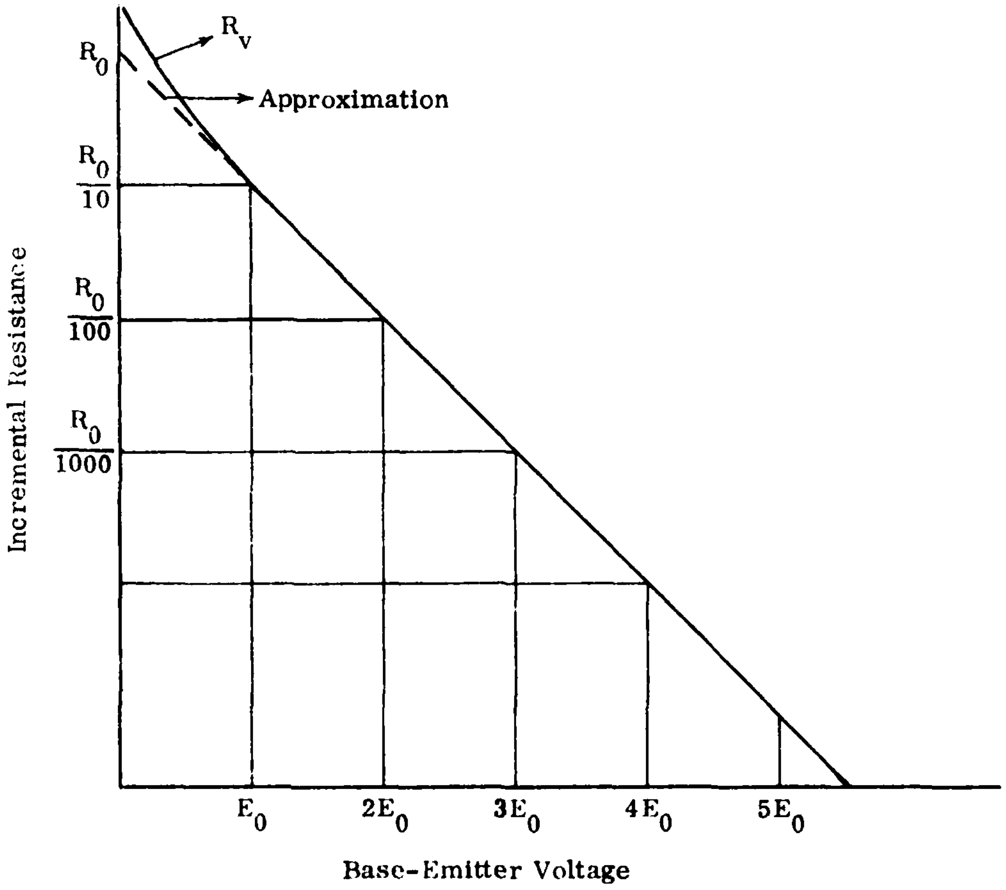

R_v is plotted above as a function of the emitter-base voltage, v_E. For $v_E \geq E_0$, the resistance falls by a decade for every E_0 increase in v_E. This fundamental property is being used to produce the logarithmic compression in the circuit. Observe that for $0 < v_E < E_0$. the resistance deviates from the above rule. In fact, R_v is infinite for $v_E = 0$ (the transistor is cut off).

Neglecting the "1" in the denominator, which is valid for $V_E/E_0 > 1$,

$$R_v = R_0 \cdot \frac{1}{10^{v_E/E_0}} \Longrightarrow R_v = R_0 \cdot 10^{-v_E/E_0} .$$

This effect of the approximation is that the true R_v (solid line) is being approximated by the dotted line for $0 < v_E < E_0$.

We now need I_{ES} to compute R_0. In the specifications sheet provided us, the base-emitter junction has been characterized, as shown below, by

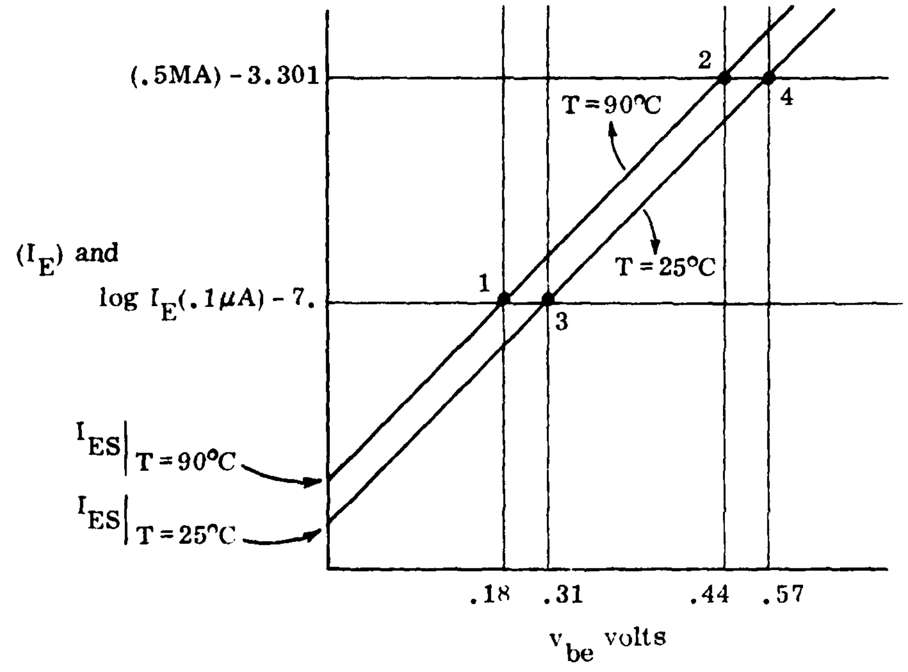

the four points shown on the I_E vs. v_{be} graph for T = 25°C and T = 90°C. Since the circuit operates at T = 90°C, we are interested in $I_{ES}\big|_{T=90^\circ C}$. This is the intercept of the upper line. Let

$$x_\tau = v_{be}\Big|_{T=\tau} \quad \text{and} \quad y_\tau = \log I_E\Big|_{T=\tau} .$$

Then, we seek to fit the line $y_\tau = mx_\tau + C$. For T = 90°C, the scope, m, and intercept, c, are obtained using points #1 and #2 in the junction characteristics. The resulting equation of the line is

$$y_{90^\circ C} = 14.2269 x_{90^\circ C} - 9.56122 .$$

Hence,

$$I_{ES}\Big|_{T=90^\circ C} = 10^{-9.56122} = 0.27465 \times 10^{-9}$$

and substituting into formula for R_0, one obtains,

$$R_0 = 1.1393 \times 10^8 = 113.93 \text{ M}\Omega .$$

Also, $E_0 = 1/m = 70.289$ mv, directly from the slope 'm'.

Compare this value of E_0 with the value $E_0 = 72.05$, obtained earlier from the physical equations describing the transistor.

A MODEL FOR SATELLITE CHARGING AT HIGH ALTITUDES

Initiator: A. Rubin
Problem No.: 4017
Project No.: 7661

Satellites in geosynchronous orbit have been found to charge up electrically during magnetic substorms leading to circuit upsets and malfunction of satellites. To understand the physical processes taking place it is necessary to calculate the details of the spacecraft charging process.

A computer program was developed to conduct numerical simulations of plasma interactions with a satellite, assuming the satellite to be represented by an infinitely long cylinder and treating the plasma as discrete particles. The system is assumed to be uniform along the axis of the satellite. A number of features of the actual satellite are incorporated into the model with as much flexibility as possible to accommodate a wide range of conditions.

PARTICLE MOTIONS

The particles are treated as discrete objects rather than as fluid elements but do not necessarily represent individual ions or electrons. The current design associates with each computer particle a cluster of identical electrons or ions so that the several million particles of the actual plasma are represented by a few thousand computer particles. In contrast to an earlier model with spherical symmetry, the parameter relating the number of real particles for each computer particle is a constant for all particles.

The particle motions are determined by the electric field produced by the satellite and by the particles themselves. The program allows the satellite to be charged to an arbitrary voltage and also allows the potential in the plasma far from the satellite to be set, thus influencing the rate at which particles emerge from the far plasma and enter the region near the satellite. The electric field is calculated from the electric potential obtained by solving Poisson's equation in a cylindrical geometry.

Thus, the equation to be solved for the potential ϕ is:

$$\frac{1}{r}\frac{\partial}{\partial r}\left(r\frac{\partial\phi}{\partial r}\right)+\frac{1}{r^2}\frac{\partial^2\phi}{\partial\theta^2}=\frac{-\rho}{\epsilon}$$

assuming uniformity is the z-direction. With a coordinate transformation $S = \ln r$, this equation becomes:

$$\frac{\partial^2\phi}{\partial S^2}+\frac{\partial^2\phi}{\partial\theta^2}=\frac{-r^2\rho}{\epsilon} \quad ,$$

which is the form for rectangular coordinates, using a modified density $r^2\rho$.

This transformation is effected by choosing the radial gridpoints to have uniform increments in $\ln r$, rather than as an explicit coordinate transformation. A standard Poisson-solving routine (8) for rectangular coordinate systems is then employed to find the potential, using the modified charge density. This approach also requires an auxiliary routine to solve for the potential on the satellite itself, to provide a necessary boundary condition for the Poisson solver. The auxiliary routine uses a moment series expansion to determine the satellite potential in terms of the charge distribution and the constant value assumed for the potential in the far plasma region.

There are also provisions for allowing a uniform magnetic field which has the field aligned along the cylinder axis.

Particles are "lost" from the system by striking the surface of the satellite or escaping from the region studied, and are added to the system by a variety of emission processes on the satellite, described below, or by entering into the region studied from the surrounding plasma.

SECONDARY EMISSION

Ions or electrons which strike the satellite are assumed to generate secondary electrons, taking into account both the energy and angle of incidence of the impacting particle to determine the yield of secondary electrons.

The equation used to evaluate the secondary emission for incident electrons is:

$$\delta = C_0 \left[\frac{1 - \exp\left(-(X_0 E)^n\right)}{(X_0 E)^{n-1}} \right] \exp\left(C_1 [1 - \cos\theta]\right) \quad ,$$

where δ = number of secondary electrons

E = energy of incident electrons

θ = angle of incidence with respect to normal to surface.

The parameters C_0, C_1, and X_0 can be chosen to be different over the angular sectors of the satellite to reflect the properties of different materials with respect to secondary emission.

For incident ions, the equation used is:

$$\delta = \frac{a_0 \sqrt{E} \sec\theta}{1 + E/X_1} \quad ,$$

where a_0 and X_1 reflect properties of the materials in each angular sector of the satellite.

For either incident ions or incident electrons, the emitted secondary electrons are assumed to have a Maxwellian velocity distribution:

$$f(v) \propto v^2 \exp\left(\frac{-v^2}{2b}\right) \quad .$$

The velocity dispersion "b" for the emitted electrons can depend on the species of incident particle, and its value can easily be changed at execution time.

The direction of the velocity of the emitted particles has a cosine distribution in angle with respect to the normal.

The corresponding process for ion emission (sputtering) has not been treated, as the magnitude of that process is relatively small.

BACKSCATTERING

Inelastic collision of electrons with the satellite is treated as a backscattering process, again taking into account the energy and angle of incidence of the impacting particle to determine the yield. The equation used here is:

$$\beta = B_0 \left(\frac{A_0 E}{(E_c + E)^{m+1}} \right)^{\cos\theta} ,$$

where β = number of backscattered electrons

E = energy of incident electrons

θ = angle of incidence with respect to normal to surface.

The parameters A_0 and B_0 can likewise be set to different values on the different angular sectors of the satellite.

The energy of the emitted particles is directly related to the energy of the incident particles, according to $f(v) \propto v^3/E^2$, for incident energy E, provided $m_e v^2/2 \le E$, and again a cosine distribution in angle is assumed.

As with the sputtering process, backscattering of ions is neglected.

PHOTOEMISSION

The emission of photoelectrons from the satellite surface is treated in a manner similar to secondary emission, taking account of the incidence angle of solar illumination and the photoemissive coefficients of the different sectors of the satellite to determine the photoemission yield. Thus, the relevant formula is:

$$\epsilon = k_0 f(\cos\alpha) ,$$

where ϵ = number of photoelectrons per unit time per unit surface area

f = solar illumination flux

α = angle of solar illumination with respect to normal to surface.

The solar flux is essentially zero or one, depending upon whether the sector is in shadow or not, while k_0 is a photoemission coefficient which can be set to different values for different sectors of the satellite.

Currently, the velocity spectrum of the emitted photoelectrons is assumed to be a Maxwellian with the cosine angular dependence previously assumed for secondaries.

PARTICLE BEAMS

Corresponding to the particle beams on the satellite, there is a routine which emits particles from a localized region of the satellite in a beam pattern. The beam pattern is given according to a $1/\theta_0 \cos \theta/\theta_0$ law, for $0 \leq \theta \leq \theta_0$, and the velocity distribution of the beam particles can be chosen to be either monochromatic ($v = v_0$ for all particles) or Maxwellian $\left(f(v) \propto v^2 \exp\left(-v^2/2v_0^2\right)\right)$. There are effectively separate particle beams for ions and electrons, and, in addition to θ_0 and v_0, the location, aiming direction, and current for each beam can be specified.

An option is available by which the total charge emitted by the beams can be linked to the total satellite charge, thus influencing the potential on the satellite.

ELECTROSTATIC POTENTIAL CALCULATIONS FOR A CYLINDRICAL MODEL

Introduction

Recent investigations of spacecraft interaction with the surrounding plasma have led to the development of a two-dimensional model for numerical simulations. This model treats the spacecraft as an infinitely long cylinder and studies the motion of particles in the cylindrical annulus between the spacecraft and an arbitrary boundary at some distance into the plasma. To represent the motion of the particles properly, it is necessary to perform calculations of the electric field which is established by the distribution of charges in the region and by imposed potentials on the spacecraft. This section describes the potential calculation method that has been implemented.

Poisson's Equation

For a system with translational symmetry in the Z-direction (along the axis of the spacecraft cylinder), Poisson's equation is:

$$\frac{1}{r}\frac{\partial}{\partial r}\left(r\frac{\partial\phi}{\partial r}\right)+\frac{1}{r^2}\frac{\partial^2\phi}{\partial\theta^2}=-\frac{\rho(r,\theta)}{\epsilon}\ \text{(MKS units)}\quad,$$

where the electrostatic potential is ϕ, and ρ is the charge density (per unit area). The charges are effectively infinitely long rods in this representation and interact via a logarithmic potential.

Converting the above form of Poisson's equation to suitable form for a discrete grid gives:

$$\frac{2r_i}{D_{i-1}}\left[\frac{r_i\phi_{i+1,j}}{\Delta_i}-\phi_{i,j}\left(\frac{r_i}{\Delta_i}+\frac{r_{i-1}}{\Delta_{i-1}}\right)+\frac{r_{i-1}\phi_{i-1,j}}{\Delta_{i-1}}\right]$$

$$+\frac{\phi_{i,j+1}-2\phi_{i,j}-\phi_{i,j-1}}{\delta^2}=\frac{-r_i^2\rho_{i,j}}{\epsilon}$$

where $\phi_{i,j}=\phi(r_i,\theta_j)$, $\rho_{i,j}=\rho(r_i,\theta_j)$, $\delta=\theta_j-\theta_{j-1}$, $\Delta_i=r_{i+1}-r_i$, and $D_i=r_{i+2}-r_i$.

For a uniform interval in the radial grid points, this form produces coefficients of $\phi_{i,j}$, $\phi_{i\pm1,j}$ which depend on i. However, if Δ_i is proportional to r_i, these coefficients are constant.

Thus, letting $\Delta_i=\alpha r_i$, so that $D_i=\alpha(2+\alpha)r_i$, Poisson's equation becomes:

$$\frac{2(1+\alpha)}{\alpha^2(2+\alpha)}\left[\phi_{i+1,j}-2\phi_{i,j}+\phi_{i-1,j}\right]+\frac{\phi_{i,j+1}-2\phi_{i,j}+\phi_{i,j-1}}{\delta^2}=\frac{-r_i^2\rho_{i,j}}{\epsilon}\quad.$$

This formulation corresponds to a transformation of the radial coordinate according to $S=\ell n\, r$, which gives

$$\frac{\partial^2\phi}{\partial S^2}+\frac{\partial^2\phi}{\partial\theta^2}=-\frac{\tilde{\rho}}{\epsilon}\quad,$$

where $\tilde{\rho}=r^2\rho$ for the transformed density in (S,θ) coordinates.

The charge density is determined from the number of charges within a particular grid cell, but each charge is treated as being uniformly distributed over a cell in (S, θ) coordinates, rather than (r, θ) coordinates. This is implemented by assuming a charge density distribution $\rho = C_{ij}/r^2$ for each cell, normalized according to $\int \rho r \, dr \, d\theta = q_{ij}$, and then using the average of $r^2 \rho$ over the cell for the right side of Poisson's equation. Thus, $r^2 \rho_{i,j}$ is replaced by $-q_{i,j}/[\delta \ell n (1+\alpha)]$ in the formula above.

Note that different charges within a cell do not interact, and only the net charge within a cell contributes to the potential. Thus, the grid produces a potential that is both "softer" (reduced short-range interaction) and "smoother" (spatially averaged) than the actual interparticle interaction.

Boundary Conditions for the Model

In solving Poisson's equation, the boundary conditions must be specified at some radius in the far plasma (R_B) and over some surface on or within the spacecraft. The spacecraft itself is modeled as a conducting cylinder completely surrounded by a dielectric layer. This allows the charge distribution on the surface of the spacecraft to be that determined only by particle impacts and emission mechanisms, yet allows for the specification of a unique fixed potential for the spacecraft. Conceptually, therefore, the two boundaries are concentric cylinders with a constant potential on each. However, neither potential is necessarily constant in time. In particular, if the spacecraft potential is not fixed, it will "float" with respect to the outer boundary potential, depending on the charge distribution in the intervening region.

If the boundary condition is left solely in terms of the potential on the interior conducting cylinder ($r = R_i$), then the routine for solving Poisson's equation must also involve the conditions at two interfaces: the conductor/dielectric interface and the dielectric/vacuum interface. However, if the interior boundary condition is transformed into a specification of the potential on the outer surface of the spacecraft ($r = R_p$), then Poisson's equation need only be solved over a homogeneous region.

This transformation can be accomplished by solving for the surface potential for the case of an isolated charge, given the potential at the outer boundary and the specification of the potential on the interior conductor ("floating" or fixed potential). The solution for an arbitrary charge distribution is then the appropriate superposition of solutions for isolated charges. (This is essentially a Green's function approach.)

For a charge q at (r_c, θ_c), with $\phi = \phi_0$ at $r = R_1$ (the inner conducting cylinder) and $\phi = \phi_1$ at $r = R_B$ (the far plasma), the potential at (R_p, θ) (on the surface of the spacecraft) is given by:

$$\phi(R_p, \theta) = a_1\phi_0 + a_2\phi_1 + a_3 \frac{q}{2\pi\epsilon} + \sum_{n=1}^{N/2} \cos n(\theta - \theta_c)$$

$$\times \left[\left(C_n + \frac{q}{2\pi n \epsilon r_c^n} \right) R_B^n - \left(C_n R_p^{2n} + \frac{q r_c^n}{2\pi n \epsilon} \right) \frac{1}{R_p^n} \right] ,$$

where $a_1 = \dfrac{\kappa \ln (R_p/R_B)}{\kappa \ln (R_p/R_B) + \ln (R_i/R_p)}$, $\quad a_2 = \dfrac{\ln (R_i/R_p)}{\kappa \ln (R_p/R_B) + \ln (R_i/R_p)} = 1 - a_1$,

$$a_3 = \frac{-\ln (r_c/R_B) \ln (R_i/R_p)}{\kappa \ln (R_p/R_B) + \ln (R_i/R_p)} = -a_2 \ln (r_c/R_B) \ , \quad \text{and}$$

$$C_n = \frac{-q}{2\pi\epsilon n r_c^n} \left[\frac{\left(R_p^{2n} + r_c^{2n}\right)\left(R_p^{2n} - R_i^{2n}\right) - \kappa \left(R_p^{2n} - r_c^{2n}\right)\left(R_p^{2n} + R_i^{2n}\right)}{\left(R_p^{2n} + R_B^{2n}\right)\left(R_p^{2n} - R_i^{2n}\right) - \kappa \left(R_p^{2n} - R_B^{2n}\right)\left(R_p^{2n} + R_i^{2n}\right)} \right] .$$

In principle, the summation should be extended to $n = \infty$, but on a discrete grid it is restricted according to the number of angular sectors N ($= 2\pi/\delta$). For the case of a floating potential on the spacecraft, with a total charge Q_i on the interior cylinder,

$$\phi_0 = \phi_1 - \frac{Q_i}{2\pi\kappa\epsilon} \left[\kappa \ln \left(\frac{R_p}{R_B} \right) + \ln \left(\frac{R_i}{R_p} \right) \right] - \frac{q}{2\pi\epsilon} \ln \left(\frac{r_c}{R_B} \right) .$$

Some modifications to the above expressions are required to accommodate the convention of having the charges distributed over each cell, rather than as discrete charges. This is accomplished by a superposition of the above solutions for a charge density

$$\rho = \frac{q}{\delta \ln(1+\alpha)\, r^2}$$

over the region $r_c/(1+\alpha) < r \leq r_c$, $\theta_c \leq \theta < \theta_c + \delta$. This produces a potential $\tilde{\phi}(R_p, \theta)$, with

$$\begin{aligned}\tilde{\phi}(R_p, \theta) &= a_1\phi_0 + a_2\phi_1 + b_1 \frac{q}{2\pi\epsilon} \\ &+ \frac{q}{2\pi\epsilon\delta \ln(1+\alpha)} \sum_{n=1}^{N/2} \frac{2}{n^3} \sin\left(\frac{n\delta}{2}\right) \cos n\left(\theta - \theta_c - \frac{\delta}{2}\right) \\ &\times \left\{ \left(\frac{R_p}{r_c}\right)^n \left[A_n\left(1 - \frac{R_B^{2n}}{R_p^{2n}}\right) - 1\right] [1 - (1+\alpha)^n] \right. \\ &\left. + \left(\frac{r_c}{R_p}\right)^n \left[B_n\left(\frac{R_B^{2n}}{R_p^{2n}} - 1\right) - 1\right] \left[1 - \frac{1}{(1+\alpha)^n}\right] \right\} ,\end{aligned}$$

where a_1 and a_2 are as before,

$$b_1 = \ln(R_p/R_i) \left[\frac{\ln(r_c/R_B) - \frac{1}{2}\ln(1+\alpha)}{\kappa \ln(R_p/R_B) + \ln(R_i/R_p)} \right]$$

$$A_n = R_p^{2n} \left[\frac{\left(R_p^{2n} - R_i^{2n}\right) - \kappa\left(R_p^{2n} + R_i^{2n}\right)}{\left(R_p^{2n} + R_B^{2n}\right)\left(R_p^{2n} - R_i^{2n}\right) - \kappa\left(R_p^{2n} - R_B^{2n}\right)\left(R_p^{2n} + R_i^{2n}\right)} \right]$$

and

$$B_n = R_p^{2n} \left[\frac{\left(R_p^{2n} - R_i^{2n}\right) + \kappa\left(R_p^{2n} + R_i^{2n}\right)}{\left(R_p^{2n} + R_B^{2n}\right)\left(R_p^{2n} - R_i^{2n}\right) - \kappa\left(R_p^{2n} - R_B^{2n}\right)\left(R_p^{2n} + R_i^{2n}\right)} \right] .$$

The condition for a floating spacecraft potential then becomes

$$\phi_0 = \phi_1 - \frac{Q_i}{2\pi\kappa\epsilon}\left[\kappa \ln\left(\frac{R_p}{R_B}\right) + \ln\left(\frac{R_i}{R_p}\right)\right] - \frac{q}{2\pi\epsilon}\left[\ln\left(\frac{r_c}{R_B}\right) - \frac{\ln(1+\alpha)}{2}\right] .$$

The solution is now completely formulated, given a method of solving Poisson's equation in rectangular coordinates. For this particular application, Hockney's$^{(8)}$ Fourier Analysis/Cyclic Reduction Method was employed. The Fourier transform routine for Hockney's programs is also used to obtain the superposition of solutions for setting the boundary potentials at $r = R_p$.

REFERENCES

(1) DeForest, S.E. (1972) Spacecraft charging at synchronous orbit, *J. Geophys. Res.* 77:651.

(2) Rosen, A. (1975) *Spacecraft Charging: Environment Induced Anomalies*, AIAA Paper 75-91, AIAA Conference, Pasadena, CA.

(3) Inouye, G.T. (1975) *Spacecraft Potentials in a Substorm Environment*, in Spacecraft Charging by Magnetospheric Plasmas, A. Rosen, Editor, MIT Press, Cambridge, MA.

(4) Parker, L.W. (1975) *Computer Method for Satellite Plasma Sheath in Steady-State Spherical Symmetry*, AFCRL-TR-75-0410, AD A015 066.

(5) Rothwell, P.L., Rubin, A.G., Pavel, A.L., and Katz, L. (1975) *Simulation of the Plasma Sheath Surrounding a Charged Spacecraft*, in Spacecraft Charging by Magnetospheric Plasmas, A. Rosen, Editor, MIT Press, Cambridge, MA.

(6) Rothwell, P.L., Rubin, A.G., and Yates, G.K. (1977) *A Simulation Model of Time-Dependent Plasma-Spacecraft Interactions*, Proceedings of the Spacecraft Charging Technology Conference, C.P. Pike and R.R. Lovell, Editors, AFGL-TR-77-0051, AD A045 459.

(7) Katz, L., Parks, D.E., Wang, S., and Wilson, A. (1977) *Dynamic Modeling of Spacecraft in a Collisionless Plasma*, Proceedings of the Spacecraft Charging Technology Conference, C.P. Pike and R.R. Lovell, Editors, AFGL-TR-77-0051, AD A045 459.

(8) Hockney, R.W. (1970) The potential calculation and some applications, in Methods in Computational Physics, Vol. 9, Academic Press, N.Y.

SPLINE SMOOTHING OF RADIANCE MEASUREMENTS

Initiator:	Mr. S. Price
Problem No.:	3036
Project No.:	7670

The task under this problem number was to develop one-dimensional and two-dimensional flexible knot least squares spline smoothing algorithms. These smoothing techniques were applied to infrared radiance measurements as a function of galactic latitude and longitude.

Least Squares Approximations and Splines

This section deals primarily with one- and two-dimensional least squares spline approximations to univariate and multivariate data, but the principle applies in general to smoothing measured data by approximating the data with an optimal vector from a designated vector space. In the case of cubic splines, the designated vector space consists of twice continuously differentiable functions which are locally cubic polynomials. In the case of least squares polynomial approximations the designated vector space consists of all polynomials of degree $\leq n$.

I. One-Dimensional Cubic Splines

A cubic spline approximation of a function f(t) defined on an interval I consists of local cubic polynomial approximations to f(t) over subintervals of I in such a way that the local approximating curves over contiguous intervals join together in a smooth fashion.

Definition: Let $P = \{x_1, x_2, \ldots, x_n\}$ be a partition of the interval [a, b], i.e., $a = x_1 < x_2 < \cdots < x_n = b$.

A function s(t) which is twice continuously differentiable on [a, b] and is a cubic polynomial on each sub-interval (x_i, x_{i+1}), $1 \leq i \leq n-1$ is called a cubic spline. The $x_1, x_2, \ldots, x_n$ are called knots for the spline interval [a, b].

Let S(P, [a, b]) denote the set of all cubic splines with knots $P = \{x_1, x_2, \ldots, x_n\}$ over the interval [a, b]. If P and [a, b] are understood, then S replaces S(P, [a, b]).

There are two basic uses of cubic splines – interpolation and smoothing. Cubic spline interpolation consists of finding a function s in S satisfying

$$s(x_i) = y_i \ , \qquad 1 \leq i \leq n \tag{1}$$

for a given set of pairs $(x_1, y_1), \ldots, (x_n, y_n)$. A fundamental result of Spline Theory states that there exists a piecewise cubic function s satisfying (1) and, furthermore, the solution s is unique if the additional constraints $s'(x_1) = c$ and $s'(x_n) = d$ are introduced. The problem of least squares cubic spline approximation consists of finding a function s in S which minimizes

$$\sum_{j=1}^{M} \{s(t_j) - y_j\}^2 \tag{2}$$

for a given set of data values (t_j, y_j), $1 \leq j \leq M$.

Both the interpolation and the smoothing problem become more mathematically tractable by introducing vector space terminology. We observe that the sum of two cubic splines is again a cubic spline and a scalar times a cubic spline is a cubic spline, that is, S is a vector space. The following result (Prenter, Splines and Variational Methods, Wiley-Interscience, 1975, p. 80) is fundamental for the computation of spline fits.

Theorem: The dimension of S is n + 2.

Consequently, if $c_1, c_2, \ldots, c_{n+2}$ is a basis for S then the solution of (2) consists of finding constants $a_1, a_2, \ldots, a_{n+2}$, which minimize $\Sigma\, \epsilon_i^2$, where

$$\begin{bmatrix} \epsilon_1 \\ \epsilon_2 \\ \vdots \\ \epsilon_M \end{bmatrix} = \begin{bmatrix} y_1 \\ y_2 \\ \vdots \\ y_M \end{bmatrix} - \begin{bmatrix} c_1(t_1) & c_2(t_1) & \cdots & c_{n+2}(t_1) \\ c_1(t_2) & c_2(t_2) & \cdots & c_{n+2}(t_2) \\ \vdots & & & \\ c_1(t_M) & c_2(t_M) & \cdots & c_{n+2}(t_M) \end{bmatrix} \begin{bmatrix} a_1 \\ a_2 \\ \vdots \\ a_{n+2} \end{bmatrix} . \qquad (3)$$

We can rewrite (3) as the matrix equation, $y = CA + \epsilon$, and in this form, the desired least squares solution is given by

$$A = \left(C^t C\right)^{-1} C^t Y \ ,$$

or, alternatively,

$$A = C^+ Y \ ,$$

where $C^+ = \left(C^t C\right)^{-1} C^t$ is the pseudo-inverse of the matrix C. Thus, the solution of the least-squares problem can be reduced to selecting a computationally convenient basis for S and then finding the pseudo-inverse of the matrix C which is generated by the basis functions. The basis functions found to be most convenient are those referred to as B-splines. In the following, we introduce the definition of *splines and B-splines using* the approach of deBoor. For deBoor the concept of spline is more general than that introduced above, but the two notions of spline coincide for twice continuously differentiable *cubic splines*. *Following deBoor*, a least squares spline approximation is developed for splines of general degree rather than an algorithm restricted to piecewise cubic polynomials.

Definition: (deBoor, p. 108). Let $\tilde{t} = (t_i)$ be a non-decreasing sequence. The i^{th}-normalized B-spline of order k for the knot sequence $\tilde{t}$ is denoted $B_{i,k,\tilde{t}}$ and is defined by the rule

$$B_{i,k,\tilde{t}}(x) = (t_{i+k} - t_i)\,[t_i, \ldots, t_{i+k}](\cdot - x)_+^{k-1}$$

for all real numbers x.

Notes: (1) for cubic splines, $k = 4$

(2) $[t_i, t_{i+1}, \ldots, t_{i+k}]$ is a divided difference and may be computed in the case of distinct knots by the rule,

$$[t_i, t_{i+1}, \ldots, t_{i+k}](f) = \frac{f(t_i)}{\{(t_i - t_{i+1})(t_i - t_{i+2}) \cdots (t_i - t_{i+k})\}}$$

$$+ \frac{f(t_{i+1})}{\{(t_{i+1} - t_i)(t_{i+1} - t_{i+2}) \cdots (t_{i+1} - t_{i+k})\}}$$

$$\vdots$$

$$+ \frac{f(t_{i+k})}{\{(t_{i+k} - t_i)(t_{i+k} - t_{i+1}) \cdots (t_{i+k} - t_{i+k-1})\}}$$

(3) the definition of deBoor permits knots to coalesce; each case of equality of adjacent knots reduces the smoothness requirement at that knot by 1; the cases treated herein deal only with distinct knots.

Remark: Let the knots for the space S be $x_1, x_2, x_3, \ldots, x_n$. To generate a basis for S, the above set of knots is extended (in a somewhat arbitrary manner) and the normalized B-splines generated for the extended set of knots yielding the desired basis. More concretely, let Δ be some positive number. Define the extended knot sequence $t_1, t_2, \ldots, t_{n+6}$ by

$$t_1 = x_1 - 3\Delta, \quad t_2 = x_1 - 2\Delta, \quad t_3 = x_1 - \Delta, \quad t_{3+i} = x_i, \qquad 1 \le i \le n$$

$$t_{n+3+j} = x_n + j \cdot \Delta, \qquad 1 \le j \le 3$$

and let $B_{i,4,\tilde{t}}(x)$ be the normalized B-splines for the extended knot set $\tilde{t} = \{t_1, t_2, \ldots, t_{n+6}\}$. Set $B(i,x) = B_{i,4,\tilde{t}}(x)$. As a consequence of Theorem IX.1, deBoor, p. 113, we have the following result.

Theorem: $B(1,x), B(2,x), \ldots, B(n+2,x)$ is a basis for S.

Note: The fact that $t_1, t_2, t_3, t_{n+4}, t_{n+5}, t_{n+6}$ are arbitrary is discussed in deBoor, p. 114.

I.1 Least Squares – One-Dimensional Cubic Spline

For observed data $(t_1, y(t_1)), \ldots, (t_e, y(t_e))$ and specified knots $x_1, x_2, \ldots, x_n$, the least squares cubic spline approximation models the data as:

Model: $S(t) = \alpha_1\ B(1,t) + \alpha_2\ B(2,t) + \cdots + \alpha_{n+2}\ B(n+2,t) + \epsilon$, where $B(1,.), \ldots, B(n+2,.)$ are B-splines. Incorporation of observation data into the model yields.

$$\begin{bmatrix} y(t_1) \\ y(t_2) \\ \vdots \\ y(t_e) \end{bmatrix} = \begin{bmatrix} B(1,t_1) & B(2,t_1) & \cdots & B(n+2,t_1) \\ B(1,t_2) & B(2,t_2) & \cdots & B(n+2,t_2) \\ \vdots & \vdots & & \vdots \\ B(1,t_e) & B(2,t_e) & \cdots & B(n+2,t_e) \end{bmatrix} \begin{bmatrix} \alpha_1 \\ \alpha_2 \\ \vdots \\ \alpha_{n+2} \end{bmatrix} + \epsilon$$

$$S = B\alpha + \epsilon .$$

The least squares solution $\hat{\alpha}$ of $S = B\alpha + \epsilon$ is given by

$$\hat{\alpha} = \left(B^t B\right)^{-1} B^t S \ .$$

I.2 Algorithm for Solution of Least Squares Cubic Spline Problem

(i) Specify Knots;	(iv) Read observation data;
(ii) Extend Knots;	(v) Write S, B;
(iii) Define basis functions;	**(vi)** Solve $S = B\alpha + \epsilon$

A computational consideration is that for large data sets, the compact support of the basis functions can be exploited in the implementation of Step 6.

Direct implementation of the definition given above for the B-splines may lead to numerically unstable expressions involving the various difference quotients as pointed out by deBoor. He suggests rather that the recurrence relations,

$$B_{j,1}(x) = \begin{cases} 1 \ , & t_j \leq x \leq t_{j+1} \\ 0 \ , & \text{otherwise} \end{cases}$$

$$B_{i,k}(x) = \frac{x - t_i}{t_{i+k-1} - t_i} B_{i,k-1}(x) + \frac{t_{i+k-x}}{t_{i+k} - t_{i+1}} B_{i+1,k-1}(x) \qquad (*)$$

be exploited in the generation of the B-splines.

RDP used the above algorithms to generate a Fortran program which does spline fits up to order 20. These spline smoothing programs have been run successfully to approximate infrared radiation measurements and to generate calibration curves for infrared detectors relating measured voltage to measured radiance.

II. Two-Dimensional Spline Approximation

The object of this section is to describe a least squares error spline approximation to surfaces $Z = f(x,y)$. A basic assumption is that the surface is defined over a rectangular region in the xy-plane and that a rectangular grid of knots is appropriate for the approximation scheme. The algorithm employed assumes that the knots in the x-direction and the y-direction are independent. If $M_1(y), \ldots, M_n(y)$ are the B-spline basis functions in the y-direction and $L_1(x), \ldots, L_n(x)$ is the corresponding basis in the x-direction then the model is

$$z(x,y) = \sum\sum a_{ij} M_i(y)\, L_j(x) + \epsilon \;. \qquad (1)$$

The basic scheme in the algorithm to be presented is to reduce the two-dimensional spline separately to two one-dimensional spline fits (after Call and Judd). To describe the problem, let

$$x_1, x_2, \ldots, x_{n1} \quad , \qquad y_1, y_2, \ldots, y_{m1}$$

be the knots in the x and y directions, respectively. Further, let

$$L_1(x), L_2(x), \ldots, L_n(x) \quad , \qquad M_1(y), M_2(y), \ldots, M_m(y)$$

be the corresponding B-splines. If the observations are

$$
\begin{aligned}
&x_1, x_2, \ldots, x_n \\
&y_1, y_2, \ldots, y_m \\
&z(x_1, y_1), \ldots, z(x_n, y_1) \\
&z(x_1, y_2), \ldots, z(x_n, y_2) \\
&\vdots \\
&z(x_1, y_m), \ldots, z(x_n, y_m)
\end{aligned}
$$

then the matricial representation of (1) using the measured data is:

$$
\begin{bmatrix}
z(x_1,y_1) & \cdots & z(x_n,y_1) \\
z(x_1,y_2) & \cdots & z(x_n,y_2) \\
\vdots & & \vdots \\
z(x_1,y_m) & \cdots & z(x_n,y_m)
\end{bmatrix}
$$

$$
= \begin{bmatrix}
M_1(y_1) & \cdots & M_m(y_1) \\
M_1(y_2) & \cdots & M_m(y_2) \\
\vdots & & \\
M_1(y_m) & \cdots & M_m(y_m)
\end{bmatrix}
\begin{bmatrix}
a_{11} & a_{12} & \cdots & a_{1n} \\
a_{21} & a_{22} & \cdots & a_{2n} \\
\vdots & & & \vdots \\
a_{m1} & a_{m2} & \cdots & a_{mn}
\end{bmatrix}
\begin{bmatrix}
L_1(x_1) & \cdots & L_1(x_n) \\
L_2(x_1) & \cdots & L_2(x_n) \\
 & & \\
L_n(x_1) & \cdots & L_n(x_n)
\end{bmatrix}
$$

or symbolically,

$$Z = MAL^t \ . \tag{2}$$

The object of the least square fit is to find the coefficients a_{ij} so that the sum of the squares of model values minus the fit values is a minimum. Algebraically, the solution of (2) can be effected in the following manner

$$
\begin{aligned}
&Z = MAL^t \\
\rightarrow\ &\left(M^tM\right)^{-1} M^tZ = AL^t \\
\rightarrow\ &\left\{\left(M^tM\right)^{-1} M^tZ\right\}^t = LA^t
\end{aligned}
$$

(Continued)

$$\rightarrow \left\{ \left(L^tL\right)^{-1} L^t \right\} \left\{ \left(M^tM\right)^{-1} M^tZ \right\}^t = A^t$$

$$\rightarrow A = \left[\left\{ \left(L^tL\right)^{-1} L^t \right\} \left\{ \left(M^tM\right)^{-1} M^tZ \right\}^t \right]^t , \tag{3}$$

where L^t is the transpose of L. Using the notation M^+ for the pseudo-inverse of M, i.e.,

$$M^+ = \left(M^tM\right)^{-1} M^t$$

the solution (3) above can be written simply as

$$A = \left[L^+ \left\{ M^+Z \right\}^t \right]^t . \tag{4}$$

For the fact that M^+Z yields the least squares error solution to the problem $Z = MA + \epsilon$ see, for example, Applied Regression Analysis by Draper and Smith. To generate the values

$$Z(x,y) = \sum a_{ij} M_i(y)\ L_j(x)$$

the following information is needed, in addition to the coefficients a_{ij}, the knots in the x-direction and on the y-direction and a subroutine which generates the basis functions $L_1, \ldots, L_n, M_1, \ldots, M_m$ corresponding to the given knots.

RDP successfully implemented the above two-dimensional smoothing algorithm and applied it to infrared measurements in the galactic plane.

STUDY OF ELECTRON DENSITY PROFILES

Initiator:	Mr. J. Aarons
Problem No.:	4083
Project No.:	4643

A magnetic tape from the Arecibo Observatory containing high resolution electron density measurements was received from the initiator. N(h) data for two nights were analyzed to study the variation of electron density as a function of altitude. A preliminary study of the data showed the existence of large and small scale fluctuations. To study the large scale fluctuations, the electron density was determined at a sequence of distinct height intervals and plotted as a function of time. A spectral analysis of these time series was effected using the FFT technique to determine the period of these waves. For small scale fluctuations, electron density profiles were low pass filtered and the spectra of the residuals analyzed using the Welch averaging technique. Numerical integration of the N(h) profiles was performed to compute total electron content for comparison with ground based measurements.

SIGNAL ANALYSIS OF ROCKET DATA

Initiator: T. Conley
Problem No.: 4854
Project No.: 7660

This problem was to develop a computerized system, including appropriate computer programs and operator instructions, to digitally filter (smooth) unwanted noise from rocket measured radiometer and photometer data (in digital form), correct data for rocket aspect, and digitally differentiate smoothed data to obtain volume emission rates. Current ICECAP rocket radiometer measured data is contaminated by noise induced by the telemetry recording and digitization processes and which leads to erroneous volume emission rates when differentiated.

Considerable data exists at OPR (approximately 10 rocket flights) which were analyzed by this technique.

Sample data was copied from tapes and programs were developed to perform initial processing on the data. Specifically, a noise filter and differentiation filter programs were written and used on the data. These test results were in excellent agreement with known results. The net noise suppression obtained (noise filter minus differentiation) was greater than 60 db. Thus, development of a complete system was undertaken as outlined.

PROCESSING PROCEDURE FOR EMISSION RATE DETERMINATION

I. Establish data file.

Edit data (replace calibration and noise "spike" points in data) using optimal fitting.

Convert to Brightness Unit (Rα).

Plot resulting Rα data vs. time.

Produce and plot FFT of data.

Van Rhijn Aspect Correction ($R_0 = R\alpha/\sqrt{\alpha}$).
Plot resulting $R\alpha$ data vs. time.
Produce and plot FFT of data.

II. Design a noise filter and process data through the filter (possibly separate filters for precession and wideband noise).
Plot filtered data (vs. time).

III. Differentiate output of noise filter (using a differentiation filter).
Plot resulting output (vs. time).
Convert to desired variables (emission rate vs. altitude) and produce plot.

INTRODUCTION

The extraction of volume emission rate estimates from the raw data is difficult since a differentiation of the received signal is required. Since differentiation is a very noisy process (e.g., d/dt[Asin (wt)] = wAcos (wt)) the noise on the received signal will completely mask the desired output after differentiation. Thus, the noise level on the signal must be greatly reduced to allow us to obtain a meaningful estimate of the derivative.

The approach taken (after aspect correction) was to digitally filter the raw data to "optimally" pass the signal while suppressing the noise.(1) Here, typically at least, 80 db reduction of noise level was obtained. The resulting output signal was then differentiated using a digital filter.(2) The differentiation enhances the noise by (at worst) 20 db. Thus, the overall filter (noise filter plus differentiation) yields a net processing gain in excess of 60 db. That is, the S/N (signal-to-noise ratio) out is at least 60 db higher than the input S/N ratio.

FILTER SPECIFICATION

Let us consider a more detailed discussion of the filters used. In general, a numerical filter consists of a set of "weights" W_k which determine the actual transfer function W(f) of the filter. (The design of a numerical filter begins with establishing the shape of the data window in the frequency domain which will give the desired effect.) Having specified the theoretical transfer function, the remainder of the problem consists of determining the weights W_k in such a way that the actual transfer function, or frequency response, approximates the desired one as well as possible. A perfect low pass filter, for example, would leave unaltered all frequency components from $f = 0$ to the desired cutoff frequency f_L and then would suppress all frequencies greater than f_L. The response of an actual numerical filter can only approximate this ideal behavior, with the accuracy of the approximation depending on the values of various design parameters. As in the simple smoothing process, a numerical filter is applied, such that

$$y_0(t) = \sum_{k=-M}^{M} W_k x(t + k\Delta t) \quad .$$

The filtering is accomplished by "sliding" the filter along the data, applying it to 2M + 1 data points to produce the filtered equivalent of the data point which has been multiplied by W_0 and then moving each weight to the next point in the series and repeating the operation. Repetition of the process until all the data in a given run have been covered produces a series of filtered data points which defines the output function $y_0(t)$. Within the precision of the filter these points will trace out the input function x(t) with the unwanted high frequency components removed (if a low pass filter is being used).

The basic form of the filter model is as follows. A nonrecursive (or transversed) filter with linear phase is described by a transfer function.

$$H(Z) = \frac{1}{Z^{2M}} \sum_{k=0}^{M} W_k \left(\frac{Z^{M+k} + Z^{M-k}}{2} \right) \quad .$$

Evaluating the complex variable at $Z = e^{j2\pi F}$ yields the frequency response

$$H(e^{j2\pi F}) = e^{-j2\pi FM} \sum_{k=0}^{M} W_k \cos 2\pi Fk = e^{-j2\pi FM} \, H_0(F) \quad ,$$

where F = fT is the normalized frequency and T is the sampling interval.

With the filter coefficient, W_k, constrained to be real, the frequency response is composed of a linear-phase term, $e^{-j2\pi FM}$, and the purely real frequency response $H_0(F)$ of a zero-phase filter. Since the linear-phase term only introduces a finite delay of M samples, the design problem becomes one of fitting $H_0(F)$, a mirror image polynomial, to the desired frequency responses. That is, determine the coefficients W_k which yield the desired frequency responses for

$$H_0(F) = \sum_{k=0}^{M} W_k \cos 2\pi F k \quad .$$

For the case at hand the weights were chosen to minimize the mean squared error$^{(1)}$ between the actual filter frequency response and an ideal low pass filter with a cutoff frequency chosen in accord with the input signal. Here, a correction factor for the "Gibbs" phenomena was included to provide a smooth transition from the pass band to the stop band of the filter.

The filters used here are specified in the figure below. It was found that narrower filters began to remove some of the signal information while wider filters allowed precession and more noise through with no added signal information. Thus, the bandwidth was chosen to lie between these two conditions.

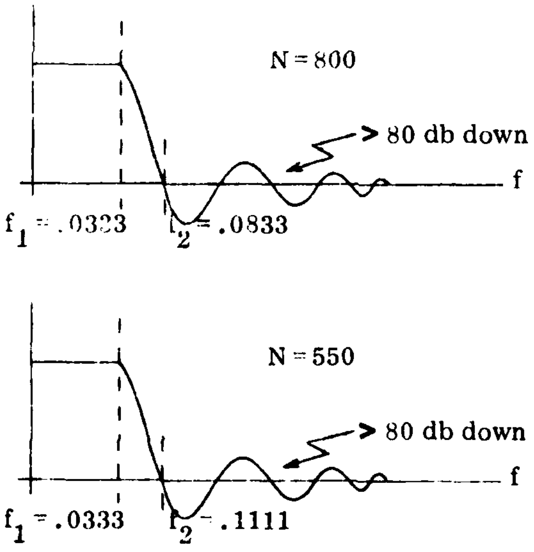

Specification of Noise Filters

Let us consider the differentiation technique employed. The ideal frequency response characteristics of a digital differentiator are shown below. The curves show the magnitude and phase of the frequency response. The magnitude response increases linearly up to a normalized frequency of 1.0 (the Nyquist frequency) and then decreases linearly back to 0.0 at the sampling frequency. The magnitude response is periodic in frequency, as shown, because of the discreteness property. The phase is $\pi/2$ radians for frequencies up to the Nyquist frequency and $-\pi/2$ radians from the Nyquist frequency to the sampling frequency, and is also periodic.

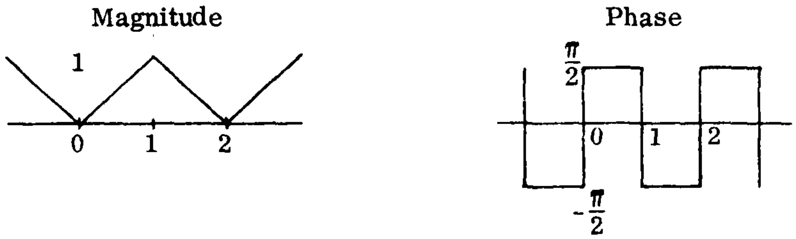

Frequency Response Curves for an Ideal Differentiator

The technique employed to approximate an ideal differentiation filter is given in Reference 2.

In this technique, linearly spaced samples of the frequency response of the desired filter were specified and the continuous frequency response was determined using the discrete Fourier transform. The interpolation formula obtained was

$$H(e^{jwT}) = \frac{\exp\left[-\frac{jwNT}{2}\left(1-\frac{1}{N}\right)\right]}{N} \times \sum_{k=0}^{N-1} \frac{\left[H_k e^{-j\pi k/N} \sin\left(\frac{wNT}{2}\right)\right]}{\sin\left(\frac{wT}{2} - \frac{\pi k}{N}\right)} , \qquad (1)$$

where

$$H_k = H(e^{jwT})\Big|_{w = 2\pi k/NT} , \qquad k = 0, 1, \ldots N-1 \; ; \qquad (2)$$

i.e., $[H_k]$ are values of the continuous frequency response at equally spaced points around the unit circle; T is the sampling period; and N is the duration of the impulse response in samples. By making the substitution

$$H_k = jG_k e^{j\pi k/N} \tag{3}$$

each of the terms inside the summation of (1) becomes imaginary, and thus the entire sum is imaginary. For N even, the complex factor outside the summation in (1) represents a pure delay of an integer ($e^{-jwT(N/2)}$) plus one-half ($e^{-jwT(1/2)}$) number of samples. Thus, (1) suggests that a differentiator with exactly half a sample delay can be designed nonrecursively by setting

$$G_k = \begin{cases} k/(N/2) \ , & k = 0, 1, \ldots, N/2 \\ (n-k)/(N/2) \ , & k = (N/2)+1, \ldots, N-1 \end{cases}$$

and applying the substitution of (3) into (1).

Further details of the design technique and resulting response curves can be found in Reference 2.

For the work described here a differentiation of lengths 128 was employed.

SAMPLING RATE

When experimental data are derived by discretely sampling some phenomenon at equally spaced intervals of time, the problem of aliasing may occur in which the sampling rate is low enough to confuse two or more frequencies in the data.

The net result is that they appear to be the same frequency. To avoid this problem and hence to define a unique input function as described by a set of data points, one must be able to assume that the phenomenon studied is spectrally limited to the range $|f| < f_c$, where $f_c = f_s/2$, f_s being the the cut-off or Nyquist frequency. If such an assumption is valid, then the function has been sampled frequently enough so that all significant frequency components are determinable. This is a result of the sampling theorem of information theory. The sampling theorem states that if a function G(t) contains no frequencies higher than W cycles per second, then it is completely determined by giving its ordinates at a series of points spaced 1/2W seconds apart, the series extending throughout the entire time domain.

Since the bandwidth of the last analog filter before digitizing is approximately 100 Hz, only about 200 to 400 samples per second are required (allowing for the analog filter roll off).

Furthermore, since the desired signal bandwidth was confined to less that 0.1 Hz (as can be seen from the FFT plot), considerable aliasing can be tolerated. That is, sampling rates of 30 to 50 samples per second will only cause aliasing above 0.1 Hz thus not affecting the signal but simply increasing the noise in the higher frequency range. With 60 db processing again this noise increase can be tolerated allowing a lower sampling rate. In fact, a sampling rate of 33 samples per second was used for the processing described here.

REFERENCES

(1) Oppenheim, A.V. and Schafer, R.W., Digital Signal Processing, Prentice-Hall, Inc., Englewood Cliffs, New Jersey, 1975, Chapter 5.

(2) Rabiner, L.R. and Steiglitz, K., "The Design of Wideband Recursive and Non-recursive Digital Differentiators," IEEE Trans. Audio Electro-acoust., Vol. AV-18, pp. 204-209, June 1970.

WAVELENGTH PEAK STUDY

Initiator: T. Conley
Problem No.: 4855
Project No.: 7670

This problem was to develop a computerized system to smooth noise contaminated spectral features in rocket measured CVF data (ICECAP data) in order to accurately specify wavelength of peak emission features and determine line widths.

A noise filter was developed for this data. Also, techniques for "optimal" estimation of peak locations were being studied. In particular, the possible use of full band differentiations (with variance estimates) was studied.

Due to high noise levels and short data spans, it was found that the required accuracy could not be obtained by these techniques. It was decided that further analyses was not warranted at this time. However, the noise filter developed was made available to the initiator.

STATISTICAL ANALYSIS OF GAS MEASUREMENT DATA

Initiator: C.C. Gallagher
Problem No.: 4861
Project No.: 6687

The problem was to develop statistical techniques to identify gas measurements from column and spectrometer tests. Using calibration and test runs, procedures for specifying an identification procedure was to be developed including probability measures of the uncertainties.

A program was developed to calculate the "statistics" of the calibration and test runs and provide student t tests for most probable compounds. Sample data was used to evaluate the approach. The program is described below.

STRATOSPHERE GAS MEASUREMENT ANALYSIS PROGRAM

1. Column Measurement
    A. Establish calibration reference base for time.
    B. Process experimental data (time of arrival and concentration).
        (i) Take as many runs as possible.
        (ii) Establish statistical distribution of time and concentration (e.g., averaging independent samples of time of arrival yields a Gaussian estimate with a variance dependent upon the data stability).
    C. Compare experimental with calibration data to establish "most likely" compounds. Here, one can order possible compounds according to their probabilities. [Note that closest in time is not necessarily most probable.]
2. Process spectrometer data in similar fashion.
3. Check if the results of 1 and 2 agree as to most probable.

(i) If <u>not</u>: perhaps need <u>more data</u>.

A second program was developed to plot and fit gas concentration measurements. Specifically, gases captured during a balloon flight were chemically analyzed. The data from the analyzer was handpunched according to a certain format.

This program plotted gas concentration versus amplitude at different pressures, and then made separate least square fits at each pressure. The plots, therefore, aided the user in extrapolating characteristics of the gas and of the equipment at undetectably low pressures.

SIGNAL STATISTICS OF SCINTILLATION

Initiator: H.E. Whitney
Problem No.: 4893
Project No.: 4643

For this problem RDP, Inc. functioned as mathematical and statistical consultants. Here, we answered a number of questions concerning the "best" procedures for processing and analyzing scintillation data.

Following is a summary of the important results.

COMMENTS AND QUESTIONS CONCERNING THE MAJOR ASPECTS OF THE DATA ANALYSIS

We shall present some comments and questions concerning the data analysis techniques which should be employed for this problem.

Before considering specifics we make the following general remarks:

(1) When the sample size of a data stream is large it is not always necessary (or advisable) to use "optimal" processing procedures. In fact, using "reasonable" approaches often yield results very close to optimal while providing simplicity. However, in general, one should know how one is performing relative to "optimal" so as to justify the procedures employed.

For the problem at hand where the system bandwidth is 2Hz and the data samples are 15 minutes long one has approximately 3600 independent samples per data record. In general, this provides a large number of degrees of freedom, allowing the use of suboptimal techniques.

(2) The desired outputs are critical in determining the techniques to be employed. In particular, the required resolution bandwidth and confidence bars are key factors.

I. Estimate of Auto Correlation Function

The appropriate estimator for the auto correlation function is given by:

$$R_r = \frac{1}{N - r} \sum_{n=1}^{N-r} x_n x_{n+r} , \qquad r = 0, 1, 2, \ldots, M$$

or if N >> M

$$R_r = \frac{1}{N} \sum_{n=1}^{N-r} x_n x_{n+r} , \qquad r = 0, 1, 2, \ldots, M \; ,$$

where $E(x_n) = 0$.

This provides an unbiased estimator with a known variance. Specifically, the variance is approximated by:

$$\mathrm{Var}\,(R_r) = \frac{1}{T^2} \sum_{u=-(T-r)}^{T-r} (T - r - |u|)(R^2(u) + R(u - r)\; R(u + r)) \; .$$

The exact statistics (p.d.f.) of R_r are, in general, not known. However, the variance provides a measure of the quality of the estimate.

Should M be large, one must consider obtaining R_r by employing the FFT approach (Faster and better estimator for large M). Here, one must consider adding zeros to the data stream (N zeros needed for aliasing) and employing weighting to provide a stable estimate.

II. Power Spectra Estimate

The power spectra estimate may be obtained as (a) the Fourier transform of the auto correlation function or (b) directly by use of the FFT on the original data stream. The major considerations here are as follows:

(a) Fourier transform of R_r

(i) Desired resolution Bandwidths (B_e) and Degrees of Freedom (DOF)

With no further weighting, we have

$$B_e = \frac{1}{M\Delta T} , \qquad \mathrm{DOF} = \frac{2N}{M} \; .$$

where ΔT = time between samples.

Further weighting leads to the following relations:

	DOF	B_e
Bartlett	6N/M	$3/M\Delta T$
Tukey	5.333N/M	$2.666/M\Delta T$
Parzen	7.42 N/M	$3.72/M\Delta T$

These different windows have varying characteristics which do not appear to be critical for our problem. What is important is to obtain the desired B_e and DOF.

(ii) Statistics of Spectral Estimator

The resulting spectral estimator is χ^2 distributed with the DOF given above. Thus, confidence bars can be established accurately.

(b) Spectra by Direct FFT

(i) Desired resolution Bandwidths (B_e) and Degrees of Freedom (DOF)

Using the direct FFT without any time and/or frequency averaging leads to a poor spectral estimator. In fact, the standard error is equal to the estimate itself. It is not considered critical how the averaging is done. That is, the primary factors are the resulting bandwidth resolution and the DOF obtained. Thus, frequency/time averaging or use of some weighting function is somewhat arbitrary and we can consider the options. It is, however, important to correctly determine the DOF which result since this dictates the appropriate Chi-squared statistics.

General Comments

(i) Bias vs. variance (fidelity vs. stability)

Smoothing of the estimator in order to reduce the variance causes a bias error. Essentially, smoothing increases the resolution bandwidth B_e which reduces the variance while increasing the bias error. The DOF obtained essentially establishes the variance, while the bias error is given by:

$$\text{Bias} = \frac{K_1}{M^{K_2}} \Gamma''(f) \quad ,$$

where $\Gamma''(f)$ = second derivative of the spectra

K_1, K_2 = constants depending on the smoothing procedure.

Some general properties of the bias error are as follows:

- When $\Gamma''(f)$ is negative (near a peak of the spectra), the bias is negative and thus peaks will be underestimated. Conversely, when $\Gamma''(f)$ is positive (near a trough), the bias is positive and thus troughs will be overestimated.
- The narrower the peaks or troughs, the larger the value of $\Gamma''(f)$ and thus the larger the bias.
- The bias is reduced as M increases (the base width of the window is decreased). Therefore, the wider windows have larger bias error (and smaller variance).

(ii) Correlation of samples

When smoothing is employed the samples become correlated (resolution bandwidth increases). One should realize that the adjacent samples are not independent. However, the samples should be plotted since it is possible to miss a peak whose frequency lies halfway between uncorrelated samples if only the independent samples are plotted.

III. Estimates of Cumulative Probability Amplitude Distribution (C.D.F.)

If it is appropriate to plot the empirical cdf, the procedure for the present problem should be to group the data (i.e., set up a frequency table) and plot the cumulative distribution for the sample. There is too much data to plot the empirical cdf directly. Problems that arise here are as follows:

(a) determining how best to group the data so that we will not distort the data (e.g., should groups be equi-probable or fixed width with a standard set of class limits ?)

(b) determining if there are additional ways to display the data so that it is informative (e.g., histograms).

Also in presenting the empirical cdf is it useful to put confidence limits around it so that a graph, such as

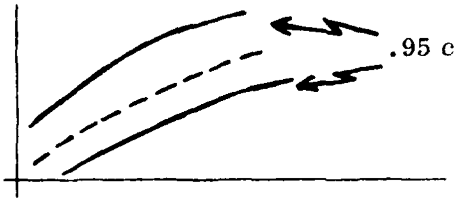

can be presented.

(c) Goodness of fit tests.

It appears that there are two main families of distributions to consider – the Nakagami m-distributions and the log normal distributions. At present, the test used for goodness of fit is the chi-squared test. The points that must be considered here are:

(i) determining the number of categories to use in the chi-squared test that will give the test maximum power.

(ii) determining how best to estimate the parameters of the distribution under consideration. In order to use the chi-squared test all the unknown parameters of the distribution being considered must be estimated from the data. There are optimal ways to do this (e.g., maximum likelihood techniques). Due to the large sample size sub-optimal techniques (e.g., methods of moments) may be sufficient.

(iii) determining the appropriate degrees of freedom for the chi-squared test.

(iv) One should also consider alternative testing procedures. For example, the Kolmogorov Smirnov test might be more powerful than the chi-squared test. Also, the $\sqrt{b_1}$ and b_2 tests applied to test for the log normal are more powerful than either the chi-squared or Kolmogorov Smirnov tests.

(v) There may be situations where more than one distribution may fit the data. For example, the Nakagami m-distribution with $m = 1$ may fit the data while the Nakagami with $m = 2$ may also supply a good fit. We may be able to supply techniques for deciding which of these two is the better fit of the data. In addition, we may be able to supply good graphical techniques to aid in deciding which distribution best fits the data.

IV. Other Considerations

(a) High frequency power spectra slope estimate

The estimate of the slope of the high frequency roll off of the spectra should be studied.

Most probably a least square fit to the spectra will provide "best" results. However, we should consider other alternatives. For example, the statistics of the spectra are known (χ^2 distributed) and the slope is really an estimate of the derivative of the spectra. Thus, we may be able to establish the statistics of the slope and from this the maximum likelihood estimate (which may be approximately or exactly the least square fit).

(b) Aliasing

Since the system bandwidth is 2Hz and the sampling rate is 6 samples/sec, there should be no real aliasing problems. When this is a concern, it can be checked by:

(i) Increasing the sampling rate, or

(ii) Checking the high frequency level of the spectra. This value should reflect the thermal noise level of the system. (Looking at some samples this appeared to be satisfied.)

(c) DC level

The DC level should be removed from the data before further processing is done. This can cause numerical differences in estimates (for example, the bias) if not removed.

(d) Maximum entropy spectral estimates

When interested in estimating a power spectra with sharp peaks, the maximum entropy spectral estimate has proven to be superior to the Fourier estimate. The spreading and bias problems inherent in the Fourier approach limit its use for peaked spectra.

CHI-SQUARED TEST FOR GOODNESS OF FIT

The chi-squared test can be used to test if a set of data is a random sample from a specified distribution. We suggest using this test with equiprobable cells. The number of cells should be from about 10 to 20. The final number will have to be decided after discussion.

The steps in the test are as follows:

(1) Decide upon k, the number of cells.

(2) Select the hypothesized distribution, F(x).

(3) Find the values of x_i, such that if the true distribution is F(x),

$$F(x_{i+1}) - F(x_i) = \frac{1}{k}\ , \qquad \begin{array}{l} x_0 = -\infty \\ x_k = \infty\ . \end{array}$$

These x_i determine the k cells.

(4) Compute the number of observations in the cells, call these 0_i for $i = 1, \ldots, k$.

(5) Compute the chi-squared statistic,

$$\underline{\bar{X}}^2 = \sum \left(0_i - \frac{n}{k}\right)^2 \Big/ \left(\frac{n}{k}\right)\ .$$

(6) If F(x) is the true distribution, $\underline{\bar{X}}^2$ has a chi-squared distribution with k-1 degrees of freedom.

Often times there are parameters of F(x) which are not known and must be estimated from the data. Say there are m of these unknown parameters. These parameters should be estimated using the maximum likelihood estimation procedure. All of the steps (1) to (5) above are carried out as shown except F(x) of (2) has the estimates in it and not the actual parameters. The distribution of $\underline{\bar{X}}^2$ of (5) is now chi-squared with k-m-1 degrees of freedom when F(x) is the true distribution.

The IMSL (International Mathematics and Statistics Library) subroutines can be used to perform some of the above.

Subroutine GFIF can be used to compute the chi-squared statistic. The hypothesized F(x) must be given as input. All parameters (or estimates of them) must be supplied. The number of estimates must be applied as input.

USE OF KOLMOGOROV-SMIRNOV TEST TO OBTAIN CONFIDENCE INTERVAL FOR EMPIRICAL CUMULATIVE DISTRIBUTION FUNCTION

It is possible to predict by means of confidence intervals how close the cumulative distribution of a sample can be expected to be to the cumulative distribution of the population. The confidence interval is based on the Kolmogorov-Smirnov test.

The steps in the procedure are as follows:

(1) Arrange the data in order of magnitude

$$X_{(1)} \leq X_{(2)} \leq \cdots \leq X_{(n)} .$$

(2) Plot empirical cumulative distribution function

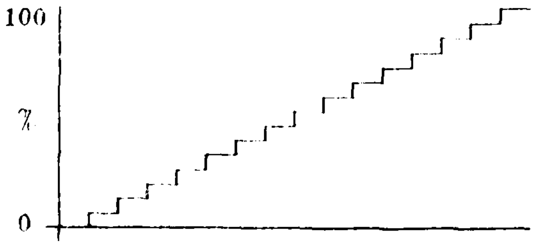

$$F_n(x) = \frac{\#(X \leq x)}{n}$$

For our problem we must investigate if the data must be grouped. Possibly with the rounding in the data grouping will not be needed.

(3) Above and below the empirical distribution draw two parallel polygons at a distance 100(1.36/n) = 136/n (for a .95 confidence interval). The width of a band giving confidence .95 for the statement, "The cumulative distribution of the population is in the band" is 200(1.36/n) = 272/n.

(4) The confidence band will look like

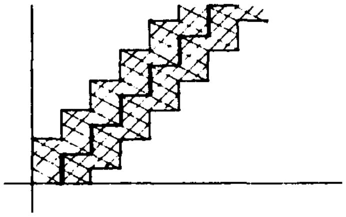

Any population cumulative distribution function which fits completely in this shaded region is consistent with the data at the .95 confidence level (or .05 significance level).

The IMSL (International Mathematics and Statistics Library) subroutines can be used to perform the above.

Subroutine VSORTA can be used to sort observations.

Subroutine USPC can be used to print and/or plot empirical cumulative distribution.

Subroutine USPC can be used to print and/or plot confidence interval (either a .95 or .99 confidence intervals can be obtained).

Subroutine USPC can be used to print and/or plot a theoretical (population) empirical cumulative. This theoretical distribution can be plotted on the same graph with the empirical distribution function and the confidence band. It is possible to produce printouts and/or plots for as many theoretical distributions as the user desires (e.g., log-normal, Nakagami m-distributions).

There are a few problems that may occur with the above procedure.

(1) The sample size, n, may be very large. This may create computational problems.

(2) The Kolmogorov-Smirnov test and the resulting confidence interval assumes a continuous distribution function and no grouping or rounding in the sample data. The technique is not valid if these conditions are not met.

(3) The theoretical distributions that can be appropriately compared to the empirical distribution (and the confidence band) are supposed to be completely specified. There are not supposed to be any estimated parameters. The technique is not valid if the parameters are estimated.

(4) It may be possible that no mathematical model (theoretical distribution) really matches the data. If the sample size is large we may observe the phenomenon that no standard distribution (e.g., log-normal or Nakagami-m) is acceptable by the above statistical criteria (i.e., falls within the confidence band).

None of the above problems should be taken to imply that this approach should be discarded. What is implied is that a routine writing of computer programs will not produce a finished product. Further discussion is needed to decide how to handle these problems. Also, it must be realized that questions will arise as the programs are being put together. These questions will have to be answered as they arise.

MAXIMUM LIKELIHOOD ESTIMATES OF THE PARAMETERS OF THE NAKAGAMI-m DISTRIBUTION

One way of writing the Nakagami-m distribution is

$$f(s) = \frac{M^{m}}{\Omega^{m}\Gamma(m)} S^{m-1} e^{-ms/\Omega} ,$$

where S = signal power, Ω = average power,

$\frac{1}{2} \leq m < \infty$ ($m = 1$ for Rayleigh fading, $m = 1/2$ for fading more severe than Rayleigh), and

$\Gamma(m)$ = gamma function of m.

Here,

$$\Omega = \int_0^\infty sf(s)\,ds \ , \qquad m = \frac{\int (sf(s)\,ds)^2}{\int (s-\Omega)^2 f(s)\,ds} \geq \frac{1}{2} \ .$$

The likelihood for a random sample of size n is

$$L = \frac{M^{mn}}{\Omega^{mn}\Gamma^n(m)} (S_1 S_2 \cdots S_n)^{m-1} e^{-(m/\Omega)\Sigma S_i}$$

$$\frac{\partial \log L}{\partial m} = n \log m + nm \frac{1}{m} - n \log \Omega - n \frac{\Gamma'(m)}{\Gamma(m)} + \sum \log S_i - \frac{\Sigma S_i}{\Omega}$$

$$\frac{\partial \log L}{\partial \Omega} = \frac{-nm}{\Omega} + \frac{m}{\Omega^2} \sum S_i \ .$$

The solution to these equations after setting $\partial \log L/\partial m = \partial \log L/\partial \Omega = 0$ is

$$\hat{\Omega} = \frac{\Sigma S_i}{n} = \bar{S} \qquad \text{and} \qquad \left[\frac{\Gamma'(m)}{\Gamma(m)} - \log m\right] = \frac{\Sigma \log S_i}{n} - \log \bar{S} \ .$$

The last equation must be solved recursively.

N.B. $\quad \Gamma'(m) = \frac{d\Gamma(m)}{dm}$.

INTERPRETATION OF SCINTILLATION INTENSITY SPECTRUM

Representing the scintillation random process as R(t), one may use either inphase and quadrature or magnitude and phase to describe the process. That is,

$$x(t) = |R(t)| \cos \theta(t)$$

$$y(t) = |R(t)| \sin \theta(t)$$

or

$$R(t) = |R(t)|\, e^{j\theta(t)}$$

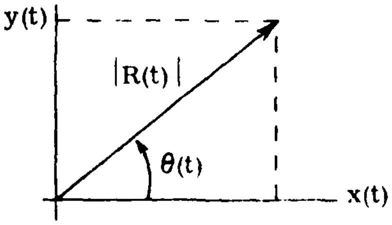

Since only the scintillation intensity is measured (i.e., $\theta(t)$ unknown), our signal is $|R(t)|^2$. Classically, the power spectrum is interpreted as

$$P(w) = \mathscr{F}[\phi(w)] = |E\{\mathscr{F}[R(t)]\}|^2 = |R_p(w)|^2 \quad ,$$

(watts
or db watts)

If it exists for
each realization
of the random process

where $\phi(w)$ is the statistical correlative function of $R(t)$ and $E\{\ \}$ denotes the mathematical expectation. However, here we define the spectra of the scintillation intensity as

$$P_s(w) = \mathscr{F}[|R(t)|^2]$$

for a given realization of the process.

Using the relation of multiplication and convolution of the Fourier transforms, we have

$$\begin{aligned} P_s(w) &= \mathscr{F}[|R(t)|^2] = \mathscr{F}[R(t)\ R^*(t)] \\ &= R_p(w) + R_p^*(w) = \Phi_s(w) \quad , \end{aligned}$$

where $\Phi_s(w)$ is the correlation function of the spectra $R_p(w)$ of the scintillation process.

Thus, $P_s(w)$ is the spectra of the scintillation intensity (in units of (db watts)) and is <u>not</u> the same as the power spectra $P(w)$ (or the square of the power spectra $P(w)^2$) of the scintillation process itself. But $P_s(w)$ is related to $P(w)$. In fact, it is the correlation function of the spectra $R_p(w)$. $P_s(w)$ can be interpreted as a spectra by considering the scintillation intensity as the time signal of interest.

Finally, $|P_s(w)|^2$ would have units (db watts)^2 and would be the power spectra of the scintillation intensity.

SPECTRAL SHAPE ESTIMATE

Attempts to obtain the MLE (Maximum Likelihood Estimate) for the spectral slope lead to an intractable mathematical formula due to the fact that the spectral estimates are Chi-squared (χ^2) distributed rather than Gaussian. Thus, we recommend use of the least squares estimate (which is the MLE under the Gaussian assumption). Here, the possible models are shown below.

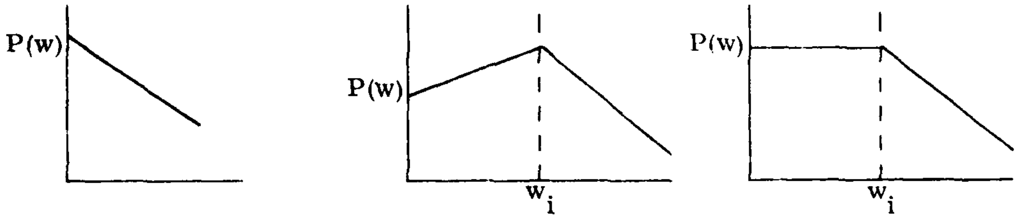

(a) (b) (c)

Figure 1

Case (a) requires a simple LS fit. However, cases (b) and (c) require a choice of w_i, the break frequency. Here, we suggest choosing w_i to minimize the overall mean squared error over w. Reference (1) provides a procedure for determining w_i. Basically, the procedure involves entering our initial guess for w_i and evaluating equation (1) below in a neighborhood about this point. Here, the final choice for w_i is that value which maximizes L(i).

$$L(i) = N \log \sqrt{2\pi} - i \log \hat{\sigma}_1 - (N - i) \log \hat{\sigma}_2 - \frac{N}{2} , \qquad (1)$$

where $N \triangleq$ total number of frequency points where spectra is estimated and

$\hat{\sigma}_1, \hat{\sigma}_2 \triangleq$ the standard deviations of the LS estimates of the spectra for the sections below w_i and above w_i, respetively, for the i being evaluated.

FADE DURATION DISTRIBUTION

To determine the distribution of fade duration, define $F_n(t)$ by

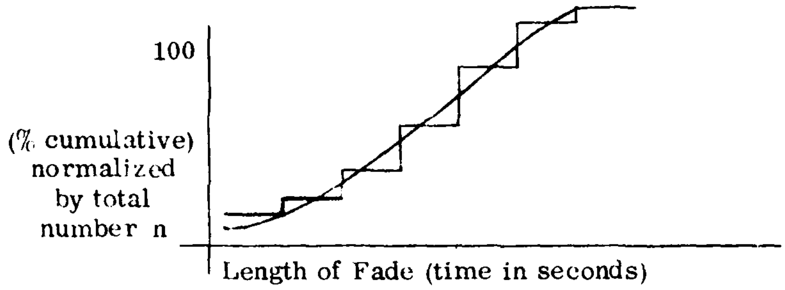

$$F_n(t) = \frac{\#(t \leq t_0)}{n} , \qquad n = \text{\# fades of a specific magnitude.}$$

We can then assume the fades are independent separate samples and the fade distribution is an empirical distribution function.

Since the true (theoretical) distribution function is not known, we can only establish confidence intervals by using a non-parametric procedure. We suggest the Kolmogorov-Smirnov procedure. Here, the confidence intervals are

$$F_n(t_0) - d \quad \text{to} \quad F_n(t_0) + d ,$$

where (if the sample size n is greater than ≈ 50), we have

For confidence	d
0.80	$1.07/\sqrt{n}$
0.90	$1.22/\sqrt{n}$
0.95	$1.36/\sqrt{n}$
0.99	$1.63/\sqrt{n}$

REFERENCE

(1) Quandt, R.W., "The Estimation of the Parameters of a Linear Regression System Obeying Two Separate Regimes," American Statistical Association Journal, Dec. 1958.

INVERSION OF CONVOLVED IR DATA

Initiator: Thomas D. Conley
Problem No.: 4910
Project No.: 7670

The major effort done under this problem number was the simulation and analysis of two optical (IR) spectra detection systems. One involved an electronic Butterworth filter while the second replaced the Butterworth configuration with a temporal filter. The equations may be summarized as follows:

1. Using Butterworth

System Transfer Function is given by

$$T(f) = \left[\frac{\sin \frac{\pi x f}{v_d}}{\frac{\pi x f}{v_d}}\right]^2 \frac{1}{\pi^2}\left[2\cos^{-1}\left(\frac{xf}{v_d 2.44}\right)\frac{xf}{v_d 1.22}\sqrt{1-\left(\frac{xf}{v_d 2.44}\right)^2}\,\right]^2$$

$$\times\left[\underbrace{\frac{f^n}{\left(f_0^{2n}+f^{2n}\right)^{1/2}}\;\frac{f_1^n}{\left(f_1^{2n}+f^{2n}\right)^{1/2}}}_{\text{Butterworth}}\right]^2$$

Input Background Noise Spectra is

$$B(f) = Kf^{-m} \quad .$$

Output power is

$$P = \int_0^\infty T(f) \cdot B(f)\, df \quad .$$

AD-A104 278 RDP INC WALTHAM MASS F/G 12/1
MATHEMATICAL AND NUMERICAL ANALYSIS IN SUPPORT OF SCIENTIFIC RE--ETC(U)
JUN 80 C J MCCANN, R M RAO, A MAZZELLA F19628-76-C-0212
UNCLASSIFIED AFGL-TR-80-0205 NL

2 OF 2
AD A
104278

END
DATE
FILMED
10-81
DTIC

2. Using Temporal Filter

Here, the Butterworth filter is replaced by

$$\left[\left(\frac{\sin \pi v_d fT}{\pi v_d fT}\right) \sin^n \pi v_d fT\right]^2 .$$

Performance of these systems with a target signal applied is evaluated by replacing B(f) with the target spectra.

The relative performances of these two systems may be evaluated by comparing the output S/N ratios of the two systems.

The parameters are defined as follows:

$X \triangleq$ footprint in meters

$v_d \triangleq$ drift velocity m/sec

$N \triangleq$ order of Butterworth filters

$V_t \triangleq$ target velocity

$M \triangleq 1.3$

$K \triangleq$ constant

$f_1 = V_t/2X$

$f_0 = f_1/10$

ALIGNMENT EXPERIMENT DATA ANALYSIS

Initiator: Capt. J.A. Shearer
Problem No.: 4921
Project No.: 7628

This problem was best handled using multiple regression analysis for fitting theoretical curves to experimental data. Consequently, the quality of various physical models were assessed.

In this particular application, the microscopic tilt of a missile in a silo was used as the dependent variable, as a function of fifteen other independent variables such as time, temperature, other tilts, and their derivatives.

The program calculates the correlation among the independent variables, and correlation with the dependent variable and the residuals resulting from the fit are analyzed to give their auto-correlations and power spectra. This allows analysis of any structure that may remain if the model is incomplete.

Results of the analysis showed that ≈ 90% of the variation in microscopic tilt was accounted for by an approximate function of temperature and certain tilt and tilt rate measurements.

PICTURE ELEMENT WORD LENGTH REDUCTION STUDY

Initiator: Rupert S. Hawkins
Problem No.: 4929
Project No.: 8628

INTRODUCTION

The problem concerned the development of a program for obtaining efficient computer oriented techniques for compressing the word length of satellite imagery while retaining image integrity. What we had to start with was an array of image brightness values, G(x,y). The array is rectangular, and each of the brightness values in the array can be associated with a small rectangular area of the image called picture elements.

The purpose of this effort was to obtain efficient automatic computer techniques for transferring image information, spread over the conventional six or eight bits of an image, to one bit while retaining the same element array. The objectives were the preservation of image brightness information in the reduced version and fast execution of the techniques on conventional computers.

The above program takes into consideration that the original image, G(x,y), can be either six or eight bits per picture element. Results were obtained for the following array sizes: 1) 80 x 80, 2) 500 x 500, and 3) 6400 x 6400 elements.

Mathematical Formulation and the Optimal Solution

The objective, in the ideal case, for this problem involves solving:

$$\min z = \sum_{x} \sum_{y} \sum_{n=1}^{m} \left| \overline{G(x,y)_n} - \overline{\Psi(x,y)_n} \right|^2 ,$$

where $\overline{G(x,y)_n}$ = average of values at n grid points about (x,y) using 6 or 8 bits information (64 or 256 levels) and $\overline{\Psi(x,y)_n}$ = is to be chosen so as to minimize z as a similar average using 1 bit of information (2 levels).

The problem as stated is an integer programming problem with a quadratic objective function.(1) The sizes of standard arrays (grids) to be considered are 80 x 80, 500 x 500, 6400 x 6400. Note that this indicates, in the smallest case, that 6400 variables are to be assigned integer values. Even in this "small" case we are well into the realm of "large" mathematical programming problems. In the absence of the integrality condition the problem is a nonlinear program. On the surface, it may appear the added requirement of integer valued variables should not present a serious problem. Indeed, the solution space is more restricted and the search need not be made over an infinite number of points. Unfortunately, such a conclusion could not be any more erroneous. Although the solution space for the integer (discrete) problem is structurally better defined, it has proved to be computationally formidable. In spite of over two decades of intense research, and a tremendous increase in computer speed and power, the developed integer algorithms have not yielded satisfactory computational results.

Some algorithms have been developed for nonlinear objective integer programming problems, which are only of theoretical interest at the current time. Even for small problems, 18-20 variables, they are not satisfactory. For large problems, over 100 variables, the state-of-the-art is severely limited even in theoretical results, computational advances are virtually non-existent.

For these reasons, this optimization problem cannot be solved with the present state-of-the-art in integer programming. However, we report this approach formally here since it defines the mathematical structure and offers some hope for the future.

Additional discussion of integer programming is provided in Appendix A for the sake of completeness.

General Considerations From the Literature

A review of the literature in picture processing and pattern recognition* has led to the following basic conclusions:

- There appears to be no other work closely related to the idea of conserving local brightness as a criteria for bit reduction.
- Virtually all algorithms for picture processing are somewhat heuristic. That is, they do something reasonable and consider the effects of varying the algorithms rather than formally deriving an "optimal" approach. This is due largely to the size of the arrays generally of interest and to the inherent nonlinearity of the desired optimization.
- Generally, considering the problem of thresholding or truncation and "enhancement," the basic forms of the algorithms(2) involve the use of the Laplacian with smoothing and subsequent thresholding. Here, depending on the particular objective, the details of a specific algorithm vary.

It is important to note that the present algorithms agree with this general approach and are thus consistent with the literature.

Based on these findings and the difficulties associated with integer programming, it is felt that the basic form of the algorithm is proper. Thus, the effort should be (and has been) directed toward the computer logic and parameter value optimizations of the algorithm, rather than attempting to develop a "new* approach.

Computer Optimization Efforts

We present here a discussion of the changes considered. We include both:

1. the historical or developmental approach of what has been done, and
2. the conclusions and recommendations resulting from the effort.

Historical

Briefly stated, an initial examination was made of the program, and a preliminary list of possible places for improvement was made. A few changes were made immediately to reduce the core-memory size of the program, even before any bench-marks were run. Then, a considerable amount of

---

* Including: NASA Reports and Defense Documentation Center Reports.

time was spent in getting SPY operating properly. (SPY is a timing program; it differs from SECOND in both accuracy and focus of attention; the program being timed itself is essentially unchanged.) Next, our own timers and counters were inserted in the program. Lastly, subroutine MATH was tested under a variety of frame sizes, shapes, and relative positions, with a variety of changes in Fortran, machine language and compiler options.

Conclusions of Computer Code Optimization

For all picture sizes:

1. Subroutine MATH was improved by about 40% by changing the structure of all "IF" statements logic and using computer optimizations level OPT=2. Further optimization to the "unsafe" level shows no essential improvement.

   Examination of the machine codes shows that rewriting the present logic in machine language will give no further improvement.

2. In practical applications on the CDC 6600, subroutine MATH is much less important than previously believed (when considering the overall program running time).

   For small pictures (80 x 80 elements) almost all the time is spent in PACK and ROW; even if we were able to reduce the time spent in MATH to zero, it would have little effect on the overall running time. For large pictures (672 x 475 mcidas) still twice as much time is spent in PACK as in the improved MATH.

Under the present setup, frames which are wide and short run faster than tall, narrow ones, because the number of calls to PACK is directly proportional to the height. Once in PACK the entire horizontal line is processed, not matter how little is actually needed. We recommend trying new ways of logic in PACK, such as random access, or keeping pointers to the starting edge of the frame desired. A desired frame size of 6400 x 6400 looks as if it might cause overload problems when considering the practical capabilities of the CDC 6600 system (by "system" we mean the conglomerate of hardware, software, and computer operations as practiced at AFGL). A few things to be examined further are:

(a) fine tuning of buffer sizes

(b) find out why PACK and ROW are better when not optimized

(c) program should be changed to give a message if the frame size is bad, instead of running to time limit with no printout.

(d) the only things on the original checklist that remain to be considered are buffering and double buffering. These should be attacked after the scheme for PACK is decided on.

The Two Algorithms Resulting from the Study

The two algorithms will be referred to as:

1. Original Optimized.
2. Modified.

The original optimized algorithm is that due to R.S. Hawkins which we have optimized for fastest computer running time while yielding the identical final matrix (0, 1). A flow diagram is shown in Figure 1.

The Modified algorithm changes the logic yielding a different final result. This algorithm is, in general, faster; however, in some cases the "quality" of the final (0, 1) picture is inferior to that of the original optimized algorithm. A flow diagram for the modified algorithm is given in Figure 2. The major difference is the skipping of elements which have been previously pushed to the upper or lower bound.

General Conclusions

We found that the results of both algorithms were very dependent upon the values of the incremental step size (c in Figures 1 and 2) and the upper and lower levels (a and b in Figures 1 and 2).

The Modified algorithm had, in general, improved running time and reduced energy difference. However, the "picture quality" seems inferior in some cases (for example, more granular).

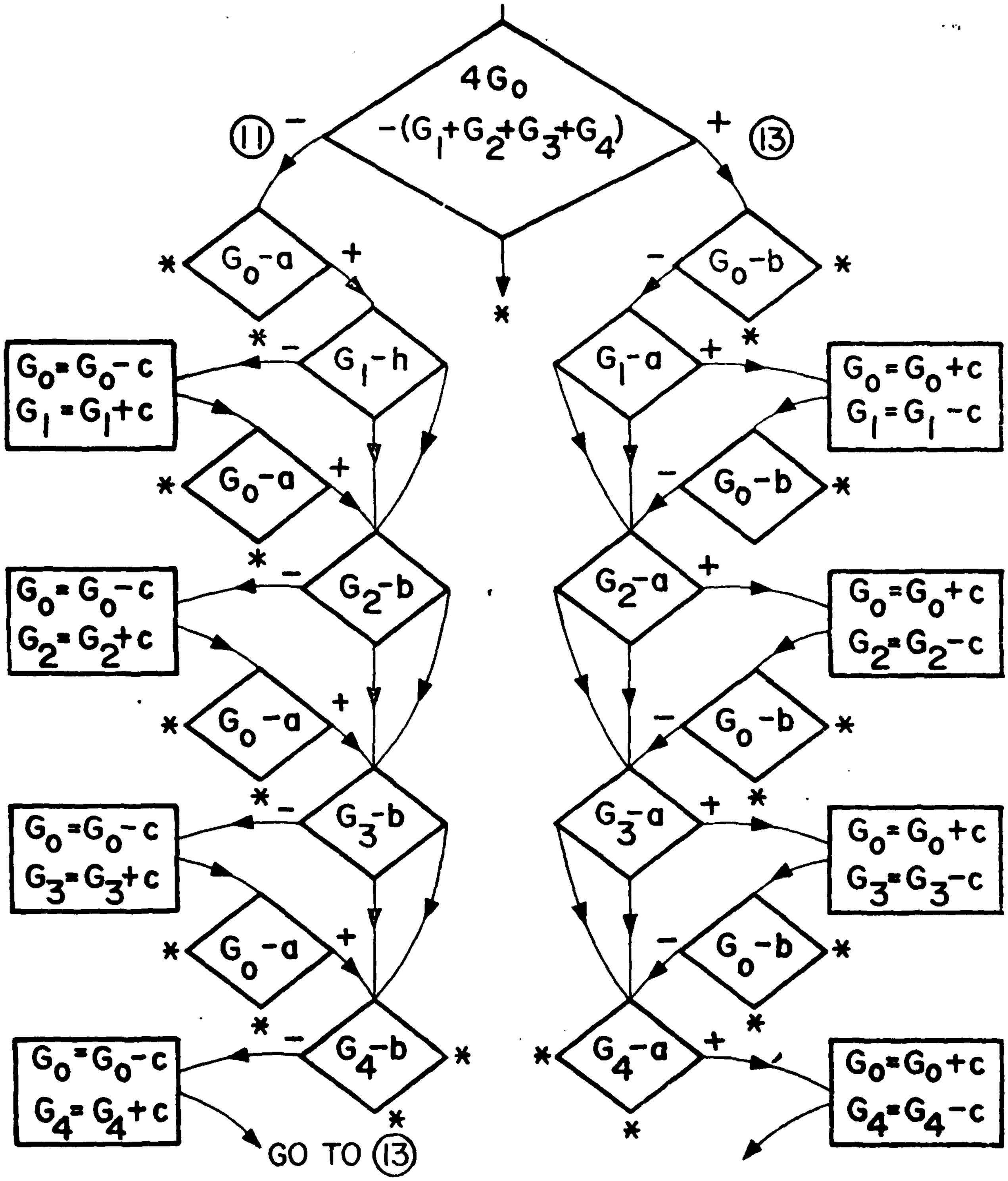

* GO TO DIAGONAL OR IF IN DIAGONAL MOVE NEXT POINT

Fig. 1. Original Optimized Algorithm

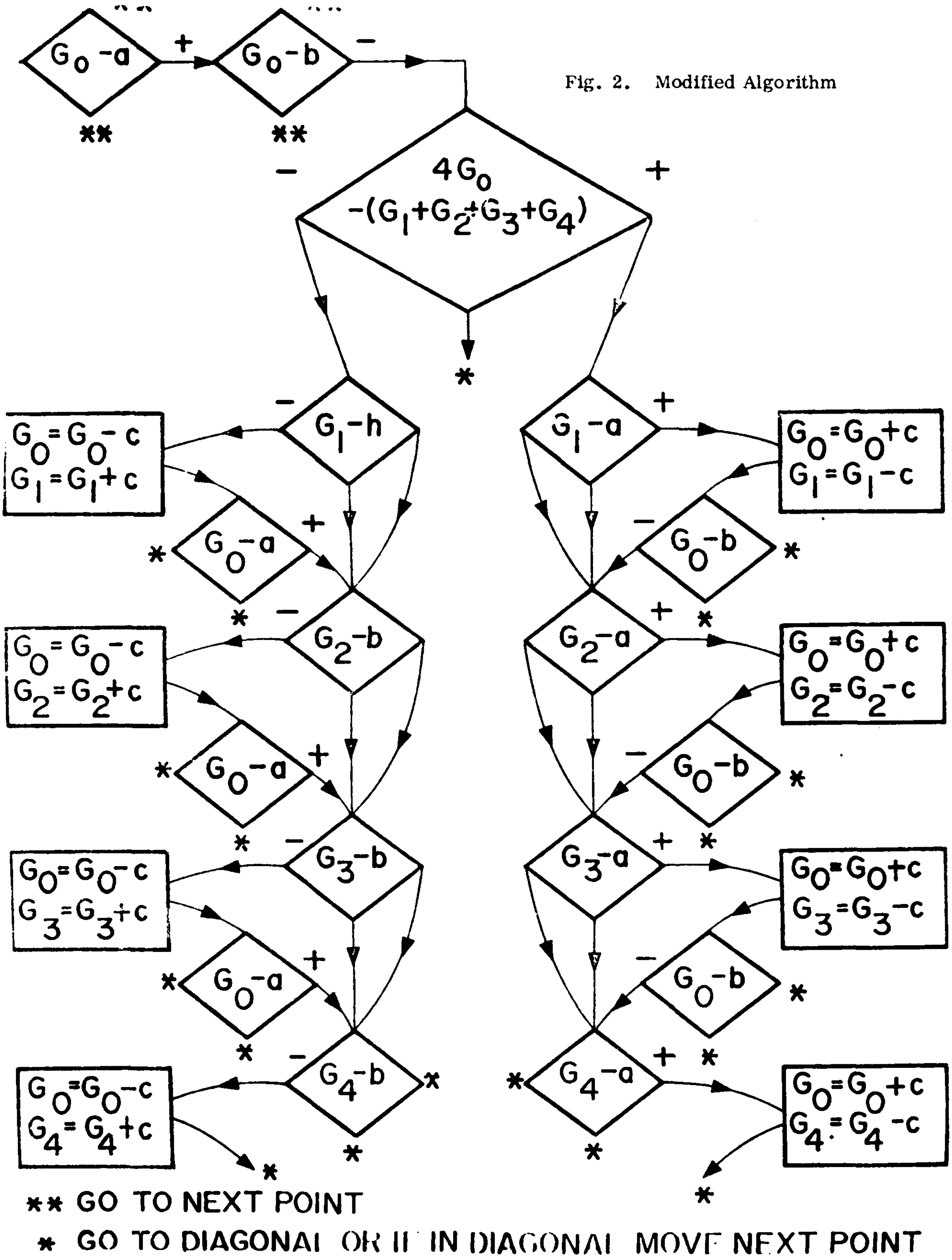

Fig. 2. Modified Algorithm

REFERENCES

(1) Integer Programming Theory, Applications and Computations, Tahg, Hamdy A., Academic Press, 1975.

(2) Digital Picture Processing, Rosenfeld, A. and A.C. Kak, Academic Press, 1976.

APPENDIX A

Some Properties of Integer Programming Problems(1)

Standard Integer Programming Problem with linear objective,

$$\text{max or min} \sum_{j=1}^{n} c_j x_j$$

$$\text{subject to} \sum_{j=1}^{m} a_{ij} x_j = b_i \quad , \qquad i = 1, 2, \ldots, m$$

$$x_j \geq 0 \quad , \qquad j = 1, 2, \ldots, n$$

$$x_j \text{ an integer (for some or all } j)$$

1. Cannot, as a first step, ignore the integer value constraints, solve the resulting math program (linear or nonlinear) and then round off the answers. Reasons are (1) rounded values may not satisfy the constraints (i.e., not feasible), or (2) rounded value if not necessarily even close to the optimal integer solution.

   Cannot solve continuous problem and then round up/down the answers.

2. Methods of solution generally fall into one of two approaches:
   i) enumeration techniques including branch and bound techniques or
   ii) cutting plane techniques.

   That is,

   Branch and Bound Method – Idea is to partition the feasible region into more manageable subregions – on each one of these branches a bound on the objective is derived and when it becomes clear that the Branch will not lead to the optimal solution attention is shifted to another branch.

   There are a number of explicit and implicit enumeration techniques which have been generated. Such techniques are generally in the class "branch and bound algorithms."

   Note that if there are n variables which are allowed to assume only two values each, then a complete tree has 2^n nodes (in the picture processing "small case", we have 2^{6400} in the 80 x 80 case, 2^{100} in

10 x 10 case). As a consequence if n is large, the amount of computer time required is very large. In large, binary cases an implicit scheme is used. Further, in linear objective case, at each branch point a linear program (continuous variables) must be solved.

Cutting Plane Methods – are almost always outperformed by a branch and bound method. It works by modifying linear programming solutions until the integer solution is obtained. It does not partition the feasible region; rather it uses a single linear program which is modified by adding new constraints. It is a very inefficient algorithm. Each new constraint (cut) removes an L. P. non-integer solution region and when a solution is reached which contains only integral values it must be the optimal point.

COMPUTATION OF OFF-AXIS RADIATION

Initiator: Mr. B. Schurin
Problem No.: 4949
Project No.: 7670

A computer program, OAREJ, was written to calculate the off-axis radiation from the earth's atmosphere measured by a sensor as a function of

(i) sensor altitude
(ii) tangent height, and
(iii) wavelength interval.

The program assumes that LOWTRAN 4 has been used in emission mode to compute atmospheric radiance with

(a) a fixed sensor altitude, and
(b) twenty-five lines of sight covering zenith angles of 90° to 180°.

Also assumed is that the spectral intervals and their corresponding filter functions have been specified and that these filter functions have been convolved with the output radiance from LOWTRAN 4. Currently, this computation is performed in a program called LOWFILT.

Input to OAREJ consists of:

(a) LOWFILT output spectral radiance incident on the sensor for 25 lines of sight, and
(b) sensor off-axis rejection weights.

The product of the sensor off-axis rejection function and the spectral radiance of the earth's atmosphere is numerically integrated over a solid angle in OAREJ. Since the off-axis rejection function is computed relative to the sensor line of sight, the coordinate system used in LOWTRAN to compute the radiance is rotated to yield radiance values compatible with the new coordinate system before the integration is performed in OAREJ. A subroutine is included in OAREJ to accommodate different vehicle altitudes. This option permits the user to run LOWTRAN at a fixed vehicle altitude and then obtain off-axis results for a variety of different vehicle altitudes. Alternatively, LOWTRAN may be run for each vehicle altitude and then LOWFILT and OAREJ run using each of the LOWTRAN outputs.

Description of the Computations in OAREJ

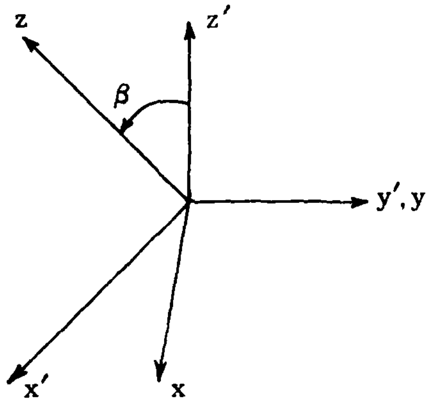

Figure 1

In Figure 1, the unprimed axes define the sensor coordinate system and the primed axis define the coordinate system in which the radiance from the earth's atmosphere is calculated. The origin of the two-coordinate systems is the sensor altitude (vehicle altitude); the z′-axis is the local zenith and the z-axis is the sensor line of sight; β is the angle from the local zenith to the line of sight.

The transformation from the sensor to the radiance coordinates can be written as

$$\begin{pmatrix} x' \\ y' \\ z' \end{pmatrix} = \begin{pmatrix} \cos\beta & 0 & \sin\beta \\ 0 & 1 & 0 \\ -\sin\beta & 0 & \cos\beta \end{pmatrix} \begin{pmatrix} x \\ y \\ z \end{pmatrix} . \qquad (1)$$

In terms of spherical coordinates (ρ, θ, φ), where ρ is the distance, θ the azimuth angle, and φ the zenith angle, the transformation can be rewritten as

$$\begin{pmatrix} \rho\sin\varphi' \cos\theta' \\ \rho\sin\varphi' \sin\theta' \\ \rho\cos\varphi' \end{pmatrix} \begin{pmatrix} \cos\beta & 0 & \sin\beta \\ 0 & 1 & 0 \\ -\sin\beta & 0 & \cos\beta \end{pmatrix} = \begin{pmatrix} \rho\sin\varphi \cos\theta \\ \rho\sin\varphi \sin\theta \\ \rho\cos\varphi \end{pmatrix} . \qquad (2)$$

Only the last equation in (2)

$$\cos \varphi' = \cos \varphi \ \cos \beta - \sin \varphi \ \sin \beta \ \cos \theta \qquad (3)$$

is required in the off-axis radiation calculations since the radiance in the atmosphere is assumed to be independent of the azimuth angle.

In the sensor coordinates, the off-axis radiation measured by the sensor as a function of β, the angle from the zenith to the line of sight, is given by

$$\mathrm{OAR}(\beta) = \int d\Omega \ W(\varphi, \theta) \ I(\varphi'(\varphi, \theta, \beta)) \ , \qquad (4)$$

where $d\Omega = \sin \varphi \, d\varphi \, d\theta$ = differential solid angle;

$W(\varphi, \theta)$ = point source off-axis rejection function of the sensor

$I(\varphi')$ = radiance of the earth's atmosphere (watts/cm^2-ster)

$I(\varphi')$ is a function of φ, θ and β as defined in Eq. (3), i.e.,

$$I(\varphi') = I(\varphi, \theta, \beta) \ . \qquad (5)$$

Equation (4) can be rewritten as

$$\mathrm{OAR}(\beta) = \int_{\varphi_d}^{\pi/2} d\varphi \sin \varphi \int_{-\pi/2}^{\pi/2} W(\varphi, \theta) \ I(\varphi, \theta, \beta) \ d\varphi \ . \qquad (6)$$

In the Eq. (6), the integration over θ in the present calculations has been restricted to the lower hemisphere about the line of sight. Numerical integration of Eq. (6) is performed in the computer program using the trapezoidal method.

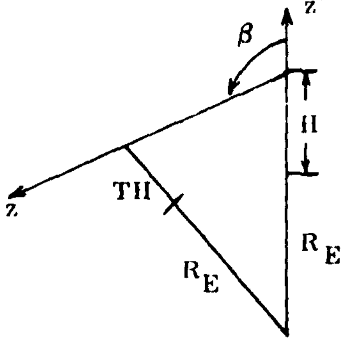

Figure 2

As shown in Figure 2, the zenith angle β and the tangent height TH are related by

$$\sin (\pi - \beta) = \sin \beta = \frac{TH + R_E}{H + R_E} \ , \qquad (*)$$

where H = the altitude of the sensor, and

R_E = the radius of the earth.

In the computation of OAR(β) in Eq. (6) the first problem is to determine the values of $I(\varphi, \theta, \beta)$. The known values are $I(\varphi')$ computed using LOWTRAN 4 and LOWFILT. The relation between φ' and the tangent height TH is given in (*). For a fixed φ, θ, and β,

$$\cos \varphi' = \cos \varphi \cos \beta - \sin \varphi \sin \beta \cos \theta \quad . \tag{**}$$

The program OAREJ uses the values

φ'_1, RAD(1)

φ'_2, RAD(2)

⋮

φ'_ℓ, RAD(ℓ)

and maps each φ'_m to the interval [1, 0] by means of the cosine mapping and then to the interval [0, 1] using the map $y = -x$. An interpolation precedes the last map.

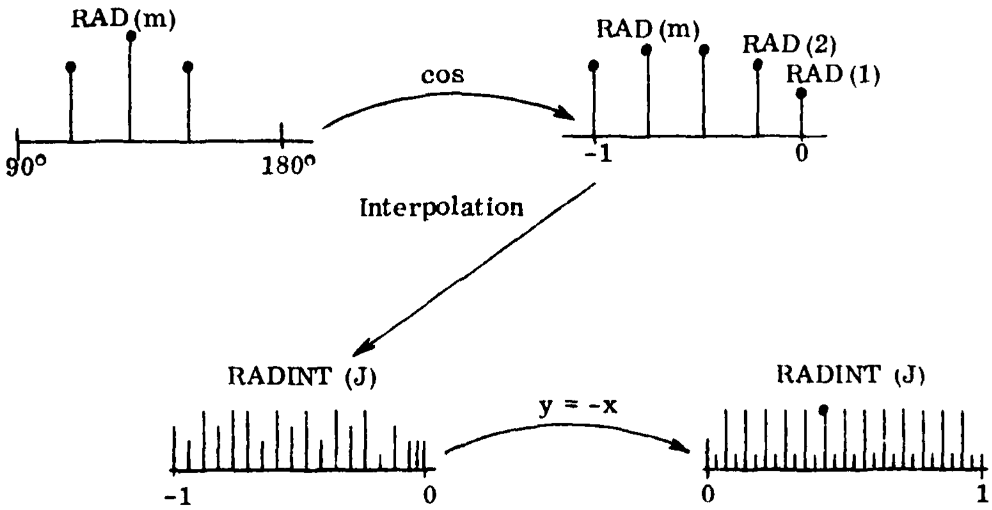

From (**), for fixed φ and β

$$-\cos\varphi' = -\cos\varphi\cos\beta + \sin\varphi\sin\beta\cos\theta \qquad (+)$$

and the relation (+) is used as a map of θ to $-\cos\varphi'$ and hence a radiance value is associated with (φ, θ, β).

Measured values $W(\varphi_i, \theta_j)$ of the off-axis rejection function are input to OAREJ on cards. For each fixed φ_i, OAREJ uses one of several options to generate interpolated values of $W(\varphi_i, \cdot)$. The option chosen is related to the number of θ_j inputs.

Finally, Eq. (6) is computed as follows:

$$G(\varphi) = \int_{-\pi/2}^{\pi/2} d\theta\, W(\varphi, \theta)\, I(\varphi, \theta, \beta) = 2\int_{0}^{\pi/2} d\theta\, W(\varphi, \theta)\, I(\varphi, \theta, \beta)$$

$$= 2\sum_{R=0}^{900} W(\varphi, \theta_k)\, I(\varphi, \theta_k, \beta)\, \Delta\theta_k$$

(the first and last terms are actually modified), where $\theta_k = (k/10) \cdot 1°$ and $\Delta\theta_k = (1/10)$th of a degree, then

$$\mathrm{OAR}(\beta) = \int_{\varphi_d}^{\pi/2} d\varphi \sin\varphi \int_{-\pi/2}^{\pi/2} d\theta\, W(\varphi, \theta)\, I(\varphi, \theta, \beta)$$

and so

$$\mathrm{OAR}(\beta) = \int_{\varphi_d}^{\pi/2} d\varphi \sin\varphi \cdot 2\int_{0}^{\pi/2} d\theta\, W(\varphi, \theta)\, I(\varphi, \theta, \beta)$$

$$= \int_{\varphi_d}^{\pi/2} d\varphi \sin\varphi\, G(\varphi)$$

$$= \sum_{k} \frac{\sin\varphi_{k+1}\, G(\varphi_{k+1}) + \sin\varphi_k\, G(\varphi_k)}{2}\, \Delta\varphi_k$$

In addition to computing OAR(β), the program modifies OAR(β) using the field of view characteristics of the sensor.

Subroutine to Extend LOWTRAN 4 Computed Radiance for Vehicle Altitude = 256 km to Other Vehicle Altitudes

The standard input to the OFF AXIS REJECTION program includes radiance values for 25 zenith angles (lines of sight) between 90° and 180° and for a vehicle altitude of 256 km. If off-axis radiation results are desired for vehicle altitudes other than 256 km, then

(a) LOWTRAN 4 can be rerun for the new vehicle altitude and for appropriate zenith angles.

(b) the LOWTRAN 4 – 256 km results can be interpreted as new vehicle altitude results by observing the relationship between corresponding zenith angles.

An algorithm for part (b) has been incorporated in the OAREJ program and the procedure used is as follows:

R_E = radius of earth
H1 = 256 km
TH = tangent height
H2 = new vehicle altitude

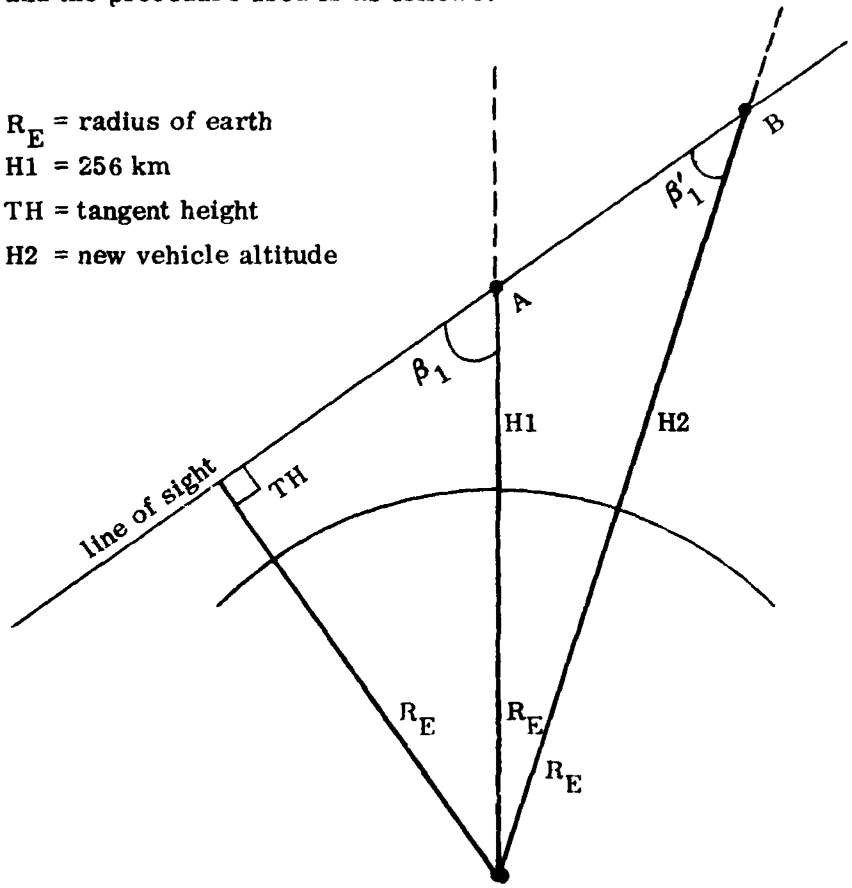

The underlying assumption is that the radiance incident on the sensor A and on sensor B along the indicated line of sight is the same and, in effect, only depends on TH.

By right triangle trigonometry,

$$\sin \beta_1 = \frac{TH + R_E}{H1 + R_E} \; ; \qquad \sin \beta_1' = \frac{TH + R_E}{H2 + R_E}$$

which implies

$$\beta_1' = \arcsin \left\{ \frac{(H1 + R_E) \sin \beta_1 - R_E + R_E}{H2 + R_E} \right\} .$$

Consequently, radiance values from LOWTRAN 4 for H1 = 256 km and angle β_1 will be the same as the radiance for H2 and angle β_1. Thus, if the following table gives the input to the off-axis rejection program for H1 = 256,

Angle	Channel 1	Channel 2		Channel k
β_1	$I_1(\beta_1)$	$I_2(\beta_1)$	···	$I_k(\beta_1)$
β_2	$I_1(\beta_2)$	$I_2(\beta_2)$	···	$I_k(\beta_2)$
β_3	$I_1(\beta_3)$	$I_2(\beta_3)$	···	$I_k(\beta_3)$
⋮	⋮	⋮		⋮
β_n	$I_1(\beta_n)$	$I_2(\beta_n)$	···	$I_k(\beta_n)$

then exactly the same table is appropriate for a vehicle altitude H2, but the *reference angle* β *is changed:*

Angle	Channel 1	Channel 2		Channel k
β_1'	$I_1(\beta_1)$	$I_2(\beta_1)$	···	$I_k(\beta_1)$
β_2'	$I_1(\beta_2)$	$I_2(\beta_2)$	···	$I_k(\beta_2)$
β_3'	$I_1(\beta_3)$	$I_2(\beta_3)$	···	$I_k(\beta_3)$
⋮	⋮	⋮		⋮
β_n'	$I_1(\beta_n)$	$I_2(\beta_n)$	···	$I_k(\beta_n)$

Input to OAREJ: The Off Axis Rejection Curves

For a given line of sight – the z-axis in the figure below – the off-axis rejection curves are measured as weights $W(\varphi, \theta)$, where φ is the angle from

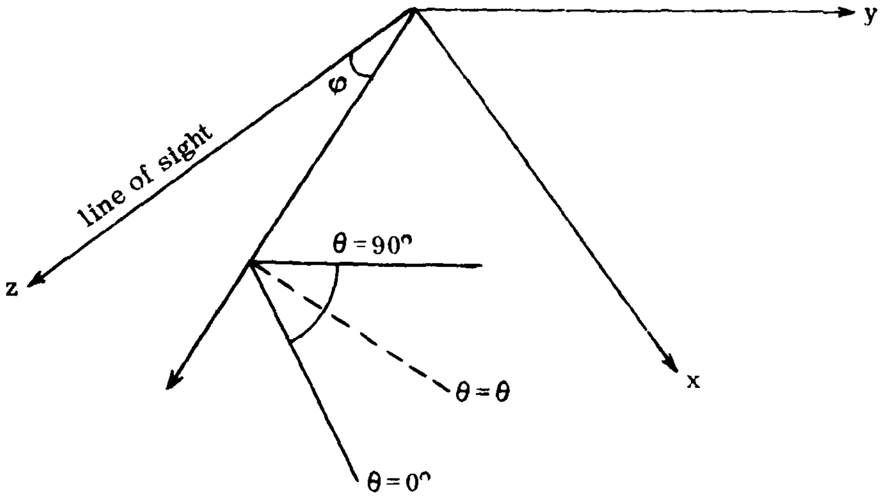

the z-axis to the x-axis and θ is the angle from the x-axis to the y-axis. See Figure 1 for the relation between the x-, y-, and z-axis and the LOWTRAN 4 coordinate system x′, y′, z′.

Typically, a sequence $0 \leq \varphi_1 < \varphi_2 < \cdots < \varphi_N \leq 90^\circ$ of φ values is specified. Then, for each φ_i one or more θ_{ij}'s, $0 < \theta_{ij} \leq 90^\circ$, are selected and measurements of the off-axis weights $W(\varphi_i, \theta_{ij})$ are taken. There are three options for the $W(\varphi, \theta)$ input to OAREJ:

1. For each φ_i, only one θ_j is selected and the one value $W(\varphi_i, \theta_j)$ is measured. The assumption is then made that

$$W(\varphi_i, \theta) = W(\varphi_i, \theta_j) \quad , \qquad -90^\circ \leq \theta \leq 90^\circ \quad .$$

2. For each φ_i, two θ's are selected $0^\circ \leq \theta_j < \theta_k \leq 90^\circ$ and the values $W(\varphi_i, \theta_j)$ and $W(\varphi_i, \theta_k)$ are input. The assumption in this case is that $W(\varphi_i, \theta_j)$ and $W(\varphi_i, \theta_k)$ lie on an ellipse $W(\varphi_i, \theta)$. The parameters defining the ellipse are determined from the above two input values.

3. For each φ_i, three or more θ_j's are specified. In this case, the values

$$W(\varphi_i, \theta_1), W(\varphi_i, \theta_2), W(\varphi_i, \theta_3), \ldots$$

are used as a base to generate other values $W(\varphi_i, \theta)$ by interpolation.

Note 1: The assumption

$$W(\varphi, -\theta) = W(\varphi, \theta) \quad , \qquad 0^\circ \leq \theta \leq 90^\circ$$

is in force throughout OAREJ.

Note 2: For Option 1 above, the measured value

$$W(\varphi_i, \theta_j)$$

is actually input twice and then Option 2 is executed.

POWER SPECTRUM ANALYSIS, DIGITAL FILTERING

Initiator:	E.A. Murphy
Problem No.:	4954
Project No.:	2310

This problem concerned experimental data with extremely poor signal-to-noise ratio. The objective was to investigate the use of digital signal processing techniques to improve the signal/noise characteristic in order to extract desired information.

A program was developed to examine the frequency spectra of the data.

This program calculates the Fast Fourier Transform of the specified input curve. It prints its magnitude and phase and then plots its normalized magnitude. The core storage needed (as specified in program) is directly related to the number of Fast Fourier points desired. The less points desired the less core storage required.

Coupled with the high noise level, it was found that the data drop out rate was so high that severe aliasing of the spectra was present. This rendered the extractions of useful information hopeless. Thus, no positive results could be obtained.

AUTOMATED AZIMUTH MONITORING

Initiator: T.E. Wirtanen
Problem No.: 4997
Project No.: 7600

The purpose of this problem was to extract data from a computer tape which was generated by an "in-house" automated azimuth monitoring system.

After running several tape dumping programs, it became apparent that most of what was occurring was meaningless noise, because all the meaningful information was packed into the very first record, which was not getting picked up correctly.

As it turned out, the mistakes are occurring at a hardware level, probably because the designers of the tape controller were unaware of industry-wide standards used by tape transport manufacturers. This is much more fundamental than, for example, reading a tape written in a "wrong" or "foreign" format.

Thus, the problem was returned to the initiator with some information as how to approach it.

ATE

LME